REPORT DOCUMENTATION PAGE			Form Approved OMB NO. 0704-0188		
The public reporting burden for this collection of information is estimated to average 1 hour per response, including the time for reviewing instructions, searching existing data sources, gathering and maintaining the data needed, and completing and reviewing the collection of information. Send comments regarding this burden estimate or any other aspect of this collection of information, including suggesstions for reducing this burden, to Washington Headquarters Services, Directorate for Information Operations and Reports, 1215 Jefferson Davis Highway, Suite 1204, Arlington VA, 22202-4302. Respondents should be aware that notwithstanding any other provision of law, no person shall be subject to any oenalty for failing to comply with a collection of information if it does not display a currently valid OMB control number. PLEASE DO NOT RETURN YOUR FORM TO THE ABOVE ADDRESS.					
1. REPORT DATE (DD-MM-YYYY) 18-11-2013		2. REPORT TYPE Ph.D. Dissertation		3. DATES COVERED (From - To) -	
4. TITLE AND SUBTITLE Synthesis, Characterization and Applications of Photoactive Nanomaterials			5a. CONTRACT NUMBER W911NF-09-1-0296		
			5b. GRANT NUMBER		
			5c. PROGRAM ELEMENT NUMBER 611102		
6. AUTHORS Sanjeev Kumar Kandpal			5d. PROJECT NUMBER		
			5e. TASK NUMBER		
			5f. WORK UNIT NUMBER		
7. PERFORMING ORGANIZATION NAMES AND ADDRESSES University of Southern Maine P.O. Box 9300 96 Falmouth St. Portland, ME 04104 -9300			8. PERFORMING ORGANIZATION REPORT NUMBER		
9. SPONSORING/MONITORING AGENCY NAME(S) AND ADDRESS (ES) U.S. Army Research Office P.O. Box 12211 Research Triangle Park, NC 27709-2211			10. SPONSOR/MONITOR'S ACRONYM(S) ARO		
			11. SPONSOR/MONITOR'S REPORT NUMBER(S) 56448-LS.27		
12. DISTRIBUTION AVAILIBILITY STATEMENT Approved for public release; distribution is unlimited.					
13. SUPPLEMENTARY NOTES The views, opinions and/or findings contained in this report are those of the author(s) and should not contrued as an official Department of the Army position, policy or decision, unless so designated by other documentation.					
14. ABSTRACT In the production of some devices, novel micro fabrications techniques are important, where the goal is compatibility with the system, convenience, and cost rather than high resolution. Electron beam and photolithography techniques are common fabrication techniques used in the semiconductor industry. Even though these techniques are common, they are high cost and not compatible with many substrates. This dissertation work explores a versatile and cost effective novel technique to fabricate fluorescent active micron					
15. SUBJECT TERMS photoactive, nanomaterials, gold nanoparticles					
16. SECURITY CLASSIFICATION OF:			17. LIMITATION OF ABSTRACT	15. NUMBER OF PAGES	19a. NAME OF RESPONSIBLE PERSON John Wise
a. REPORT UU	b. ABSTRACT UU	c. THIS PAGE UU	UU		19b. TELEPHONE NUMBER 207-228-8050

Report Title

Synthesis, Characterization and Applications of Photoactive Nanomaterials

ABSTRACT

In the production of some devices, novel micro fabrications techniques are important, where the goal is compatibility with the system, convenience, and cost rather than high resolution. Electron beam and photolithography techniques are common fabrication techniques used in the semiconductor industry. Even though these techniques are common, they are high cost and not compatible with many substrates. This dissertation work explores a versatile and cost effective novel technique to fabricate fluorescent active micron scale Laser Induced Structures (LIS). The optimization of the instrumental parameters and the mechanisms involved in structure formation are given, the photo-physical characterization of the LIS and a photoactive film used in solar cells is reported.

Here silver nanoparticles were synthesized through a wet chemical process, concentrated and drop cast as films onto different substrates. The drop cast films were air dried and subjected to 532nm continuous wave laser irradiation to generate structures in the film. A silver nanoparticle-polymer coating formulation was also explored for structure formation and critical instrumental parameters were studied. A mechanism is proven, similar to Liquid Melt Ejection (LME), to explain the structure formation. Thermo gravimetric analysis was performed to characterize the thermal decomposition of silver nanoparticle-citrate films. In a related study, photoactive film (made out of $SrAl_2O_4$: Eu, Dy phosphor material) for solar cells was photo-physically characterized to understand its emission mechanism and was investigated against the backdrop of its effect on photovoltaic cell efficiency.

A number of novel results were obtained in this work. One unexpected result relates to the structure being fluorescent active at the edges: a physical and chemical change of the material near the peak laser intensity occurred. This was attributed to light absorption and heating of the silver nanoparticles. LIS were generated with 14.3 mW laser power on silver-polymer coating based coating. Data described here suggests that the mechanism for structure formation is likely a result of: 1) absorption of radiation by the nanoparticles to generate heat, 2) decomposition of material near the particles creating water vapor, 3) the movement of material (mainly Na-citrate and Ag) by the vapor away from the laser focus. Sodium citrate dihydrate was found to be responsible for the fluorescent nature of the LIS. As sodium citrate dihydrate move away from the laser focus during heating and LIS formation, sodium citrate dihydrate close to the center of the beam is decomposed to an extent of loosing there fluorescent activity and forming sodium carbonate. But few microns away from the center of the laser beam the accumulated citrate molecule still have its fluorescent nature intact, which forms the edge of the LIS.

In the last section of this dissertation, the photoactive film ($SrAl_2O_4$: Eu, Dy phosphor material) coatings demonstrated a measured Photovoltaic (PV) response. However, the scattering losses due to the addition of nanoparticulates reduced the amount of "solar" radiation hitting the PV device surface. While it was evident that, under constant illumination, the photoactive films do add back some additional reemissions, via fluorescence upconversion or downconversion, radiation in the direction of the PV active element, the net losses are greater than the net gains.

SYNTHESIS, CHARACTERIZATION AND APPLICATIONS OF PHOTO ACTIVE NANOMATERIALS

By

Sanjeev Kumar Kandpal

B.Tech Chemical Engineering, Jawaharlal Nehru Technological University, 2008

A DISSERTATION

Submitted in Partial Fulfillment of the

Requirements for the Degree of

Doctor of Philosophy

(in Chemical Engineering)

The Graduate School

The University of Maine

August 2013

Advisory Committee:

Michael D. Mason, Associate Professor of Chemical & Biological Engineering, Advisor

Douglas W. Bousfield, Professor of Chemical & Biological Engineering

David J. Neivandt, Associate Professor of Chemical & Biological Engineering

Robert W. Meulenberg, Assistant Professor of Physics & Astronomy

William J. DeSisto, Associate Professor of Chemical & Biological Engineering

DISSERTATION

ACCEPTANCE STATEMENT

On behalf of the Graduate Committee for Sanjeev Kumar Kandpal, I affirm that this manuscript is the final and accepted dissertation. Signatures of all committee members are on file with the Graduate School at the University of Maine, 42 Stodder Hall, Orono, Maine.

Submitted for graduation in August 2013

Michael D. Mason, Associate Professor of Chemical & Biological Engineering   (Date)

LIBRARY RIGHTS STATEMENT

In presenting this dissertation in partial fulfillment of the requirements for an advanced degree at The University of Maine, I agree that the Library shall make it freely available for inspection. I further agree that permission for "fair use" copying of this dissertation for scholarly purposes may be granted by the Librarian. It is understood that any copying or publication of this dissertation for financial gain shall not be allowed without my written permission.

_____

Sanjeev Kumar Kandpal   (Date)

SYNTHESIS, CHARACTERIZATION AND APPLICATIONS OF PHOTO ACTIVE NANOMATERIALS

By Sanjeev Kumar Kandpal

Dissertation Advisor: Dr. Michael D. Mason

An Abstract of the Dissertation Presented
in Partial Fulfillment of the Requirements for the
Degree of Doctor of Philosophy
(in Chemical Engineering)
August 2013

In the production of some devices, novel micro fabrications techniques are important, where the goal is compatibility with the system, convenience, and cost rather than high resolution. Electron beam and photolithography techniques are common fabrication techniques used in the semiconductor industry. Even though these techniques are common, they are high cost and not compatible with many substrates. This dissertation work explores a versatile and cost effective novel technique to fabricate fluorescent active micron scale Laser Induced Structures (LIS). The optimization of the instrumental parameters and the mechanisms involved in structure formation are given, the photo-physical characterization of the LIS and a photoactive film used in solar cells is reported.

Here silver nanoparticles were synthesized through a wet chemical process, concentrated and drop cast as films onto different substrates. The drop cast films were air dried and subjected to 532nm continuous wave laser irradiation to generate structures in the film. A silver nanoparticle-polymer coating formulation was also explored for structure formation and critical instrumental parameters were studied. A mechanism is proven, similar to Liquid Melt Ejection (LME), to explain the structure formation.

Thermo gravimetric analysis was performed to characterize the thermal decomposition of silver nanoparticle-citrate films. In a related study, photoactive film (made out of $SrAl_2O_4$: Eu, Dy phosphor material) for solar cells was photo-physically characterized to understand its emission mechanism and was investigated against the backdrop of its effect on photovoltaic cell efficiency.

A number of novel results were obtained in this work. One unexpected result relates to the structure being fluorescent active at the edges: a physical and chemical change of the material near the peak laser intensity occurred. This was attributed to light absorption and heating of the silver nanoparticles. LIS were generated with 14.3 mW laser power on silver-polymer coating based coating. Data described here suggests that the mechanism for structure formation is likely a result of: 1) absorption of radiation by the nanoparticles to generate heat, 2) decomposition of material near the particles creating water vapor, 3) the movement of material (mainly Na-citrate and Ag) by the vapor away from the laser focus. Sodium citrate dihydrate was found to be responsible for the fluorescent nature of the LIS. As sodium citrate dihydrate move away from the laser focus during heating and LIS formation, sodium citrate dihydrate close to the center of the beam is decomposed to an extent of loosing there fluorescent activity and forming sodium carbonate. But few microns away from the center of the laser beam the accumulated citrate molecule still have its fluorescent nature intact, which forms the edge of the LIS.

In the last section of this dissertation, the photoactive film ($SrAl_2O_4$: Eu, Dy phosphor material) coatings demonstrated a measured Photovoltaic (PV) response. However, the scattering losses due to the addition of nanoparticulates reduced the amount of "solar" radiation hitting the PV device surface. While it was evident that, under constant illumination, the photoactive films do add back some additional reemissions, via fluorescence upconversion or downconversion, radiation in the direction of the PV active element, the net losses are greater than the net gains.

ACKNOWLEDGEMENTS

Jamie St. Pierre

Alexander Demers

Matthew Newsom

Harrison Gates

Andrew Doolittle

Finley Richmond

Ravikant Patil

David Cassidy

Undergraduate Students

Kody Allcroft

Aimee Co

Alieen Co

Shushil Kadka

Technical Assistant

Nick Hill

Kelly Edwards

Administrative Assistant

Cathy Dunn

Angel Hildreth

Theresa Paladino

Karen Lidral

Jonnie Johnson

Gurumaa, Family members and Friends

TABLE OF CONTENTS

LIST OF TABLES

LIST OF FIGURES

LIST OF ABBREVIATIONS

NPs- Nanoparticles

PT- Photothermal

RFID- Radio Frequency Identification

SERS- Surface Enhanced Raman Spectroscopy

LIP- Laser Induced Pyrolysis

LIS- Laser Induced Structures

PTM- Plain Thermax

DLVO- Deryagin-Landau-Verwey-Overbeek

c.c.c- critical coagulation concentration

CW- Continous Wave

MSD- Mean Square Displacement

RMSD- Root Mean Square Displacement

SPR- Surface Plasmon Resonance

MEF- Metal Enhanced Fluorescence

DLS- Dynamic Light Scattering

TEM- Transmission Electron Micrograph

DPSS- Diode Pumped Solid State

MD- Molecular Dynamics

CCD- Charge-Coupled Device

SEM- Scanning Electron Microscope

AFM- Atomic Force Microscope

XRD- X-ray Diffraction

EDAX- Energy Dispersive X-ray Spectroscopy

NA- Numerical Aperture

CLSM- Confocal Laser Scanning Microscopy

TGA- Thermo Gravimetric Analysis

FTIR- Fourier Transform Infrared Spectroscopy

Chapter 1
INTRODUCTION

There is a frequent demand for various functional microstructures due to their potential use in widespread applications. For example, fine scale structures in microelectronics are composed of conductive lines and other dielectric structures that give rise to the electronic devices we use everyday (Willson & Roman, 2008). In microfluidic devices, channels, sensors and pumps help to achieve precise control of fluid flow at the micro scale (E. Stankevicius, 2012; S. Jariwala, 2010; C. Schizas, 2010). In sensor applications, structures are generated that can detect small quantities of chemicals using techniques such as Surface Enhanced Raman Scattering (SERS) (Gouadec & Colomban, 2007). Also, in microoptics and photonics, structures are used to make microlenses and optical gratings (J. Serbin, 2004; R. Guo, 2006; J. Trull, 2011; M. Malinauskas, 2010). There are a number of related different techniques used to make these structures such as photolithography (Willson & Roman, 2008; Maekawa *et al.*, 2009; Nguyen *et al.*, 2007; Kim *et al.*, 2006; Mikami, 1994), direct laser writing (Rekstyte *et al.*, 2013), and Laser Induced Pyrolysis (LIP) (Aminuzzaman *et al.*, 2010; Maekawa *et al.*, 2009; Nguyen *et al.*, 2007; Kim *et al.*, 2006; Tekin *et al.*, 2008). All of these techniques use a combination of light and photosensitive material to produce structures with length scales from 20nm to 50μm.

The photolithography technique uses a light-sensitive polymer (photo-resist), which is exposed to ultraviolet (UV) light to transfer geometric shapes from a mask to a silicon or silicon dioxide wafer surface. Initially, UV light with wavelengths in the range of 193-436 nm is radiated through a photomask that consists of opaque features on a transparent substrate (e.g., quartz, glass) to make an exposure on a photo-resist that is coated on a substrate (Moreau, 1988; Elliott, 1989; Madou, 2002) . The polymer chains of photo-resist

break down in the exposed area, resulting in more soluble in a chemical solution called developer. The exposed photo-resist is removed in a developer to get the desired photo-resist pattern. This technique is capable of making structures from 37nm (B. D. Gates & Whitesides, 2005) to 3μm (Madou, 2002), with high throughput. The disadvantage for this method is that it requires a very expensive setup and most photoresists are expensive, toxic, and incompatible with many modern applications.

In Direct Laser Writing (DLW), structures are formed by localized polymerization, achieved more commonly by use of tightly focusing ultra shot laser pulses on a photosensitive substrate. This is achieved by controlled scanning of beam focus position, making it possible to create full 3D structures with submicron spatial resolution. DLS was mainly used for photoresist material, having the advantage of fewer steps, and less expensive setup over the traditional photolithographic technique. But DLS has a diffraction limitation on the minimum size it can achieve, usually around 350nm approximately (depending on wavelength of light, and NA of the objective). To overcome the cost of phtoresist, to tailor the compatibility of the substrates, metal nanoparticles are finding wide spread use in making different kinds of substrates photosensitive with customized compatibility to the applications. When nanoparticle doped substrates are used in place of photoresist; the mechanism of structure formation changes to LIP. Here temperature generated by photo absorption of metal nanoparticles is utilized in structure formation.

In LIP, a substrate is coated with a high nanoparticle metal content (>50% by wt) coating. The particles in the coating are separated by an organic surfactant. This substrate is moved under a focused laser beam. The laser beam decomposes the organic surfactant and sinters the nanoparticle together, leading to the formation of a conductive path along the path of laser exposure. Finally, the unexposed area is removed by a solvent washing step (Aminuzzaman *et al.*, 2010).

Nanoparticles have attracted attention of the scientific community because of their unique physical, chemical, and electronic properties. A few such properties have been ex-

ploited to make nano/micron structures, properties such as size dependent melting point depression (Buffat & Borel, 1976) (i.e bulk Ag MP=962°C, 20nm Ag MP=150°C), high photo to thermal energy conversion efficiency (Govorov & Richardson, 2007), and surface plasmon resonance property (Maier, 2007; Khlebtsov & Dykman, 2010). Exploiting these properties, Laser Induced Structures (LIS) can be drawn into the nanoparticle coated substrate. A common commercial use of laser induced structures is for laser marking. Laser marking is used to code a wide range of products with a small amount of variable data. The marking usually consists of a combination of four lines of text and machine readable codes. The text consists of product information such as best before dates, batch numbers for food, pharmaceutical products details, and classification marks on cables and wires. Laser marking of surfaces without nanoparticles requires high laser power, reduces the speed of the marking, and induces unwanted thermal stress on the surface. All these disadvantages may be overcome with the use of metal nanoparticle based coatings. Additionally, it also helps to choose a single wavelength where the absorption by the nanoparticle is at its maximum.

The work reported here developed a similar technique to that of LIP, but with low metal particle content, a significant polymer matrix around the particles, and an aqueous based reducing and stabilizing agent instead of organic agents, which are expensive and toxic. In this work, silver nanoparticles are used in coating formulation because of their high photo to thermal energy conversion efficiency and conductivity. This thermal energy causes a structural rearrangement of material at the surface generating features that are $8\mu m$ in width. Exposure to laser radiation leads to a different mechanism of structure formation that is linked more to the decomposition of the material around the nanoparticle and not an actual sintering of the particles. A surprising result is that material just outside of the edge, is fluorescent active. This activity is caused by sodium citrate dehydrate and this result may lead to methods to generate fine scale fluorescent regions for various applications.

In a separate project making use of the same analytical techniques, $SrAl_2O_4$: Eu, Dy phosphor material was synthesized, photo-physically characterized, and compared with commercially available $SrAl_2O_4$: Eu, Dy phosphor material. The effect of the phosphor material on the efficiency of a commercially available solar cell was studied by coating the surface of the photovoltaic cell with a polymer-$SrAl_2O_4$: Eu, Dy layer.

1.1 Organization

This dissertation is organized in the following manner: Chapter 2 will discuss important concepts involving light-nanoparticle interactions, colloidal stability, and potential processes involved during structure formation. Chapter 3 describes the formation of Light Induced Structures (LIS) on Ag nanoparticle based films and subsequent photo-physical characterization. Chapter 4 discusses the optimization of instrumental parameters enabling efficient LIS on Ag-polymer based coatings as well as surface temperature estimations of Ag nanoparticles during laser interaction. Chapter 5 explains the mechanism of LIS and explores reasons for the edges of LIS being fluorescent. Finally, Chapter 6 gives details about $SrAl_2O_4$: Eu, Dy phosphor material photo-physically characterization to understand its emission mechanism and presents an investigation of its effect on photovoltaic cell efficiency. While a fundamentally unique nanoparticle system many of the same tools were employed.

Chapter 2
LITERATURE REVIEW

In this chapter all the major concepts related to laser-nanoparticle interactions are been reviewed. Since the work reported in the dissertation involves considerable nanoparticle synthesis, a review of the synthesis techniques employed is given.

2.1   Nanoparticle Synthesis

The synthesis of nanoparticles is a fairly well established field as particles of submicron or nanosized dimensions have been synthesized for centuries. The Roman Lycurgus Cup, a bronze cup lined with colored glass, is one of the foremost examples of the use of nanoparticles that dates to the fourth Century AD. This glass scatters a dull green light yet transmits red light. A study of this glass showed that it consists of an alloy of 70nm particles (70% Ag and 30% Au) (Evanoff & Chumanov, 2005). Silver nanoparticles of this size are known to scatter green light, and the addition of Au shifts the absorption band to longer wavelengths. While this particular application of nanoparticles may not have been intentional, small Au and Ag nanoparticles were often used in later centuries to create ruby red and lemon yellow stained glass.

Centuries later Faraday described several methods in his 1857 lecture, in which the reduction of gold chloride by phosphorous in carbon disulfide seemed to produce the most highly colored "rubyred fluids" But the most popular method to produce Au suspensions is the so-called Turkevich method, which employs the reduction of chloroauric acid with sodium citrate and produces a narrow size distribution of around 10 nm particles. For Ag nanoparticle suspensions, a common method is the Lee-Meisel method, which is similar to the Turkevich method with slight change of $AgNO_3$ used as the metal source. However, unlike the Turkevich method, the Lee-Meisel method produces a broad distribution of

particle sizes. The most famous method for Ag nanoparticle synthesis is the Creighton method, mostly known to produce a narrow size distribution (approximately 10nm) of nanosized Ag particles by reduction of $AgNO_3$ with $NaBH_4$. This method can also be adapted to produce particles of other metals such as Pt, Pd, Cu, Ni, etc., although it depends on the reduction potential of the source ion. For example Cu and Ni suspensions are not very stable as the metal particles are easily oxidized, requiring strong capping ligands to prevent oxidation.

The three metals which have Plasmon resonances in visible region are Au, Ag, Cu. Among these three, Ag has the highest efficiency of Plasmon excitation because optical excitation of Plasmon resonances in nanosized Ag particles is the most efficient mechanism by which light interacts with matter. The light interaction cross-section for silver is ten times more than its geometrical cross-section, which implies that the particle captures more light than physically incident on it. Apart from this, silver is the only metal whose Plasmon resonance can be tuned to any wavelength in the visible region.

There are many methods for synthesis of silver nanoparticles and these can be broadly classified into Traditional and Non-traditional methods. Traditional methods are solution-phase synthesis techniques which are based on different modifications of the Lee-Meisel and Creighton methods. There are many examples in which different Ag salts and reducing agents are used. Aggregation is stopped by the formation of electrical double layers around metal nanoparticles in low-ionic-strength suspensions. For high ionic strengths or organic-phase suspensions, capping agents, surfactants, polymers, and dendrimers are used to protect the particles from aggregation. Anisotropic particles can be synthesized by use of capping ligands because of the differing affinity of ligands towards exposed crystal faces. This phenomena is preferred in the making of different shapes of particles by the use of appropriate reducing agents. Alternatively, nanoparticles can be capped with desired molecules after synthesis to facilitate their transfer into non polar phases and to modify their surface chemistry.

Non-traditional synthesis methods include electrolysis of Ag salt solutions, laser ablation of a metal, photo-reduction of Ag ions, particle synthesis by high temperature reduction in porous solid matrices and vapor-phase condensation of a metal onto a solid support. The above mentioned are not the exhaustive list of methods of the available synthetic methods, but a broad representation of what has been reported. Fortunately or unfortunately, all of the methods listed have some advantages and disadvantages, the selection of a specific synthetic procedure depends on the nature of the nanoparticle application. With the traditional methods, the major drawback is often a limited flexibility in the size of particles they produce, specifically such methods are very good in producing <10 nm particles. Due to a large surface-to-volume ratio, small particles are more useful in catalysis, but for optical applications, larger particles are often preferred. Small Ag nanoparticles do not interact with light nearly as efficiently as particles that are in the 50 to 100 nm range which do so by energy absorption. An additional advantage with large particles are that the plasmon resonances in larger Ag nanoparticles have a significant light-scattering component that can be advantageously used in applications that require efficient optical labels, such as in chemical assays, and tissue imaging (Evanoff & Chumanov, 2005).

Nanoparticle solutions are colloidal solutions and to take advantage of the nanoparticles in the solution, one has to prevent them from aggregating and precipitating out of solution. To do so one has to have an understanding of colloidal stability, Here a brief review of colloidal stability is given.

2.2 Review of Colloidal Stability

Colloidal systems consist of two different phases i.e. the finely divided dispersed phase (in the size range of 1-1000 nm) is suspended in a continuous phase. Colloidal systems can be solid/liquid/gas and the word "microheterogeneous" is commonly used to

describe colloidal systems. The small size leads to high surface-to-volume ratios, which results in a large number of molecules lying near the surface. The molecules at the interface have properties different from those of the bulk phase, and substantiate the importance of surface chemistry in affecting the properties of colloids. The material within a molecular layer of the solid/liquid interface wields the greatest influence on particle-particle and particle-medium interactions. Therefore, it is the interactions in this molecular layer which the scientific community is trying to understand. The understanding will help formulate additives to facilitate the appropriate level of stability when making a dispersion, and instability when weak flocculation is desirable, such as in many coating and paint formulations (Everett, 1988; Shaw, 1992; Tadros, 1987; Buscall *et al.*, 1985; Gibson, 1998).

According to the laws of thermodynamics, all systems must minimize their free energy and according to first principles, the free energy of two colloidal particles increases as the separation distance between them increases. For a colloidal system approaching zero separation distance between particles, tend to agglomerate. To prevent agglomeration, one has to use an energy barrier that keeps the particles separated. This energy barrier balances the forces of attraction between particles with repulsive forces. Stabilizers such as surfactants or polymers are used to modify the solid/liquid interface such that an energy barrier is created and a metastable thermodynamic state is achieved (Everett, 1988; Tadros, 1987; Israelachvili, 1992). Here the nature and energetics of colloidal stability is described.

2.2.1 Intermolecular Forces

The natural attractive force between non-polar particles was first observed by van der Waals in 1873. Fritz London showed that the attractive forces arise from fluctuating dipoles within a molecule and with the application of quantum mechanics he determined that they were proportional to the 7$^{\text{th}}$ power of the separation distance between

the molecules. After integration of the expression (of attractive forces between fluctuat-ing dipoles within a molecule) with respect to distance, he determined that the work to reversibly separate the particles from a distance d to infinity is given as:

$$\Delta G_{att} = -\Delta W = \frac{A'}{d^6} \tag{2.1}$$

where the work at infinite separation is defined as 0, and A' is given as

$$A' = \frac{3}{4} h v \alpha^2 \tag{2.2}$$

Where v is the frequency of the first ionization potential that lies in the UV region of the electromagnetic spectrum. When the molecules get too close to each other the electron clouds of the atoms overlap and a short-range repulsive force is generated. The resulting potential is expressed as:

$$\Delta G_{rep} = \frac{B'}{d^{12}} \tag{2.3}$$

The Lennard-Jones potential for describing the total interaction between two atoms is the summation of the attractive and repulsive energies. Here it can be observed that the van der Waals forces act over long distances compared to repulsive forces.

$$\Delta G_{total} = \frac{B'}{d^{12}} - \frac{A'}{d^6} \tag{2.4}$$

2.2.2 Attractive Potential

The attractive force between two colloidal particles can be calculated by summation of the forces between individual molecules comprising the particles. For two infinite flat plates a distance h apart, the free energy per unit area is given as:

$$\Delta G_{att} = \frac{-A_H}{12\pi h^2} \tag{2.5}$$

Where A_H is known as the Hamaker constant and is given as:

$$\Delta A_H = A' \pi q^2 \tag{2.6}$$

Where q is the number of molecules per unit volume of particles.

2.2.3 Repulsive Potential

To understand repulsive forces between particles in detail, one has to understand the electrical double layer, Debye's length, DLVO theory and the Schultz-Hardy Rule. These concepts are described below according to their relevance to the system presented in this work.

2.2.3.1 Electrical Double Layer

It is well known that most colloidal particles are electrically charged and that there is a tendency of charge accumulation at the interface of two phases (surfaces/mobile phase). It has been observed that electrostatics play a major role with a dielectric constant higher than 30 (Wu & Setterquist, 1991). The accumulated charges (σ_0) on the particle surface are balanced by the countercharges from the solution which are opposite in charge ($-\sigma_0$) and equal in magnitude. The combination of surface charge and countercharge form what is known as the electrical double layer. The accumulation of charge on a particle surface may occur in a variety of ways, such as ionization of surface groups, unequal distribution of lattice forming ions at the surface due to differential solubility, isomorphous substitution, charged crystal surfaces and adsorption of specific ions. While each mechanism is important, perhaps the most easily understood and widely applicable is ionization of surface groups, described in detail below.

2.2.3.2 Ionization of Surface Groups

Dissociation of surface groups leads to charged surfaces. An acidic surface group after dissociation leaves a negatively charged surface and vice versa for basic surface groups. The relative strength of surface groups and pH of the solution determines the magnitude of the surface charge. The pH at which the surface charge is zero is called the point of zero charge. In the absence of specific adsorption, the point of zero charge is equivalent to the isoelectric point, (i.e.p). The isoelectric point is defined as the pH at which the zeta

potential becomes zero. The zeta potential is a measure of the charge located roughly one molecular layer into the medium, refered to as the Stern or inner layer of the electrical double layer. The counterions in the electrical double layer exist either in a mobile state

a)   b)
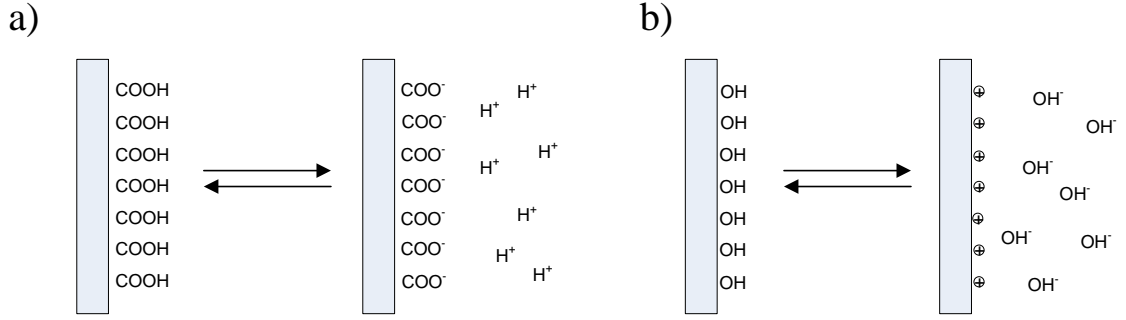
Figure 2.1. Ionization of surface groups. Ionization of acid groups giving rise to negatively charged surface (a). Ionization of basic groups giving rise to positively charged surface (b).

due to thermal energy, the diffuse layer, or fixed near the surface in the Stern plane, as in the case of specifically adsorbing ions. The surface charge is thus balanced by the combination of charge from the ions in the diffuse and Stern layers ($\sigma_0 = \sigma_s + \sigma_d$). Here σ_0 is the surface charge of the particle, σ_s is the charge in the stern layer and σ_d is the charge in the diffuse layer. According to Boltzmann's distribution law, the probability of finding a particle at a given point and having a free energy or potential energy V relative to a reference point, can be derived from the chemical potential, in terms of the concentration of counterions in the solution. For positive ions:

$$\mu = z_+ e\psi + KT \log c_0 \tag{2.7}$$

Here z_+ is the valency of the positive ion, e is the elementary electronic charge, ψ is the electrostatic potential, and c_0 is the concentration of positive ions in the region where ψ is zero. Similarly for negative ions, the expression is

$$c_- = c^0 exp\left(\frac{+z_- e\psi}{KT}\right) \tag{2.8}$$

11

So the net excess charge in the region will be

$$c_+ - c_- = c_0 \left[exp\left(\frac{-z_+ e\psi}{kT} \right) - exp\left(\frac{+z_- e\psi}{kT} \right) \right] \tag{2.9}$$

This excess of charge forms a charge cloud, ionic atmosphere, or electrical double layer. For electrically neutral solutions the net charge in a volume will be zero, which can be expressed as :

$$\int_{V_{Total}} [c' - c]dV = 0 \tag{2.10}$$

The above equation is the basis for the Debye-Huckel theory of electrolytes. The charge on the particle is distributed over the surface of the particle and is balanced by the total charge in the double layer. This type of description of colloidal particles was first made by Helmholtz and later developed by Stern, Guoy, and Chapman. A schematic of the electrical double layer is shown in Figure 2.2. The plane with thickness β is known as the
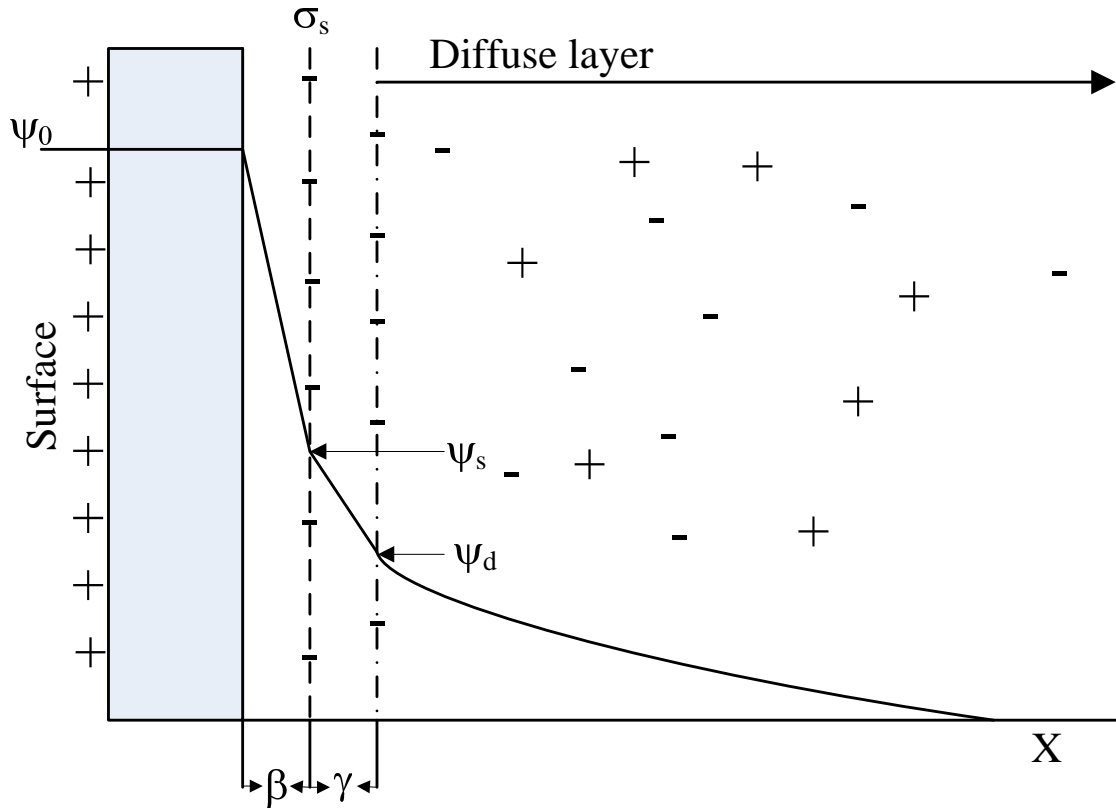
Figure 2.2. Electrical double layer model.

inner Helmholtz plane, i.H.p. The plane with thickness γ, ending at the boundary to the diffuse layer is known as the outer Helmholtz plane, o.H.p. The charge density is high near the surface and gradually falls off as shown by the solid curves in the figure. Also shown are the corresponding potentials due to the charged nature of the system. On the surface the net charge is σ_0 which results in a surface potential, ψ_0. Similarly, the Stern layer and diffuse layers have potentials ψ_s and ψ_d, respectively. The length of the double layer is estimated using the Debye length equation, which estimates the length over which the surface potential drops from ψ_0 to ψ_0/e and is given by:

$$\kappa^{-1} = \left[\frac{\varepsilon KT}{e^2 \sum_i c_i z_i^2} \right] \tag{2.11}$$

The Debye length expression indicates that as the concentration of electrolyte increases, the thickness of the double layer decreases. This explains why colloidal solutions tend to coagulate as the concentration of the electrolyte increases. To summarize the above discussion, one can picture the colloidal particle as each particle surrounded by its own electron cloud. Two colloidal particles will attract each other due to van der Waals forces, until their electron clouds overlap and begin to repel each other.

2.2.3.3 DLVO Theory

The basics of the Deryagin-Landau-Verwey-Overbeek (DLVO) theory have been described above. The original theory was derived from the contributions of van der Waals attraction and electrostatic potentials to the total energy curve. In this section the Schultz-Hardy rule will be reviewed, which describes the effect of the nature of the electrolyte inducing instability in the colloidal solution. Schultz-Hardy found that the ion charge and valency play important roles in promoting instability in the colloidal solution. The key results of their findings were that ions of the same charge had less effect irrespective of their valency, and ions of opposite charge had a greater effect on destabilization of colloidal solutions. The concentration of electrolyte required to induce instability decreases as its

valency increases. The critical coagulation concentration (c.c.c) is the minimum concentration of electrolyte needed to induce rapid and therefore, irreversible, coagulation. The Schultz-Hardy rule states that the c.c.c. is mainly a function of the valency of the counterion. One of the assumptions of the original DLVO theory was that the potentials for two overlapping double layers were additive. For two flat parallel plates, the total interaction potential energy is, $V_{tot} = V_{el}^{rep} + V_{vdw}^{att}$, where

$$V_{vdw}^{att} = \frac{-A}{12\pi D^2} \tag{2.12}$$

$$V_{el}^{rep} = 2\pi\varepsilon a\xi^2 exp(-\kappa D) \tag{2.13}$$

Here A is the Hamaker constant, D is the interparticle separation, a is the particle radius, ε is a function of the ionic composition, and ξ is the zeta potential. The repulsive term is dependent on the concentration of the electrolyte through the exponential term in Equation 2.13, in the form of the Debye length, which in turn is dependent on the concentration of the electrolyte. As electrolyte concentration increases, the energy barrier decreases, leading to coagulation. An approximate way of determining the c.c.c. is to locate the point on the total interaction potential curve where both $V_{tot}^{int} = 0$ and $\frac{dV_{tot}^{int}}{dD} = 0$, yields c^0(c.c.c) which is inversely proportional to $A^2 z^6$. Both DLVO theory and the empirical Schultz-Hardy Rule are in very good agreement in estimating c.c.c. For Ag nanoparticles capped with citrate in aqueous solution, the total attractive and repulsive forces between particles are predicted using the equations described above in MATHCAD software and the results are attached to Appendix F.

2.2.4   Means of Increasing Colloidal Stability

To increase colloidal stability, repulsive forces must be increased. This may be addressed in two ways as shown in Figure 2.3.

1. Electrostatic: In this method, particle interactions are controlled using formulated electrolytes. These electrolytes form ionic clouds around the particles (through

processes including ionization of surface groups, unequal distribution of lattice forming ions at the surface due to differential solubility, isomorphous substitution, charged crystal surfaces and adsorption of specific ions), as shown in Figure 2.3. Such mechanisms prevent particles approaching each other through electrostatic repulsions.

2. Steric Repulsion: In this method polymer is added to the colloidal dispersion which adsorbs onto the particle surface. This prevents particles from coming into close contact due to the steric repulsion between polymer molecules; at the resulting separations, vander Waals forces are too weak to make particle adhere.

Steric Stabilization   Electrostatic Stabilization
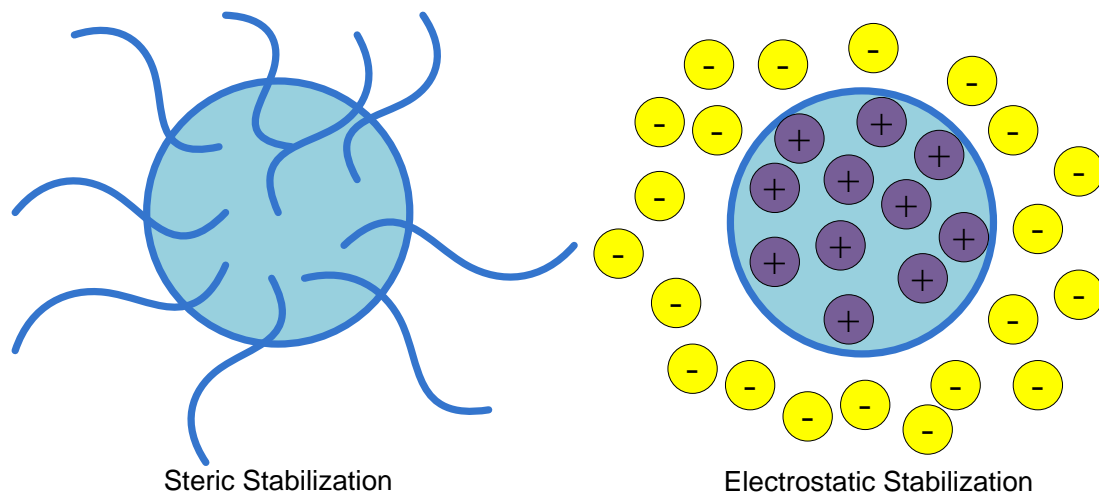
Figure 2.3. Steric and Electrostatic stabilization.

This section on colloidal stability was written referring to Gibson (1998) and documents available on Malvern website.

2.3 Light Scattering by Particles

Light scattering by particles plays an important role in various fields including physics, biology, meteorology, paper technology and many more. As visible radiation is incident

upon matter, whether it is dense as in a solid, or dilute, as in a gas, the electric field interacts with the charged particles, atoms, or molecules. The incident electric field causes a separation of charge or an induced dipole, and this dipole responds to the oscillating incident field by oscillating itself . As accelerating charges isotropically radiate electromagnetic radiation, radiation secondary to the incident light is emitted from the oscillating dipoles. The secondary radiation is termed *scattered radiation*. A single particle can also be imagined as an aggregation of tiny dipolar radiators. These dipole radiators are driven by the oscillating electric field of incident radiation and subsequently re-radiate light. Scattering by such an array of radiators depends on its geometry, observation angle (scattering angle), its composition, and properties of the incident radiation.

A particle is made up of many atoms and can be adequately described in macroscopic terms (i.e. by parameters like permeability and permittivity). Single molecules are not particles even though scattering by them is similar in some ways to that of particles. Scattering by a single particle is described best by wave mechanics, where as scattering by arrays of incoherent particles is best described by quantum optics. The distinction between multiple and single scattering events is more difficult in practice than in theory. When an isolated single scatterer exists in vacuum and is illuminated by a remote source, it can be approximated as a single scatterer. A single particle is a coherent array of many molecules, but can be a part of an incoherent array of many particles. Scattering from such an array may lead to phases scattered by each particle canceling each other, but multiple scattering is not always negligible and is not just scaled up single scattering (Born & Wolf, 1999)(Hulst, 1981). Scattering is a vast field, the picture given here provides some theoretical insight to allow selecting a specific nanoparticle system for a particular experiment and instrumental setup (Hecht, 2002).

The german physicist Gustav Mie was the first to derive the extinction spectra (extinction is scattering plus absorption) of spherical particles of an arbitrary size from Maxwell's equations at the beginning of the nineteenth century; Mie's theory has been

used widely since. These classical references, as well as a concise history of the "optical theorem" in scattering that covers roughly a century worth of work, are given in the references at the end of the proposal.

The energy carried in incident radiation can be dissipated, or absorbed, by the atoms or molecules it interacts with in nonradiative ways. This loss of radiation is termed absorption. The total attenuation of incident radiation, called extinction, is the sum of the scattered and absorbed light and is often expressed in terms of scattering and absorption cross sections such as

$$\sigma_{\text{total}} = \sigma_{\text{scattered}} + \sigma_{\text{absorption}} \equiv \text{extinction} \tag{2.14}$$

where the total cross section also equals the commonly used extinction cross section. The extinction cross section gives the rate at which energy is removed from an incoming beam of light due to scattering and absorption in a closed surface surrounding the scatterer via the so-called "optical theorem". It is of note that there are a variety of semiredundant ways to present extinction measurements. Twelve of these are shown in the Table 2.1. The extinction cross section of a homogeneous sample multiplied by the number density gives the extinction constant. The extinction constant, related to the molar absorptivity or (molar) extinction coefficient via Avogadro's number, can be used in the familiar Beer-Lambert law (equation: 2.15) to compute the attenuation of light traveling through a sample (neglecting multiple-scattering events).

$$T = \frac{I}{I_0} = 10^{-\alpha l} = 10^{-\varepsilon l} = 10^{-\varepsilon l c} \tag{2.15}$$

where I is the intensity of transmitted light, I_0 is the intensity of incident light, α is the absorption coefficient, ε is the molar concentration, l is the distance the light travels, and c is the concentration of absorbing species.

The absorption, scattering, and extinction cross sections of any spherical particle can be calculated using Mie theory, provided sufficient information about the wavelength dependence of the dielectric constants of the particle and the surrounding medium exists.

17

Transmittance, T	$T = I/I_0$
Extinction, E	$E = 1-T$
Extinction	$\text{Extinction} = log(I/I_0)$
Optical Density, OD	$OD = log(I_0/I) \, or \, ln(I_0/I)$
Absorbance, a	$a = I_a/I_0$
Absorbance, A	$log_{10}(I_0/I_a)$
Absorption/extinction/scattering constant $\gamma_a, \gamma_e, \gamma_s (cm^{-1})$	$I = I_0 exp(-\gamma_i Z)$
Absorption coefficient, k $(n = n_r + ik)$	$(4\pi k/\lambda) = \gamma_a$
Absorption index, κ	$n_r + ik = n_r(1 + i\kappa)$
Absorption/extinction/scattering cross sections $\sigma_{abs}/\sigma_{extinction}/\sigma_{scattered}(m^2)$	$\gamma_i = N\sigma_i$, where N is the number density and γ_i is used in definition above
Absorption/extinction/scattering efficiencies	$\text{Efficiency}_i = \sigma_i/\pi R^2_{GEO}$, where R_{GEO} is the geometric cross section of the particles.
Imaginary part of the dielectric function	$\varepsilon_2 = 2n_r k$
Optical conductivity	$\Sigma = \omega\varepsilon_2/4\pi$

Table 2.1. Different ways to present extinction data.
(Kreibig & Vollmer., 1995)

Briefly summarizing, according to Mie theory, the extinction and scattering cross sections, integrated over all angles (θ, Φ), can be expressed as

$$\sigma_{extinction} = \frac{2\pi}{k^2} Re(a_n + b_n), \tag{2.16}$$

$$\sigma_{scattered} = \frac{2\pi}{k^2} \sum_{i=1}^{\infty}(2n+1)(|a_n|^2 + |b_n|^2), \tag{2.17}$$

where $k = 2\pi/\lambda_0$. Substituting Equations 2.16 and 2.17 into 2.14 gives the absorption cross section. In Equations 2.16 and 2.17 the coefficients a_n and b_n are given as

$$a_n = \frac{\mu m^2 j_n(mx)[xj_n(x)]' - \mu_1 j_n(x)[mxj_n(mx)]'}{\mu m^2 j_n(mx)[xh_n^{(1)}(x)]' - \mu_1 h_n^{(1)}(x)[mxj_n(mx)]'}, \tag{2.18}$$

$$b_n = \frac{\mu_1 j_n(mx)[xj_n(x)]' - \mu j_n(x)[mxj_n(mx)]'}{\mu_1 j_n(mx)[xh_n^{(1)}(x)]' - \mu h_n^{(1)}(x)[mxj_n(mx)]'}, \tag{2.19}$$

where the $h_n s$ and $j_n s$ are spherical Hankel and Bessel functions of the first kind, respectively, m is the relative index of refraction ($m = n_p/n_m$), μ and μ_1 refer to the magnetic permeability of the medium and the particle, respectively, and $x = ka$ the size parameter. While these equations are cumbersome to evaluate, there are a number of software

packages available that utilize the fact that the terms in the infinite series of Equation 2.17 converge quickly yielding accurate numerical results.

2.3.1 Simplifications for Nanosized Particles

Mie theory makes it possible to obtain exact extinction spectra for arbitrary spherical particles but the formula does not allow for direct insight into absorption and scattering phenomena. For subwavelength-sized metal nanoparticles, an aggregation allows for considerable simplification of the mathematical formalism. Specifically, within the limits of the Rayleigh approximation, a particle is considered small relative to the wavelength of light when

$$\frac{2\pi a}{\lambda_0} n_p \ll 1, \tag{2.20}$$

where a is the radius of the particle, n_p is the complex index of refraction of the particle, and λ_0 is the vacuum wavelength. Below the Rayleigh limit, it can be shown that for a spherical dielectric nanoparticle, the absorption and scattering cross sections, integrated over all scattering angles, are:

$$\sigma_A = \frac{8R^3}{\pi\lambda_0} \left(\frac{m^2 - 1}{m^2 + 2}\right), \tag{2.21}$$

$$\sigma_S = \frac{8\pi R^6}{3} \left(\frac{2\pi n_m}{\lambda_0}\right)^4 \left(\frac{m^2 - 1}{m^2 + 2}\right)^2, \tag{2.22}$$

where $m = n_p/n_m$ is the ratio of the index of refraction of the particle to that of the medium, λ_0 is the vacuum wavelength, and R is the radius of the particle. An important point to note in Equations 2.21 and 2.22 is the strong dependence of the absorption and scattering cross sections on size of the particle if one assumes the dielectric properties of the particles are the same as the bulk values. It also important to point out that σ_A increases as R^3, where as σ_S increases as R^6. This suggests that for most nanoparticles below 100nm, absorbance dominates scattering. This section on light scattering was written by referring to, Bohren & Huffman (1983), Born & Wolf (1999), Hulst (1981), Hecht (2002), Kreibig & Vollmer. (1995).

2.4 Absorption of Light by Metal Nanoparticles

Absorption and scattering go hand in hand. Light which is not scattered is absorbed. In the case of metal nanoparticles, absorbed light is readily converted into heat because of the presence of a large number of free electrons. These free electrons may be excited by the incident light and when the frequency of the incident light matches with the natural frequency of the valence electron, resonance conditions prevails (Zeng *et al.*, 2011). Absorption becomes strongly enhanced under Plasmon resonance, that is when incident laser frequency matches the collective resonance of a nanoparticle (NP). To measure the number of photons emitted after photon absorption, the optical quantum yield is calculated. Optical quantum yield define as the ratio of photons emitted to the photons absorbed. Metal NPs have a very low optical quantum yield (i.e. they are very poor light emitters). The majority of light absorbed is converted to heat and the total amount of heat generated can be estimated in a relatively simple way as the total optical absorption rate. Crystalline nanoparticles of various materials like gold, silver, cadmium etc., can release heat under optical excitation. The mechanism for heat release under optical excitation is straight forward. The electric field in the light source such as a laser excites the mobile charge carriers in the nanocrystals. The energy gained by the nanocrystals is converted into heat which then diffuses into the surrounding matrix, resulting in an elevated temperature of the surrounding matrix. Conversely, heat generation for semiconductor nanoparticles is low because of an interband absorption process leading to formation of electron and hole pairs. In the absence of phase transformation of the particle, the temperature distribution around optically-stimulated NPs is described by the usual heat transfer equation as:

$$\rho(r)C(r)\frac{\partial T(r,t)}{\partial t} = \Delta k(r)\Delta T(r,t) + Q(r,t) \qquad (2.23)$$

Where t = time, r is a radial coordinate, $T(r,t)$ = local temperature, $\rho(r)$ = mass density, $C(r)$ = specific heat, $k(r)$ = thermal conductivity and $Q(r,t)$ = Energy source from light dissipating into nanoparticles ($Q(r,t) = \langle j(r,t)E(r,t)\rangle_t$), where $E(r,t)$ = stimulating electric field,

and $j(r,t)$= current density. The electric field is calculated using Maxwell's equations. In the steady-state regime, the local temperature around a single NP is described by:

$$\Delta T(r) = \frac{V_{NP}Q}{4\pi K_0 r} \qquad (2.24)$$

Where K_0= thermal conductivity of the surrounding medium, V_{NP}= volume of nanoparticle, and R_{NP}= radius of the nanoparticle. This equation is valid outside the nanoparticle i.e $r > R_{NP}$. The surrounding medium may be anything, including water, a chemical solution, or a polymer and it is possible to analytically calculate the heat generation Q, (assumption is $\lambda \gg R_{NP}$):

$$Q = \frac{\omega}{8\pi}E_0^2 \left| \frac{3\varepsilon_0}{2\varepsilon_0 + \varepsilon_{NP}} \right|^2 Im\varepsilon_{NP} \qquad (2.25)$$

Where ε_0 = is the dielectric constant of the surrounding medium, ε_{NP} = is the dielectric constant of the nanoparticle, and E_0 is the amplitude of the incident radiation. The
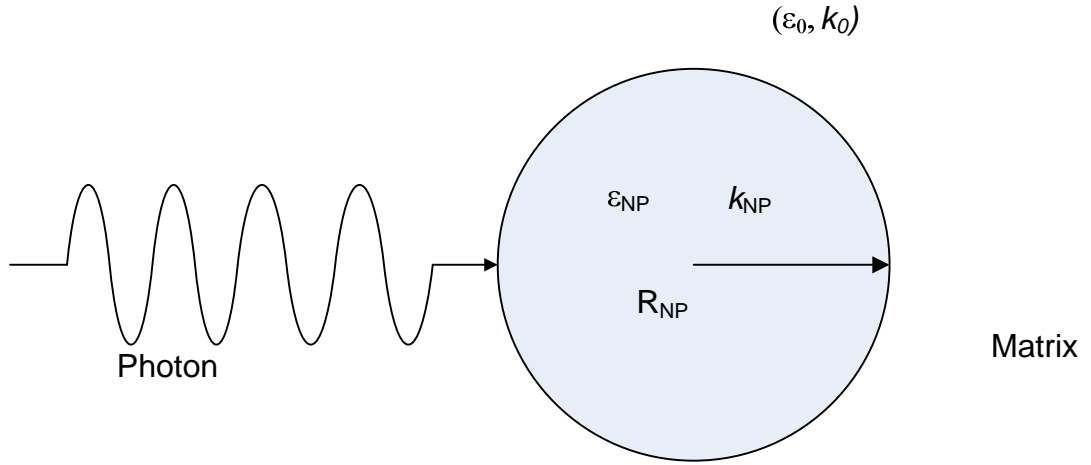
Figure 2.4. Sketch of an optically driven nanoparticle.

maximum temperature increase occurs at $r = R_{NP}$, the nanoparticle surface, and is given by:

$$\Delta T_{max}(I_0) = \frac{R_{NP}^2}{3K_0}\frac{\omega}{8\pi} \left| \frac{3\varepsilon_0}{2\varepsilon_0 + \varepsilon_{NP}} \right|^2 Im\varepsilon_{NP} \frac{8\pi I_0}{c\varepsilon_0^{0.5}} \qquad (2.26)$$

21

where I_0 = light intensity inside the matrix. This equation shows the important dependence of temperature on the NP size. This section on light absorbtion by metal nanoparticles was written referring to Govorov & Richardson (2007).

In the present work, LIS were made by focusing a laser via an objective lens. To understand the behavior of light after focusing, and to know the size of a tightly focused laser beam spot, one has to understand the topic of optical diffraction, which is presented in the next section.

2.5 Optical Diffraction

The fundamental maximum resolution of any optical system is dictated by optical diffraction. Electromagnetic waves from a source radiate in the form of ever-widening circles until they come in contact with a solid object, at which point another series of waves is radiated from the edge of the object. This results in a new source of waves that merge with the original waves so that the light now appears to bend around the corner, this bending of light is called diffraction. When an electromagnetic wave undergoes diffraction at the edge of an object, the diffracted waves interfere with the initial wave front giving raise to non-sharp images of the edge of the object being irradiated. Optical diffraction can be understood by observing light passing through a slit, shown in Figure 2.5. When light passes through an objective it undergoes similar optical diffraction as in the case of diffraction through a single slit. In addition, other principles apply when it travels from one medium to another.

A point object in a microscope, when imaged, generates an image that consists of a diffraction pattern created by interference. This image when magnified, contains a diffraction pattern consisting of a central spot surrounded by a series of diffraction rings. This point source diffraction pattern is referred to as an Airy disk, the axial dimension of an airy disk forms elliptical pattern, commonly known as point spread function (PSF).

22

The radius of the central spot in the Airy pattern was first estimated by Ernst Abbe in 1873 and is given by the following equation:

$$d = \frac{\lambda}{2nsin\theta} \tag{2.27}$$

where λ is wavelength of light used for imaging, n is refractive index of the medium between the objective and the sample, and θ is the half angle over which light is gathered by the objective. Rayleigh further developed Abbe's theory and proposed the criteria for resolving two point sources placed close to each other. According to Rayleigh theory, the limiting distance is when the principal maximum of the Airy pattern of one point source touches the first minimum of the second point source and is given by the equation:

$$Rayleigh resolution = \frac{0.61\lambda}{nsin\theta} \tag{2.28}$$

In the present work, the Rayleigh criteria was used to determine the waist of the beam for calculating the total flux out of the objective.

2.6 Theoretical Study of Heating of Spherical Nanoparticle in Thin Film by Continuous Wave Laser Irradiation

As discussed in Section 2.4, when a focused laser beam interacts with a metal nanoparticle, a large portion of the laser radiation is absorbed by the particle and is efficiently converted into heat. In this section, the process of light to heat conversion and dissipation of heat to the surroundings of the particle is quantified using quasi-steady state energy balance equations.

Specifically the following section provides a theoretical investigation of the heating of a spherical Ag metal particle embedded in a polymer, upon exposure to intense continuous wave (CW) laser radiation. The solutions are obtained for a quasi-steady state condition for distributions of temperature inside, at the particle surface, and conductive heat transfer between the particle and the surrounding thin film medium for assuming non-temperature

23
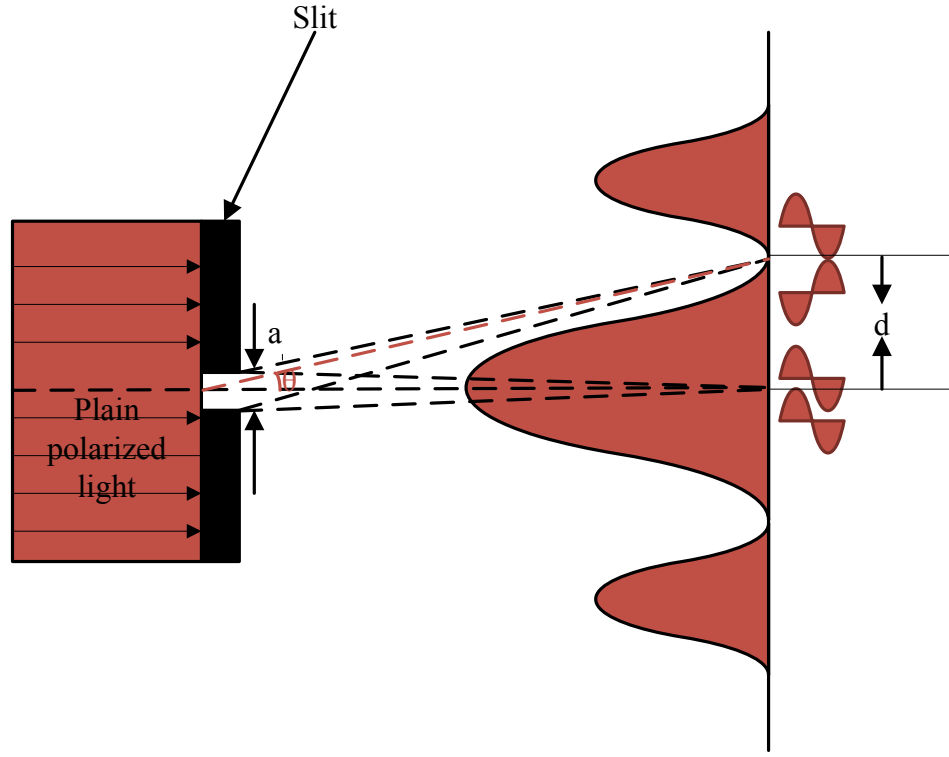
Figure 2.5. Single slit diffraction.

dependent heat transfer coefficients. Comparison of predicted results with experimental data was not done for the system of interest (Ag in a thin film) but a similar prediction and comparison with the experimental data was done for Au metal nanoparticles in the literature and they were in good agreement (Kurita *et al.*, 1998; MafunÃľ *et al.*, 2003; Hartland *et al.*, 2003).

Suppose laser radiation with wavelength λ, and intensity I_0 is incident starting from time t = 0, on a spherical solid (metal) particle with the radius r_0, and initial temperature T_∞ (equal to the surrounding medium temperature). The particle absorbs the radiation energy and becomes heated. Within the range $T_\infty < T_0 < 0.8 T_{ev}$ (where T_{ev} is the boiling point of Ag metal which is 2435K), the process of evaporation of the metal particle can be neglected because the vapor pressure of the material (Ag) is less than 1% of the vapor pressure value at $T = T_{ev}$ (Johnson & Christy, 1972) and the particle gives up its heat to

the surrounding media by conduction. The processes of the heating of spherical particles, which absorb laser radiation energy, and of heat transfer between the particles and the surrounding medium, with no mass transfer, can be described by:

$$\rho_0 c_0 \frac{\partial T}{\partial t} = div(k_0(T)gradT) + q_0 \tag{2.29}$$

with intial and boundary conditions $T(r \leq r_0, t = 0) = T_\infty$, $-(k_0(T)gradT)_{sp} = J_\varepsilon$, $T(r = r_0) = T_0$, where t is the time, T is the temperature, r is the radius with the origin at the center of the particle, ρ_0 is the density, c_0 is the specific heat capacity of the particle material, k_0 is the coefficient of thermal conductivity of the particle (Ag), J_ε is the energy going out of particle surface, and subscript "sp" denotes the surface of the particle. The power density of energy generation in the particle due to laser radiation absorption is denoted by q_0 and is assumed constant all around the particle for $2\pi r_0/\lambda < 1$.

Employing the quasi-steady state approximation, the analytical solution (for equation: 2.29) for the distribution of temperature inside the particle given is given by:

For $b \neq -1$,

$$T = T_0 \left(1 + \frac{q_0(r_0^2 - r^2)(b+1)T_\infty^b}{6k_{0\infty}T_0^{b+1}} \right)^{1/b+1} \tag{2.30}$$

For $b = -1$,

$$T = T_0 exp \left(\frac{q_0(r_0^2 - r^2)}{6k_{0\infty}T_\infty} \right) \tag{2.31}$$

Where the temperature dependency of the conduction coefficient is given by using a power law: $k_0 = k_{0\infty}(T/T_\infty)^b$, where $k_{0\infty} = k_0(T = T_\infty)$, index b=constant (for Au b=0.5 in the range 273<T<2000K). The temperature dependence of the conduction coefficient of the surrounding material can be similarly given as: $k = k_\infty(T/T_\infty)^a$, where $k_\infty = k(T = T_\infty)$, a=constant (for air a=1.5 in the range 273<T<2000K) (Vargaftik, 1972). Similarly for the quasi-stationary condition, the temperature distribution around the particle can be given using the following equations, which were derived in Pustovalov & Bobuchenko (1989),

For $a \neq -1$,

$$T(r) = T_\infty \left[1 + \frac{r_0}{r} \left(\left(\frac{T_0}{T_\infty} \right)^{a+1} - 1 \right) \right] \tag{2.32}$$

25

For $a = -1$,

$$T(r) = T_\infty \left(\frac{T_0}{T_\infty} \right)^{r_0/r} \tag{2.33}$$

To estimate the surface temperature (T_0) of the particle, Equation 2.29 must be integrated over the entire volume of the sphere and has the form:

$$\rho_0 c_0 V_0 \frac{dT_0}{dt} = \frac{1}{4} I_0(t) Q_{abs} S_0 - J_\varepsilon S_0 \tag{2.34}$$

with the initial condition $T_0(t = 0) = T_\infty$

$$\int_0^{r_0} q_0(t) 4\pi r^2 dr = \frac{1}{4} I_0(t) Q_{abs} S_0 \tag{2.35}$$

where $V_0 = \frac{4}{3}\pi r_0^3$, $S_0 = 4\pi r_0^2$, $Q_{abs}(\lambda, r_0)$ is the absorption efficiency of the particle and was calculated using Mie plot software (Laven, 2013). The energy removed from the particle surface is the sum of conduction and radiation losses ($J_\varepsilon = J_c + J_r$). Radiation losses are only significant at higher temperatures and for simplicity, assuming the surface temperature doesn't go very high then the only loss term is conduction, which is given using Fourier's law of heat conduction:

$$J_c = -\left(k(T) \frac{dT}{dr} \right)_{sp} \tag{2.36}$$

Substituting the temperature distribution, Equation 2.32 and 2.33, into Fourier's law of heat conduction, Equation 2.36, results in the following expression:

For $a \neq -1$,

$$J_c = \frac{k_\infty T_\infty}{(a+1)r_0} \left[\left(\frac{T_0}{T_\infty} \right)^{(a+1)} - 1 \right] \tag{2.37}$$

For $a = -1$,

$$J_c = \frac{k_\infty T_\infty}{r_0} ln \frac{T_0}{T_\infty} \tag{2.38}$$

Substituting the expression for J_c into Equation 2.29 results in an estimate of the surface temperature. For two different a values the expression reduces to:

For a=0,

$$T_0 = T_\infty + \frac{I_0 Q_{abs} r_0}{4k_\infty} [1 - exp(-Bt)] \tag{2.39}$$

26

For a=1,

$$T_0 = T_\infty A \frac{A + 1 - (A - 1)exp(-ABt)}{A + 1 + (A - 1)exp(-ABt)} \qquad (2.40)$$

where $A = \left(\frac{I_0 Q_{abs} r_0}{2 k_\infty T_\infty} + 1 \right)^{0.5}$, $B = \frac{3 k_\infty}{c_0 \rho_0 r_0^2}$. The equations described in this section were used to estimate the temperature profile around different sized Ag particles (Figure 2.6), using MATHCAD software. The relevant worksheet is attached to Appendix E. The graph
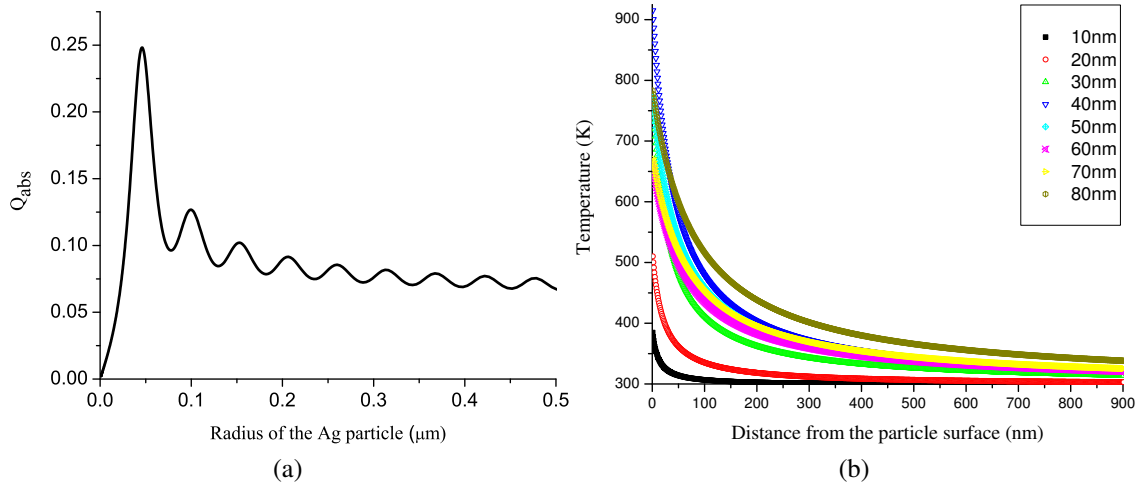
Figure 2.6. Absorption efficiency of different size Ag particles and temperature profile around them. Absorption efficiency (a). Temperature profile (b).

of Figure 2.6a is of absorption efficiency versus the radius of Ag nanoparticles. It shows the absorption efficiency increases up to a radius of 45nm and then drops. The curve has an oscillating nature to it. These absorption efficiency values were used to calculate the surface temperatures of the particles, and are shown in the Figure 2.6b. The curve for 40nm radius Ag particles has the highest surface temperature compared to other size Ag particles, a fact attributed to the maximum in the absorption efficiency.

2.7   Thermal Paper

As the present body of work is related to light absorption and the conversion of light energy into heat by metal nanoparticle structures, it is instructive to consider other tech-

niques which use heat to form patterns. One well established printing technology which uses heat to print is the Thermal Printing Technique. Thermal paper technology was first developed in the 1930's and since then it has grown into two main divisions, heat transfer systems and two-component systems. In heat transfer systems, in order to obtain a gray scale image, the Dithering Method is used. Higher order color images are obtained by sublimate-transfer in which the amount of dye transferred to the receiving layer is controlled and proportional to the input energy of the thermal head. In two-component systems, there are at least two components that are heated and combined to form an image. In this category chelate type thermal paper was the first and used metallic acids. Images obtained by this reaction are very stable and chelate pigments absorb near infrared light, making them useful for IR bar code scanners. The disadvantage of this method is low light sensitivity and the background has a greenish tint. Improving on this approach, NCR (NCR is global technology company) in the 1960's developed leuco dye and phenolic acid based thermal paper. It is currently the most widely used thermal paper; the reaction for image formation is shown in Figure 2.7
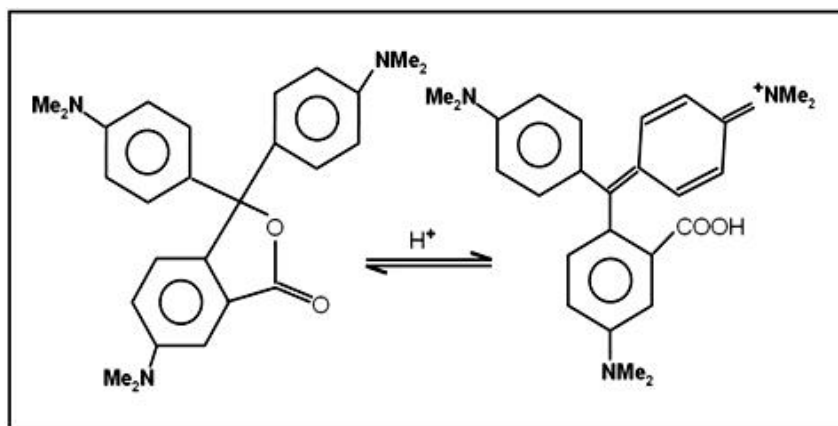
Figure 2.7. Color development in thermal printing.
(Watanabe & Kisaka, 1993)

Thermal recording systems have many advantages over other printing techniques, such as low maintenance, the small size of the equipment, and the low cost of the thermal

paper. As with any other technology, it also has some disadvantages, high surface gloss makes thermal paper hard to read, the smooth surface makes it hard to write on by conventional means, and images tend to fade through interaction with skin oil and are easily scratched. These difficulties have been overcome by the development of Plain Thermax (PTM). PTM is a three layer thermal paper, each layer adds an extra feature to its plain paper characteristics. Layer 1 is Base paper; to achieve plain paper texture a hard paper must be used. The typical thickness of paper used is in the range of 70 to 90μm. The second layer is a base coat, which affects the paper's resolution (print resolution) and optical density. Oil absorbing pigments are used in the base coat to get high sensitivity and resolution. Additionally, it acts as an insulating layer and prevents energy loss from the thermal head. The third layer is called an over coat, which acts as a protecting layer from abrasion and dirt. The over coat also makes it easy to read and write, whereas a binder in the coat offers resistance to water. Various other chemicals are added to increase ink set and reduce thermal head abrasion. The thermal sensitivity of the paper is increased by decreasing the size of the leuco dye. It is reported in the literature that decreasing the size of leuco dye from 1.5μm to 0.8μm will reduce the energy consumption of the thermal head by 30%. Since the reaction between the leuco dye and phenolic acid is reversible, images developed by this reaction fade over time. To overcome this image instability problem, a compound with an epoxy functional group (consisting of an oxygen atom joined by single bonds to two adjacent carbon atoms) is added to the heat sensitive layer. The epoxy based compound forms an intermediate compound, which acts as a catalyst and makes the reaction irreversible. Other special thermal papers:

1. Two Color Thermal Paper: In this type of thermal paper there are two heat sensitive layers with different melting points and developing colors. The first color comes from an upper layer which melts at a lower temperature than the layer underneath it and a second color is developed when both layers are melted.

2. High Quality Thermal Paper: In this thermal paper, synthetic paper is used as the base paper which helps in superior dot reproducibility due to its smooth texture.

3. IR Readable Thermal Paper: uses leuco dye in a heat sensitive layer, which absorbs infrared light. This makes them very popular for point of sale and inventory control uses.

4. Translucent Thermal Paper: uses polyester/polypropylene as its base sheet. Its translucent nature is used in thermal plotters, as it can be used to superimpose/overlay. Approximately 230 tons per month of thermal paper is produced worldwide and there is a constant demand for new types of thermal paper for emerging applications.

This section on thermal paper was written by reviewing Watanabe & Kisaka (1993)

2.8 Printing Techniques

Since the major portion of this thesis addresses the formation of LIS, it will be worth while to review other methods that exist to make structures. One of the most popular ways to make patterns on a large scale is printing.

The four most important printing techniques use a master pattern for image transfer. These are: Flexography, Gravure, Lithography, and Screen printing. People have considered Gravure, Lithography, and Flexography techniques suitable for printing electronics, whereas Screen printing is a thick film process and is used in the production of printed circuit boards.

2.8.1 Flexography

Flexography can be imagined as a rubber stamp on a roll. The raised surface is provided with ink and then the ink is transferred to the substrate. The advantage with this technique is that it is easy to make the rubber printing form, which makes it attractive for

a laboratory printing technique. A significant disadvantage is deformation of the rubber printing form leading to print defects. Limitations also exist with regard to compatability of the printing material and the type of solvent based inks used, since organic based ink can cause swelling of polymer printing forms.

2.8.2 Gravure

The Gravure technique can be imagined as the inverse of the flexography process. In the Gravure process a pattern is etched into the surface to make the print form, these etched patterns (wells) hold ink when provided with one. A doctor blade provided in the setup removes ink from non patterned areas. The ink from the wells are then transferred to the substrate. The advantages of this technique are its very high print resolution, no deformation/swelling, and high print speed. Disadvantages include the high cost and slow speed to pattern Gravure rolls, making it less suitable for prints which change day-to-day. The direct gravure method is less suitable for printing on solid substrates and to overcome this, offset gravure is used, which reduces the resolution.

2.8.3 Lithography

Of the various lithography techniques, offset lithography is the most commonly used. In this technique the printing form has hydrophilic and hydrophobic regions. Firstly, the printing form is dampened with water; the hydrophilic regions of the printing form are covered with water and then the print form is provided with hydrophobic ink, which adheres to the hydrophobic regions of the print form. This pattern of water and ink on the print form is transferred to an intermediate cylinder (offset roll) and then to the substrate. The water region on the print form helps in avoiding spreading of ink while the pattern is absorbed by the paper substrate. A disadvantage of this technique particularly for printed electronics, is the use of two fluids to print one pattern, which may lead to cross contamination. Additionally problems in design control, the fact that most substrates used

in the electronics industry are non-absorbent and the use of an offset cylinder, which may lead to a loss of pattern precision, exist.
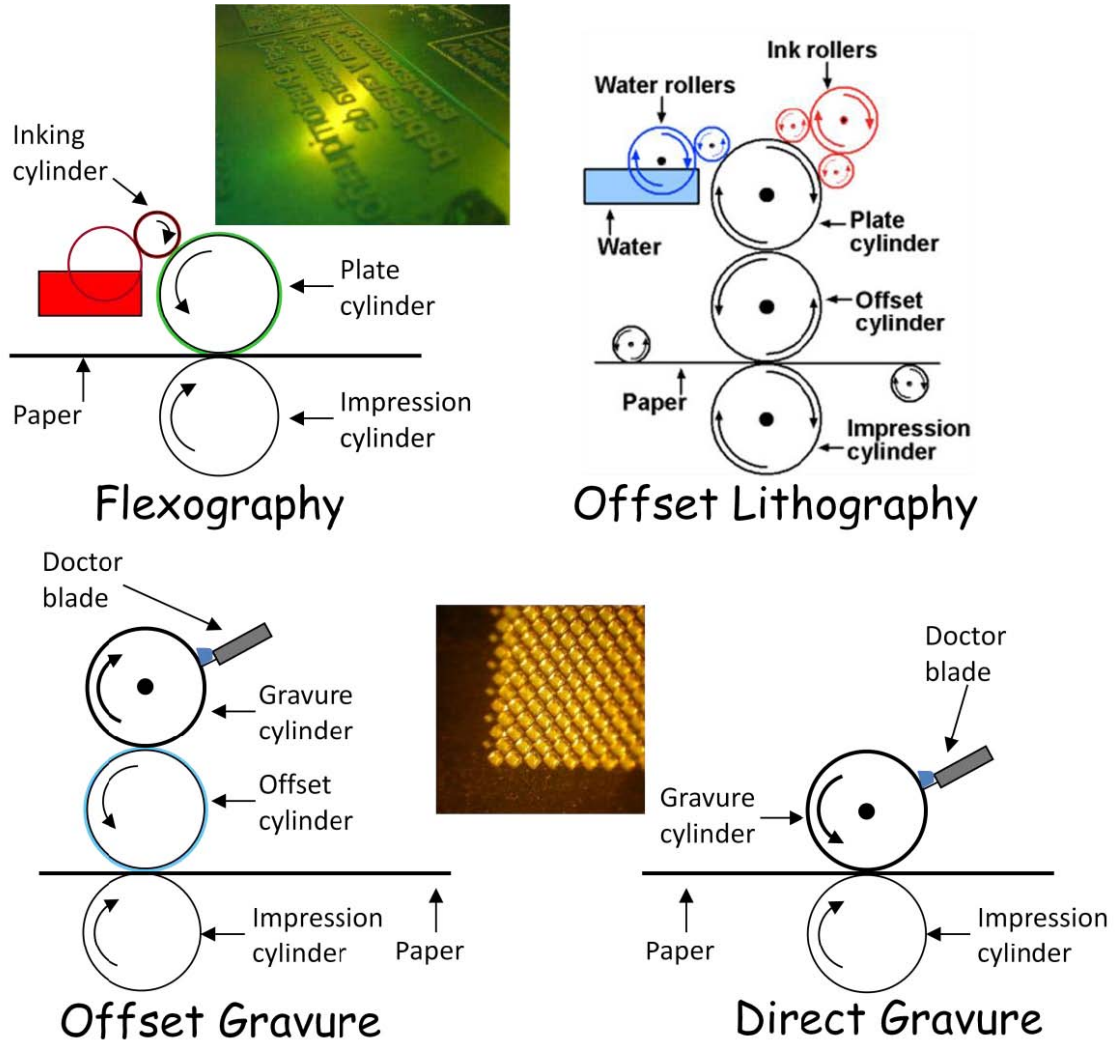
Figure 2.8. Well-known printing processes. Inset photographs of a gravure roll (bottom middle). Flexography roll (top left).
(la Fuente Vornbrock, 2009)

2.9   Mechanism Behind Light Induced Structure Formation

In this section of the the literature review, the processes which are known to contribute to LIS formation under various conditions are being reviewed. Three important phenom-

ena which are likely occurring during or leading to LIS formation are optical trapping, sintering, and liquid melt ejection.

2.9.1 Optical Trapping

This section gives a brief overview of the optical trapping process by referring to a review article Neuman & Block (2004).

Optical Trapping was first observed during the early 1970's by Arthur Ashkin. Ashkin showed how micron sized particles could be displaced and levitated in different media. He was able to make a 3-Dimensional optical trap using counter propagating laser beams, which lead to the development of single-beam gradient optical tweezers, or optical traps. Optical trapping has been extensively used in physics and biology for cooling and trapping single atoms, and for manipulating viruses and bacteria. It has been used to apply PecoNewton forces and simultaneously measure the resulting displacement with nanometer level precision to study molecular motors at the single molecule level. An optical trap is formed by the radiation pressure of a tightly focused laser beam employing an objective of high NA (numerical aperture). A dielectric particle near the focus will experience a force because of momentum transfer from the incident beam due to the scattering of incident photons. This force, referred to as an optical force, may be deconvoluted into two components: (1) a gradient force in the direction of the spatial light gradient and (2) a scattering force in the direction of light propagation.

The scattering force can be imagined as a photon 'fire hose', pushing the particle in the direction of beam propagation. The incident photons hit the particle and scatter a portion of photons in all directions, while a portion is absorbed which leads to transfer of momentum to the particle. For isotropic scattering, the forces cancel in all directions except in the forward direction, which can be calculated from the scattering cross section of the particle. The second component of optical force is the gradient force which arises because of the force experienced by the dipole of the particle in the inhomogeneous

electric field of the laser beam. The fluctuating electric field of the laser beam induces a fluctuating dipole in the particle; it is the interaction of the fluctuating dipole with the electric field which leads to a gradient trapping force. This force depends on the intensity of the incident light and the polarizability of the particle.

In order for an optical trap to be stable, the gradient force must exceed the scattering force, which is possible for steep gradients of light produced by tight focusing of the incident beam to a diffraction limited spot using a high NA objective (refer to Section 2.5). As a result of the force balance between the two (gradient and scattering force), the axial equilibrium position of the trapped particle is located below the focal point of the incident beam. The gradient force is proportional to the displacements from the equilibrium position, the optical trap behaves like the Hookean spring whose optical trap stiffness is proportional to the beam intensity.

In the calculation of the optical trapping force for spherical particles, two limiting cases exist for which it is possible to calculate optical forces readily. When the trapped sphere is much larger than the wavelength of the trapping laser, the conditions for Mie scattering are satisfied and optical forces are calculated using ray tracing. i.e. Refraction of the incident light by the sphere changes the momentum carried by the light which in turn generates equal and opposite momentum in the particle. The rate of momentum change generates a force on the sphere which is proportional to the light intensity. If the refractive index of the sphere is greater than the surrounding medium, then the force will be in the direction of the incident beam gradient. The scattering component of the force arises from specular reflection and absorption of light by the trapped particle. The peripheral rays contribute dis-proportionally to the axial gradient force, whereas central rays contribute to the scattering force. Thus expanding the Gussian laser beam to slightly overfill the objective will result in increased trapping efficiency.

The second limiting case is when the trapped sphere is smaller than the wavelength of the trapping laser, under these conditions Rayleigh scattering is satisfied and the forces

are calculated considering the particle as a point dipole. In this case the scattering and the gradient force components are readily separated and the scattering component of the force is due to the absorption and reradiation of light by the dipole.
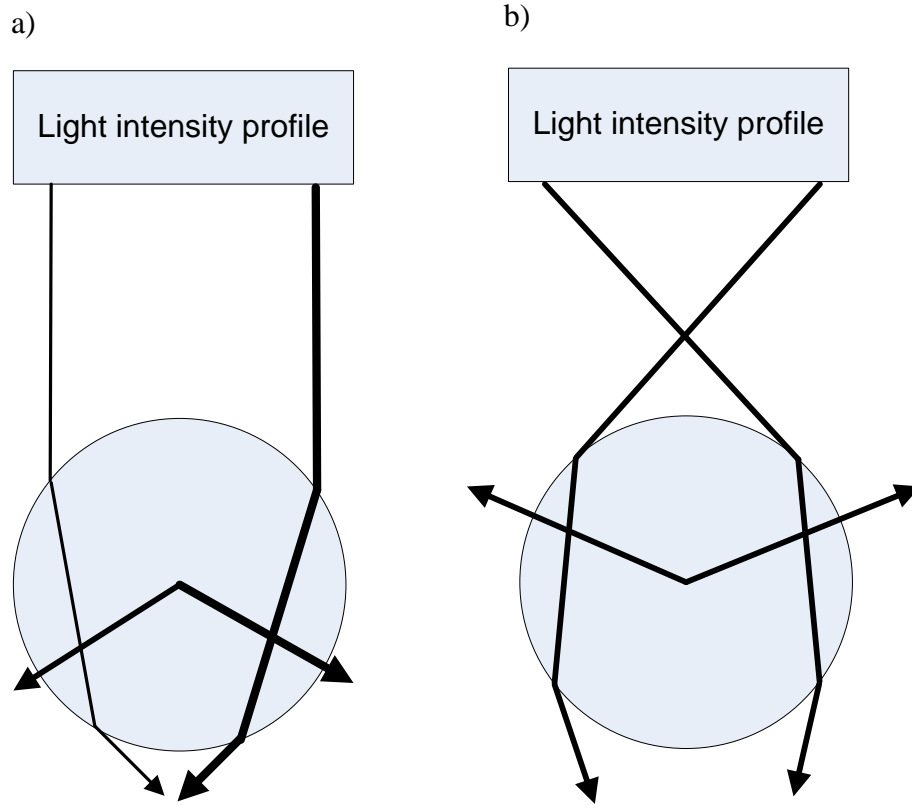
Figure 2.9. Describes axial gradient force in ray-optics regime.
(Neuman & Block, 2004)

Figure 2.9 presents the axial gradient force in the ray-optics regime. (a) A transparent bead is illuminated by a collimated beam with intensity increasing from left to right (dark thick line represent higher intensity). Refraction of the light beam changes its momentum, which is equivalent to a change in the direction of the input and output directions of the rays. Conservation of momentum dictates that the momentum of the bead changes in an equal but opposite in direction, which results in the force on the bead (shown by the gray arrow). The net force is to the right in the direction of the incident gradient.(b) In this figure a stable trap is shown, formed by the generation of a 3-dimensional intensity

gradient. In this case the bead is illuminated by a focused beam with a radial intensity gradient, where two representative beams are refracted by the bead and the change in momentum in this instance generates a force towards the focus (represented by gray arrows). The sideways forces cancel and the axial force is balanced by the scattering force (not shown), which fades away as the distance from the focus increases. For a sphere of radius a, the scattering force component is given by

$$F_{scat} = \frac{I_0 \sigma n_m}{c} \tag{2.41}$$

$$\sigma = \frac{128\pi^5 a^6}{3\lambda^4} \left(\frac{m^2-1}{m^2+2}\right)^2 \tag{2.42}$$

Where I_0= is the intensity of the incident light, σ= scattering cross section, n_m= index of refraction of the medium, c= speed of light in a vaccum, m= ratio of the index of refraction of the particle to the index of the medium (n_p/n_m), λ= wavelength of the trapping laser.

The gradient force is due to interaction of the induced dipole with the inhomogeneous field and is given by $F_{scat} = \left(\frac{2\pi\alpha}{cn_m^2}\right)\Delta I_0$ where $\alpha = n_m^2 a^3 \left(\frac{m^2-1}{m+2}\right)$ is the polarizability of the sphere. The gradient force is proportional to the intensity gradient and increases when $m > 1$. The final case is when the dimension of the trapped particle is approximately equal to the wave length of the trapping laser then neither ray-optics nor point dipole approximations are valid. Rather, complete electromagnetic theories are required to describe the situation.

2.9.2 Sintering

Sintering is based on atomic diffusion and is observed above absolute zero and is enhanced at higher temperatures. People have been making conductive micron structures through laser induced sintering of nanoparticle film (Aminuzzaman *et al.*, 2010). In this

section a brief overview of sintering of nanoparticles is given via reference to Song & Wen (2010).

Microscopic sintering of nanoparticles occurs because of surface motion and grain boundary motion. Such motion occurs in order to minimize the total sum of surface and grain boundary energy. A large number of studies have been carried out on the sintering processes of large particles, resulting in the proposal of many possible mechanisms such as surface diffusion, lattice diffusion from grain boundaries, and lattice diffusion through dislocation (P.Zeng *et al.*, 1998; Koparde & Cummings, 2005, 2008). Basic thermodynamic principles are applicable to nanoscale sintering, for example the Kelvin equation, which is the basis of classical sintering theory, is supported by nanoscale experimental evidence (Nanda *et al.*, 2002).The sintering process of nanoparticles is expected to be very significant from that of micrometer or millimeter sized particles due to the high surface to volume ratios, and large surface energies. The melting point of particles depends on their size and the relation between particle size and melting point, or melting associated properties such as vapor pressure, and is not linearly related and cannot be described by typical continuum equations. A large amount of both experimental and theoretical work has been performed on the sintering of metal oxide and metal nanoparticles including Au, Cu, Ni, TiO2, etc. (P.Zeng *et al.*, 1998; Koparde & Cummings, 2005, 2008; Zhu & Averback, 1996a,b; Raut *et al.*, 1998; Hendy *et al.*, 2003; Hawa & Zachariah, 2004; Arcidiacono *et al.*, 2004; Hawa & Zachariah, 2006; Panigrahi, 2007; Pawluk & Wang, 2007). Molecular Dynamics (M.D) has proved to be a robust method for quantitatively predicting nanoscale processes (Ding *et al.*, 2009), especially at the initial stages of nanoscale sintering, which usually happens within less than one nanosecond and is difficult to measure experimentally.

Many studies have shown that the sintering process is aided by smaller particle sizes with the major mechanisms being surface diffusion and grain boundary diffusion for the sintering of Cu and Au nanoparticles (P.Zeng *et al.*, 1998; Arcidiacono *et al.*, 2004; Wakai,

2006). There are however many contradictions and inconsistencies. Few studies have been conducted probing the kinetics of sintering; different regimes of sintering particles, such as the surface, neck and the core have not been distinguished clearly.

To investigate the basics of particle sintering, most workers employ two particles. Among the two particle sintering studies, a majority of studies have used two equal sized spherical particles. It is noted that in reality many practical systems involve a broad size distribution of particles. Hawa & Zachariah (2006) demonstrated that the deformation and convection processes dominate the sintering of liquid-like small particles, whereas a diffusion process dominates for solid-like large particles. Clearly the size dependency of the physical properties of nanoparticles makes sintering more complicated. So a proper and careful study of sintering is required. A single study has been performed on the kinetics of melting and sintering processes of two different sized nanoparticles using Molecular Dynamics simulations. In one experiment the sintering process was divided into regimes to understand sintering kinetics and the relation between surface melting and the sintering process.

A typical sintering scenario is depicted as in Figure 2.10. It starts with the formation of a neck as shown in Figure 2.10(b) which reaches the diameter of the smaller particle at about t = 50ps (Figure 2.10(c)) which is followed by a slow process, reaching full sintering at around 200ps, at which time the small particle becomes indistinguishable. These snapshots show clearly the progress of the sintering process. To quantify the sintering process, Gyration Radius, Mean Square Displacement (MSD), Root Mean Square Displacement (RMSD), Diffusivity and Activation Energy are used.

Pengxiang Song and Dongsheng Wen performed a MD study on two different size nickel nanoparticles (3.52nm and 1.76nm in dia). The conclusions of the MD simulations were, 1) The study of different stages (surface, neck, and the core) of nanoparticle sintering reveals that surface melting starts first and it propagates inwards as the heating temperature increases, which influences sintering significantly, 2) Mean square displace-
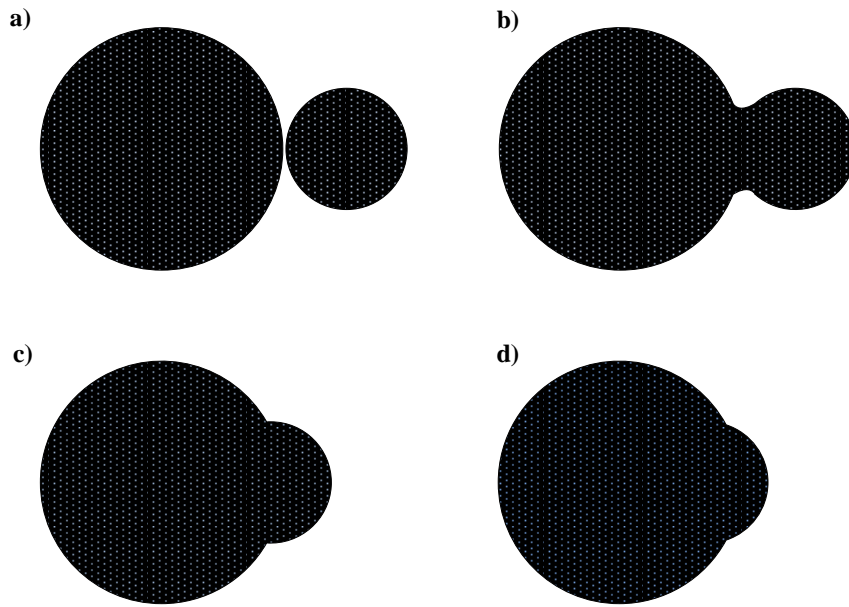
Figure 2.10. Sintering snapshots. Simulation time 0ps (a). 5ps (b). 50ps (c). 200ps (d).
(Song & Wen, 2010)

ment and gyration radius help in quantifying the three different regimes of sintering of metal nanoparticles, 3) The sintering diffusivity is regime and size dependent. It is higher at the surface and smaller for large particles. 4) Other than surface diffusion, factors that are significant for sintering of nanoparticles are grain boundary diffusion, viscous flow, surface tension gradient, and plastic deformation.

2.9.3   Liquid Melt Ejection

A schematic of melt ejection is shown in Figure 2.11 . A Gaussian profile laser beam is directed using an objective lens towards a nanoparticle based film, which absorbs a fraction of the incident light energy. The absorbed light is converted into heat by the metal nanoparticles, raising the temperature of the surrounding matrix. At a sufficiently high temperature, the material surrounding the nanoparticle melts and vaporizes. This melting followed by vaporization creates a back pressure on the liquid free surface of surrounding material melt, which in turn pushes the melt away in the radial direction. Thus the material is removed by a combination of vaporization and liquid expulsion. A

Knudsen layer exists adjacent to the liquid-vapor interface which is only a few microns thick. The Knudsen layer is defined as a small layer where the phase is between liquid and vapor, this region is several mean free path (of electron) lengths thick. On top of this layer, stacking in the vertical direction, lie the layers of vapor, disturbed air, and undisturbed quiescent air.
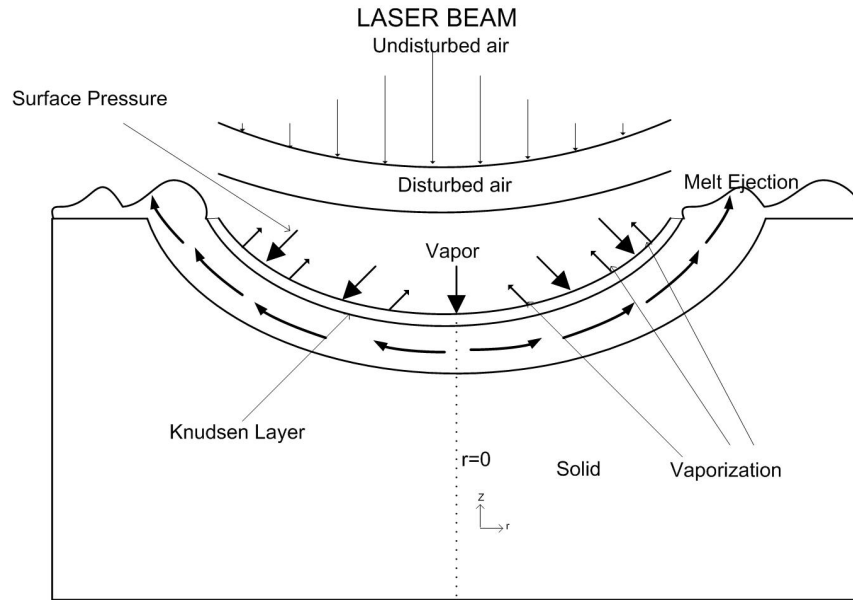
Figure 2.11. Schematic of melt ejection.
(Ganesh & Faghri, 1997)

Figure 2.12 presents a magnified version of Figure 2.11. In this figure the circles represent bubbles of vapor coming up from the melt pool (melted film of the material surrounding the nanoparticle). These bubbles burst, releasing hot vapor. The hot vapor tends to expand in all directions but faces resistance from the melt pool, thereby creating a pressure on the melt pool leading to pushing of the melt radially outward.

The liquid melt ejection mechanism seems to be a good fit for the LIS formation, as in the LIS, the material accumulated along the edges of the LIS (in the z-direction) has come from the central region of LIS, where a trough has been created.

Motion of vapor near the surface of a metal and transfer of momentum to a target from incident laser radiation: (Q) momentum vector of vaporized substance, (—Q) momentum imparted to solid target
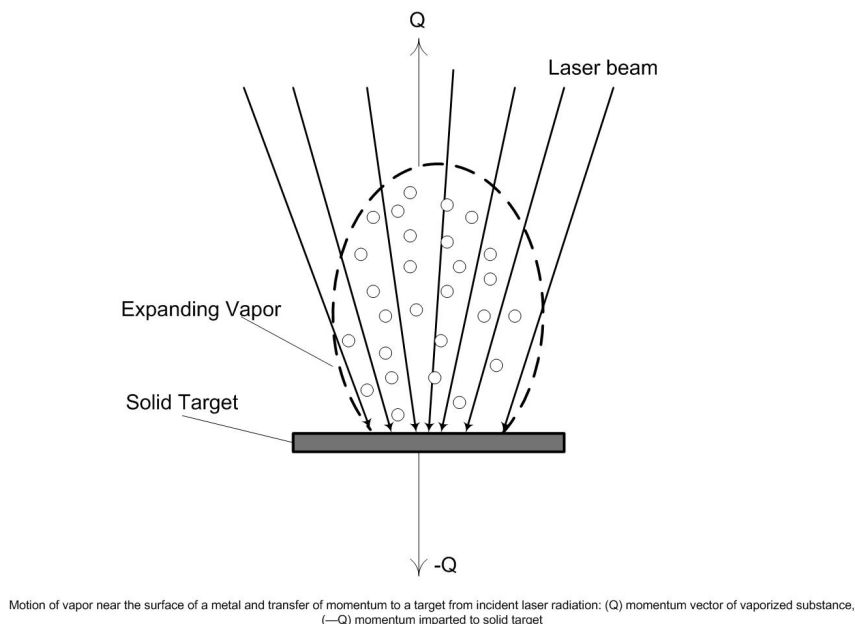
Figure 2.12. Magnified image of melt ejection.
(The Gale Group, 1970-1979)

2.9.3.1   Heating and Pressure Wave Generation

At the microscopic level, the nanoparticles encapsulated in excess citrate/polymer (in the drop cast film) absorbs the laser radiation and due to the metal nanoparticle's efficient phothermal conversion, photon energy is converted to heat. The heat generated is conducted across the nanoparticle and into the surrounding citrate/polymer molecule. The citrate molecule has water molecules attached to its structure, which on contact with heat is evaporated, generating pressure waves or expanding micro bubbles around the nanoparticle. The expanding bubble pushes the nanoparticles and melted citrate towards the sides of the laser beam incident location, creating a trough, which on straight line laser beam movement makes a straight line structure on the Ag nanoparticle-citrate film.
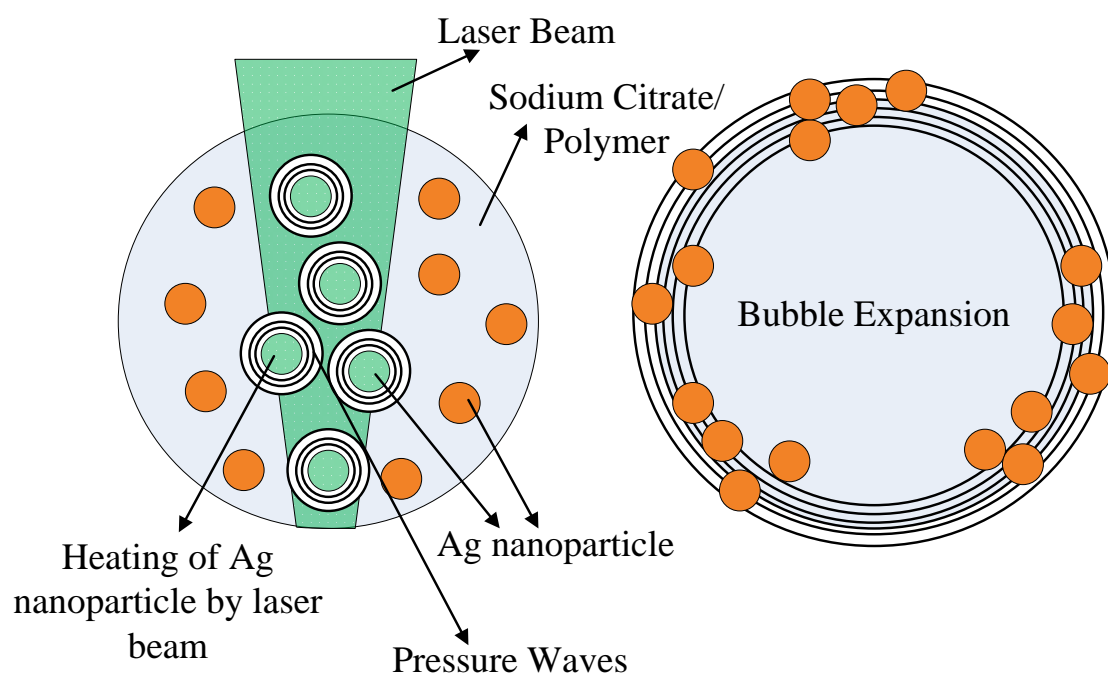
Figure 2.13. Pressure wave and bubble expansion during laser-nanoparticle interaction.

Chapter 3

EXPOSURE OF SILVER-SODIUM CITRATE DIHYDRATE NANOPARTICLE BASED FILM TO THE LASER

3.1 Introduction

The scientific community has made several structures employing high Ag nanoparticle content films using focused lasers (Rekstyte *et al.*, 2013; Aminuzzaman *et al.*, 2010). The mechanism for structure formation has been attributed predominantly to sintering, accompanied decomposition of organic surfactant. The work reported in this chapter differs in that it uses very low Ag nanoparticle content (Ag=25mg, dispersant= 600mg) (without any polymer matrix) films to make structures.

This chapter develops a LIS technique to create 3D structures on Ag nanoparticle based coatings using a 532nm CW laser source. A surprising result is that the LIS has the unique attribute of being inherently fluorescent, providing a utility not previously reported in the literature. The Ag nanoparticles were made in a wet synthesis technique, concentrated, and characterized. The concentrated Ag solution was used to generate drop cast films on glass slides which was then exposed to a focused laser beam to induce structure formation. The LIS structures were photo-physically characterized.

3.2 Materials and Methods

3.2.1 Synthesis of Ag Nanoparticle

Silver nanospheres were made using single-pot redox chemical techniques according to published material (Turkevich & Hillier, 1951; Pillai, 2004). Specifically a soluble metal salt (silver nitrate), a reducing agent (sodium citrate) and a stabilizing agent (excess sodium citrate) were used. The mechanism of formation is believed to commence with a

nucleation step, followed by nanoparticle growth and finally a stabilizing agent caps the particle leaving a negatively charged surface, helping to avoid aggregation (Rivas *et al.*, 2001).

The experimental process starts with cleaning all glassware with concentrated nitric acid, in order to remove any leftover nanoparticles from previous batch. Subsequently 600mg of sodium citrate is dissolved in 160 ml of $18.2 M\Omega.cm$ pure water in a 500 ml round bottom flask. This was then brought to a temperature of $95°C$ in an oil immersion bath. Simultaneously, 40mg of silver nitrate was dissolved in 40 ml of $18.2 M\Omega.cm$ ultra-pure water in a glass beaker. This was then added to the round bottom flask containing the sodium citrate solution and heated to the same temperature ($95°C$) under constant stirring. The sodium citrate acts as both a reducing and a stabilizing agent. The temperature was maintained until the reaction was complete, which takes approximately 45 minutes. The heating and the stirring were stopped and the solution allowed to cool to room temperature.

The size of the nanoparticles was measured using dynamic light scattering (DLS) (Malvern, Zetasizer Nano-ZS) and also using transmission electron microscopy and UV-Vis Spectroscopy. Figure 3.2a shows a transmission electron micrograph (TEM) of the as-prepared silver nanoparticles prior to use. From the image, the average diameter was estimated to be approximately 100 nm. Nanoparticle solutions synthesized using the method described above were too dilute in nature.

$$4Ag^+ + Na_3C_6H_5O_7.2H_2O \rightarrow 4Ag^0 + C_6H_5O_7H_3 + 3Na^+ + H^+ + O_2 \uparrow \qquad (3.1)$$
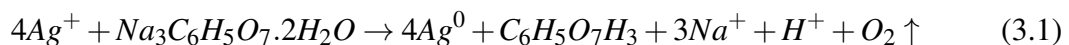
(Šileikaite *et al.*, 2006)

3.2.2 Nanoparticles Film Formation

To get continuous LIS on nanoparticle films, the nanoparticles required a closer proximity than possible with the films made from as prepared Ag solutions. To increase the
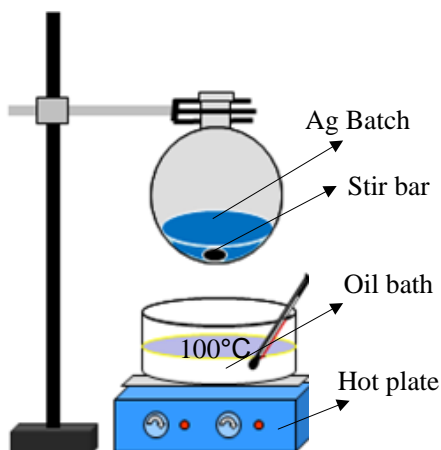
Figure 3.1. Ag synthesis setup.

number density of particles, the solution was subjected to rotation vaporization using a rotary evaporator (Rotovap) instrument (BUCHI Rotavapour R-205), with settings of 72mmHg pressure in the flask and a temperature of 95°C. The solution was concentrated from 0.013wt% to 0.102wt%; the solution was then characterized using DLS and UV-Vis spectroscopy. 100μl of this solution was drop cast onto a 22x22mm cover slip (Fisherfinest #1) and allowed to air dry slowly in a fume hood over a period of 8 hours. Spin coating was also employed to make Ag nanoparticle films on glass, however several problems were encountered including the problem sample wastage (90%), edge bead effects, and it took a large number of spin coated Ag nanoparticle films to get a response with the laser.

3.2.3 Formation of Line Features

Drop cast films were subjected to a 532nm CW diode pumped solid state (DPSS) laser using a custom built hybrid scanning confocal microscope (Figure 3.7). The film was scanned at a rate of 0.07 mm/sec under the laser in a raster pattern using a piezoelectric x-y scanning stage (i2, New England Affiliated Technologies, Inc.). The scan stage was controlled using custom built LabVIEW software. The instrument was equipped with a

broadband light source (Kohler illumination), widefield image collection optics, and a CCD camera (Princeton Instruments, SPEC-10) allowing for simultaneous observation of the film (120 μm x 160μm) during exposure.

3.2.4 Characterization of Line Features

In a separate measurement, using the same custom built instrument, localized fluorescence emission spectra were obtained at different morphological features within the LIS structure. In this case, 473 nm CW laser excitation (20 μW) was directed towards the sample with a broad band beamsplitter and focused to a diffraction limited spot using the 0.65 NA objective. As indicated in Figure 3.7, the resulting fluorescence was collected in reflection using the same objective, passed through a beamsplitter, and directed into an optical fiber (CeramOptec, spot-to-slit fiber bundle). Emission spectra were obtained by passing light from the fiber into a 1/4 meter grating monochromoter (Acton) and onto a LN$_2$ cooled CCD camera system (Princeton Instruments). Additionally, structural and photoluminescence characterizations were performed using Fluorescence Confocal Laser Scanning Microscopy (CLSM) (Leica TCS SP2), Scanning Electron Microscopy (SEM) (AMRAY 1820), Atomic Force Microscopy (AFM) (Asylum Research MFP-3D), X-ray Diffraction (XRD) (Phillips P.W. 1830) and Energy-Dispersive X-ray Spectroscopy (EDAX). .

3.3   Result & Discussion

3.3.1   Characterization of Particles

The prepared nanoparticle solutions were characterized using DLS, UV-Vis spectroscopy and TEM. The DLS graph shows that the freshly made Ag particles were of 50nm in radius and rotovap concentrated particles were $\approx$ one micron. These numbers are complemented by TEM images which gave information about the shape of the particles. In the UV-Vis graph the flat red curve shows the aggregation effect of particles and

the black curve is the typical UV-Vis curve of 100nm Ag particles. These data suggests a tremendous aggregation effect of Ag particles when they are concentrated using rotational evaporation.
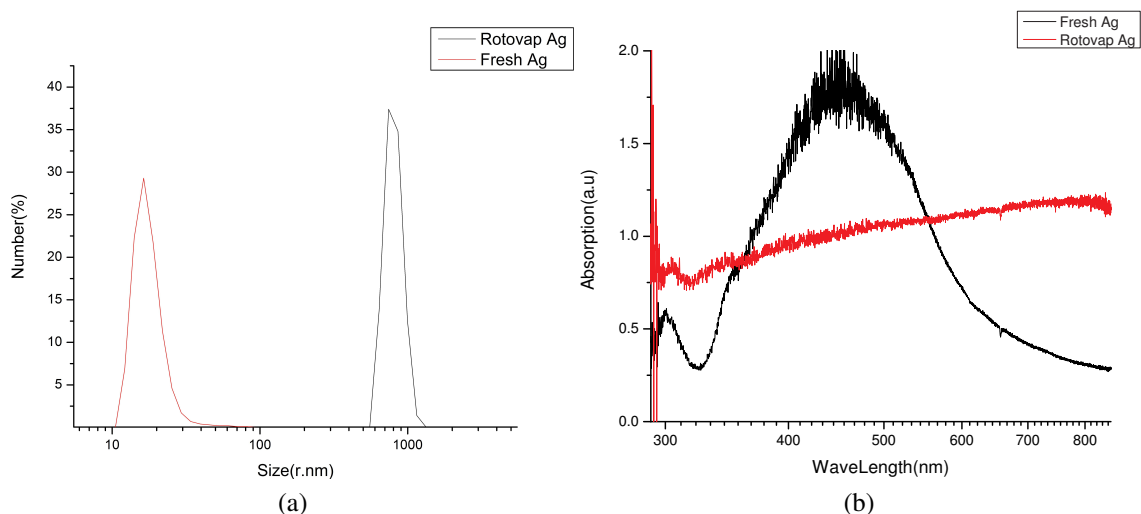
Figure 3.2. Particle characterization by DLS & UV-Vis spectroscopy. DLS size of particles (a). UV-Vis spectrum of particles (b).

The stability of the Ag nanoparticle solutions was assessed using DLVO theory (Section 2.7). The potential energy of repulsion ($V_{.R0}$, J), potential energy of attraction ($V_{.vdW}$, J) and total potential energy ($V_{.tot}$, J) between the particles were calculated using the equations of Section 2.7. The equations were solved using MATHCAD software and are shown in Appendix F. The potential energy curves for two different Hamaker constants for freshly made (non-concentrated) Ag solution are shown in Figure 3.3. The figure shows the potential energy curves as a function of distance between the particles (H1, nm). The green curve is the van der Waals force of attraction between the particles, these are long distance forces. The attraction force increases as the distance between the particles decreases but when the particles get too close then the repulsive force comes into play, which is shown as the blue curve, the sum of the attractive and repulsive forces are shown as the red curve & the total potential energy. The value of the Hamaker constant has major role in predicting the stability of the solution. $3.7 * 10^{-20}$J (Hamaker, 1937;

Huynh & Chen, 2011) is the value reported in the literature for Ag-citrate particles. To obtain a stable colloidal solution, some portion of the total potential energy curve needs to be above zero and this is usually created by use of stabilizer, which creates the energy barrier between the particles either by electrostatic or steric mechanisms. The potential energy (Figure 3.3) curves for Hamaker constant $3.7 * 10^{-20}$J indicates that the solution is not stable, contrary to physical observations. If the Hamaker constant is changed to 10^{-21}, the model predicts the solution has capability to attain stability. This indicates the value of Hamaker constant plays a vital role in predicting stability of the colloid, but it was indicated in literature that the Hamaker constant is dependent on the size of the particles (Pinchuk, 2012), which in the reported calculation have not been taken account. A similar analysis can be applied to potential energy curves of concentrated Ag solution, which are shown in Figure 3.4.
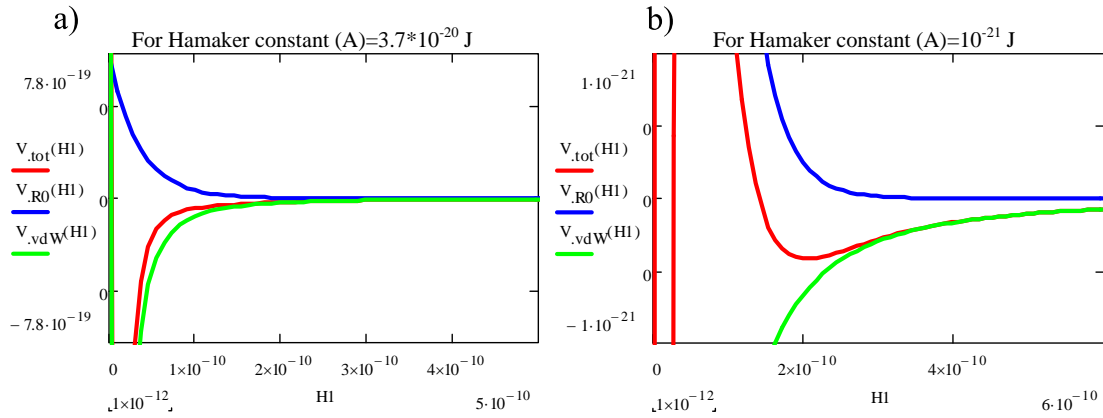
Figure 3.3. Potential energy curves for non-concentrated Ag solution.

3.3.2   Drop Casting and Exposure Data

Figure 3.6 shows a typical digital image of a $100\mu l$ drop cast film of Rotovap concentrated Ag solution. Perhaps the most interesting feature of this drop cast film is the apparent formation of an inverse coffee ring. Unlike most other films prepared by this approach, there was no apparent 'coffee ring' of high nanoparticle concentration at the
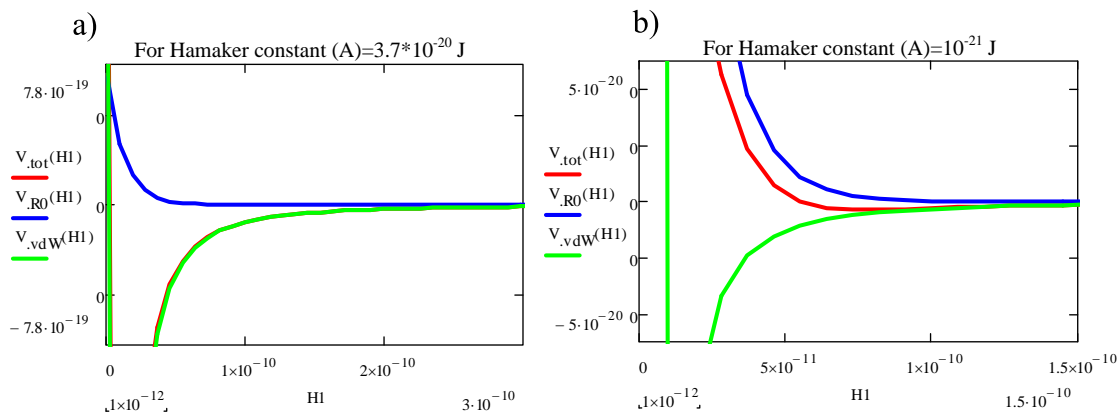
Figure 3.4. Potential energy curves for concentrated Ag solution.

(a) (b)
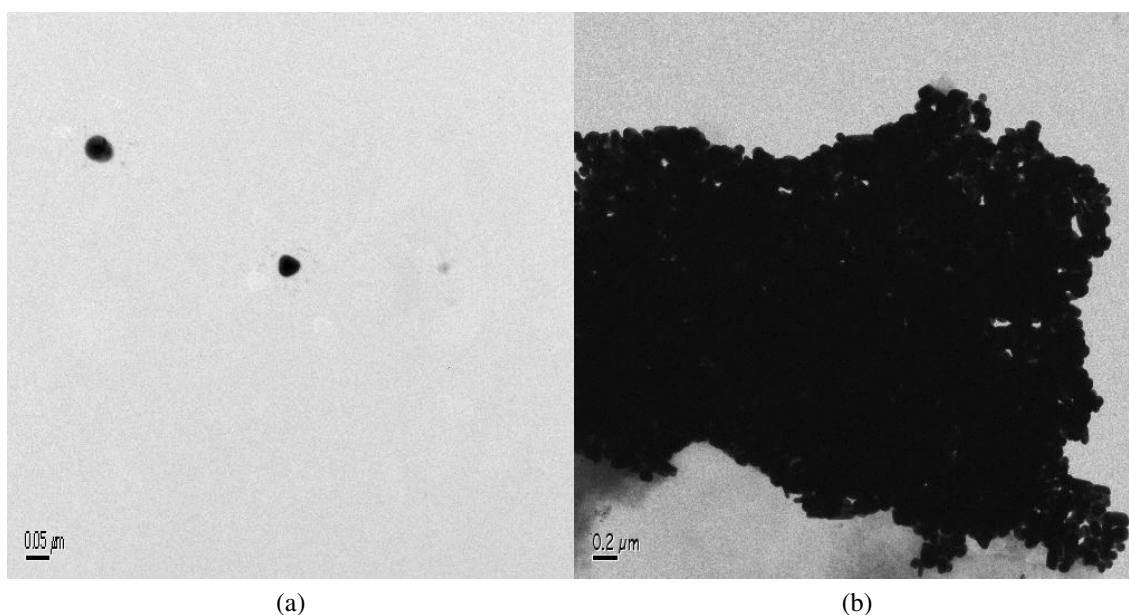
Figure 3.5. TEM images of Ag particles. TEM image of non-concentrated Ag sample (a). TEM image of rotovap-concentrated Ag sample (b).

periphery of the dried droplet. This can be understood by considering the range of the nanoparticle size distribution used here, from larger Ag nanoparticle aggregates induced during concentration, and extremely small nanocrystallites of excess citrate. During drying smaller particles are moved more readily towards the periphery of the drop where the drying rate is higher (Yunker *et al.*, 2011). The smallest particles, the excess citrate, form a coffee ring structure not visible in the digital image shown here but evident from

an FTIR measurement performed at the edge of the drop and shown in Figure 5.8. In contrast, larger particles only move slightly, as they are heavy and tend to settle down, increasing in relative abundance at the center of the droplet over time. The film was later exposed to a 532nm continous wave (CW) diode pump solid state (DPSS) laser using the optical configuration of Figure 3.7) , which has the provision to expose the film to laser excitation and to take optical images simultaneously.
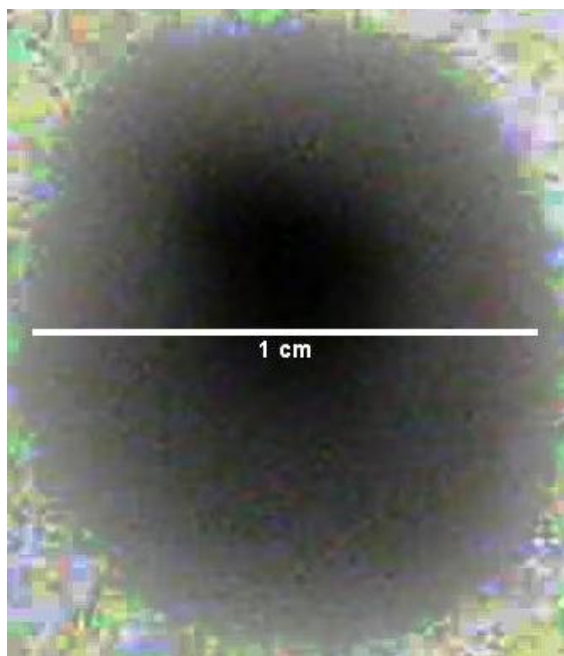
Figure 3.6. Widefield (transmission) image of Ag concentrated nanoparticle solution drop cast onto a glass coverslip.

In Figure 3.8 black and green speckle patterns are visible. The black regions correspond to Ag, where the green regions are empty space between the particles. The reason they look green is because of transmission mode imaging and camera settings. The raster patterns in the images are the regions which were exposed to the laser. It is observed that there is vacant region (bright green region) at the center of the pattern and ridges to the sides (dark regions). There was a decrease in the width of the Laser Induced Structures (LIS) when a higher numerical aperture (NA) objective was used to focus the laser beam, which is due to the ability of the higher NA objective to focus the light to a small
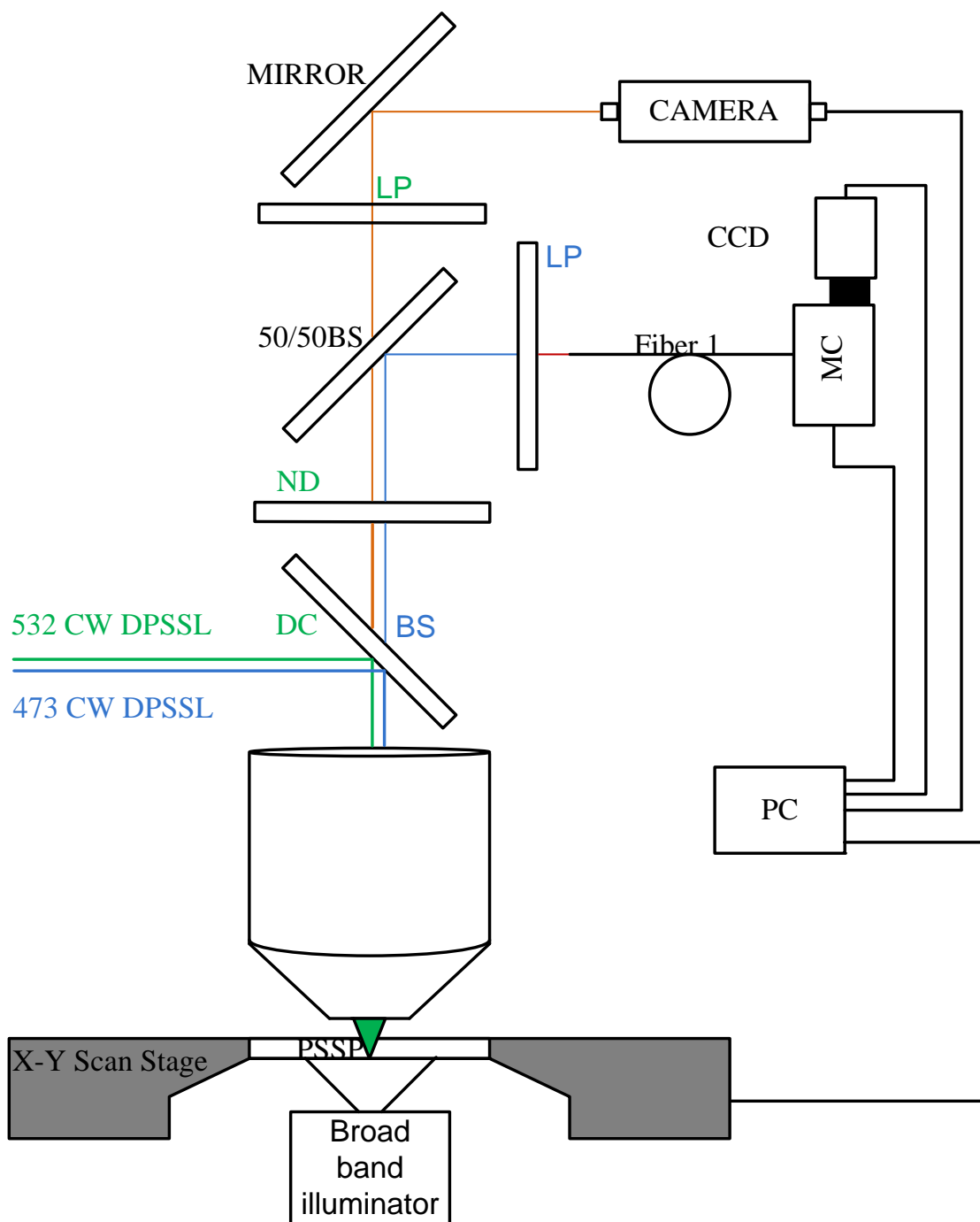
Figure 3.7. Schematic of the optical setup used for film exposure, widefield imaging and fluorescence microspectroscopy.

region. Figure 3.9a shows that the beam waist decreases and flux of the beam increases

with the increase of NA. The curves in the graph shown in Figure 3.9b were plotted using

the intensity profile of the fixed area of the raster pattern (drawn using 0.4 & 0.65 NA objectives), using ImageJ software. The width of the curves gives the inner width of the LIS and for the 0.65NA objective, the FWHM (Full Width Half Max) was found to be 1.3μm. This number is approximately 10 times better than the resolution obtained using most traditional printing techniques (Nguyen *et al.*, 2007; Kim *et al.*, 2006; Tekin *et al.*, 2008; Sirringhaus, 2000; Mizuno & Okazaki, 1991; Mikami, 1994).

| (a) | (b) |
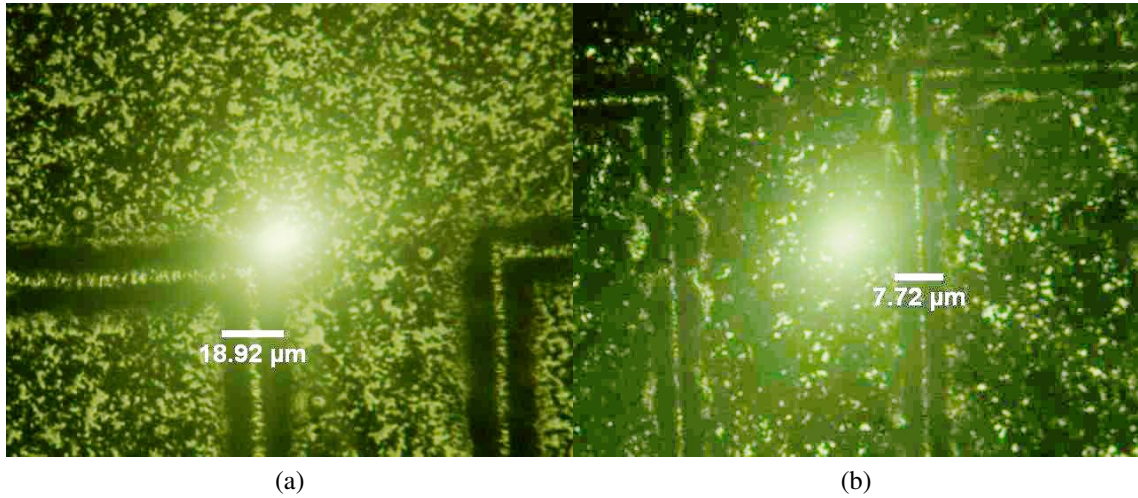
Figure 3.8. Effect of NA on size of LIS. Transmission mode optical image of laser exposed silver drop cast film, using 0.4NA Objective (a). 0.65NA Objective (b).

3.3.3 Characterization of LIS

3.3.3.1 AFM Characterization

In order to determine the exact dimensions of the LIS structures in three directions, AFM topographs were obtained of the LIS. A 'PSSP' LIS created on a concentrated Ag drop cast film on glass was chosen as the sample on which to perform AFM characterization. The LIS was characterized using AFM in non-contact mode, using a silicon tip of radius 9 +/- 2 nm. A typical AFM image (Figure 3.10) showed that the structures were 8μm high, & 25μm in width for a 0.4NA LIS and there is a cavity at the center of the
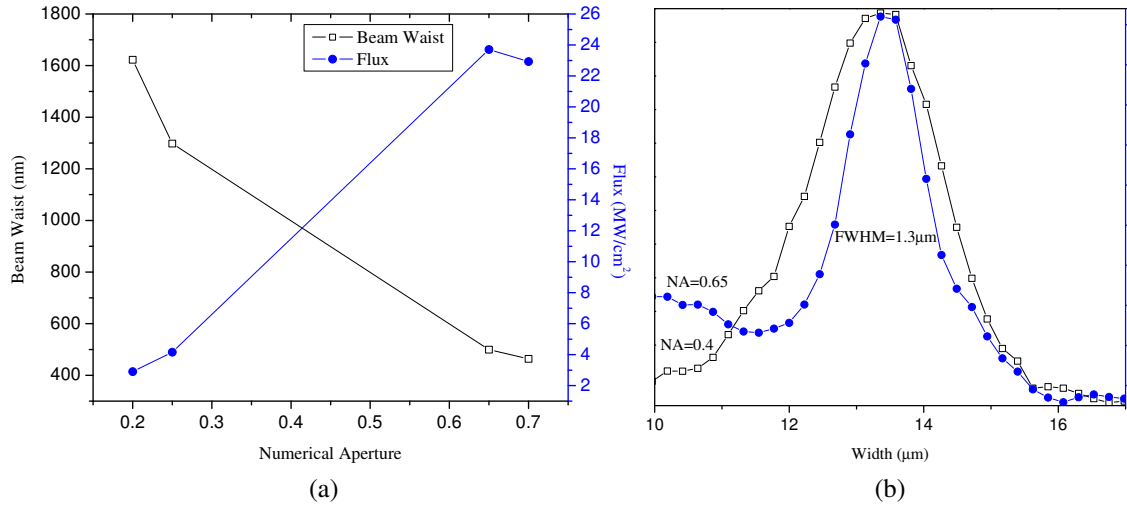
Figure 3.9. Beam waist and LIS width comparison. Beam waist, Flux Vs NA (a). LIS width comparison between 0.4 (black) & 0.65 (blue) numerical aperture objectives used during exposure (b).

structure and ridges to the sides. The AFM data confirms that there is a physical change happening as a result of laser exposure.
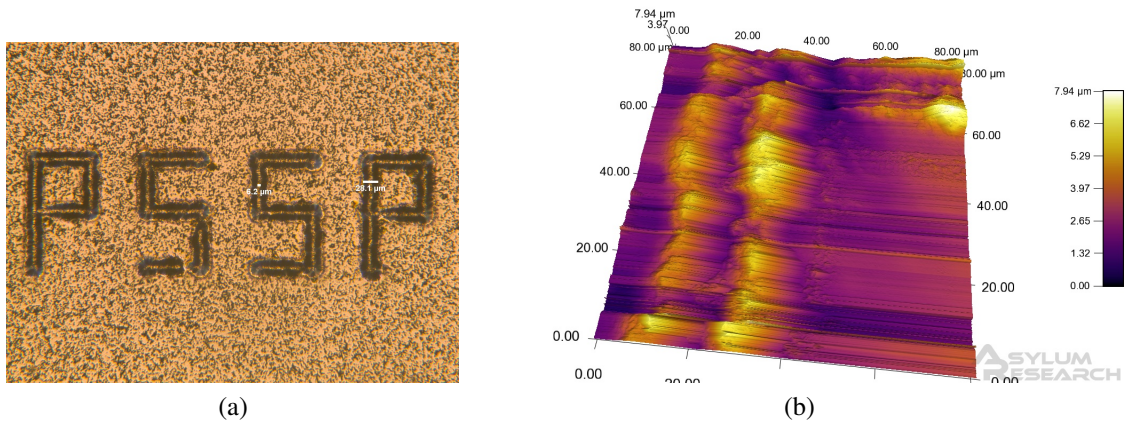
Figure 3.10. Transmission mode optical image and AFM image of LIS 'PSSP' on Ag-citrate coated glass. 'PSSP' LIS (a). AFM image of tail of letter 'P' (b).

3.3.3.2   Confocal Microscope Characterization

Irradiation of LIS with the mercury lamp in the Leica confocal microscope (TCS SP2) revealed that they were fluorescent active at the edges. Subsequently the fluores-

cence emission of the LIS was quantitatively characterized using a Leica confocal setup with various excitation wavelengths and collection optics. The 'PSSP' LIS was excited with specific wavelength lasers and the signal from the structure collected using a photo-multiplier detector. The various excitation and collection geometries are elucidated in the figure caption (Figure 3.11)

<center>(a)   (b)   (c)</center>
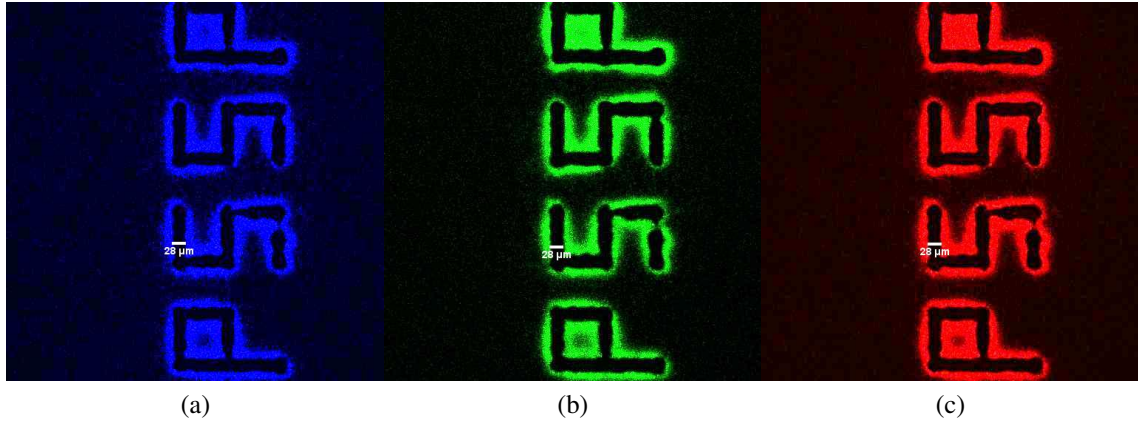
Figure 3.11. Confocal images of LIS. Excitation: 488nm, Collection: 500-530nm (a). Excitation: 543nm, Collection: 560-620nm (b). Excitation: 633nm, Collection: 633-750nm (c).

It is observed from Figure 3.11 that a strong fluorescent signal is emitted at the edges of the LIS, and that the fluorescence occurred over a broad spectral range. To further quantify the fluorescent signal, the spectrum of the fluorescent signal of LIS was taken using the setup shown in Figure 3.7, the spectra are shown in Figure 3.12.

The various curves in the Figure 3.12 are from spectra taken at various focal planes (Z-direction), relative to the LIS. The maximum signal intensity was observed at the edge of the LIS (Figure 3.12a). The intensity of the fluorescent signal is many magnitudes lower on the surface of the LIS, relative to the signal collected at the edge of the LIS (Figure 3.12b). These spectrums (Figure 3.12) also quantifies the broad range of fluorescent signal observed in the confocal laser scanning microscope images of Figure 3.11. To gain
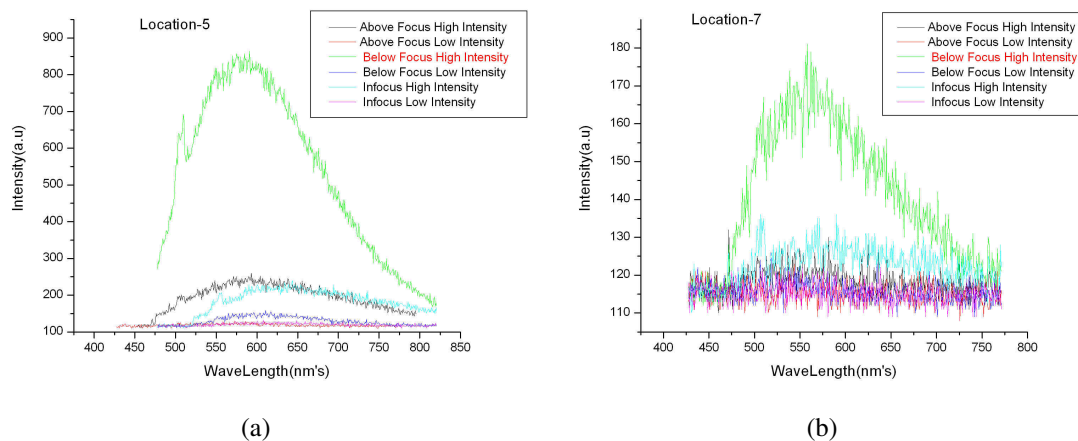
Figure 3.12. Fluorescent spectrum comparison of the LIS at different vertical positions (Z-axis). At the edge of the LIS (a). On the surface of LIS (b).

further insight into the fluorescent nature of the LIS, XRD was performed to investigate the identity of the fluorophore.

3.3.3.3   X-ray Diffraction and SEM Characterization

Laser exposed and unexposed regions of Ag nanoparticle films were characterized with XRD to determine any crystallographic differences between these two regions. The crystal structure of the silver film was identified by XRD using nickel-filtered Cu K-α radiation. Diffraction patterns were recorded over a range of 2θ angles from 20 to 75. The red curve in Figure 3.13a is from an unexposed region of a Ag film, & contains three characteristic peaks of crystalline (fcc) Ag. The black curve of Figure 3.13a is from a laser exposed region; additional peaks are observed. These peaks, identified using a difference spectrum of Figure 3.13a (blue), exhibit good qualitative agreement with the known peak positions for sodium carbonate (green delta functions), which is a proposed byproduct of thermal decomposition of sodium citrate (Barbooti & Al-Sammerrai, 1986; Guarini & Dei, 1995; Bielawski & Baranowska, 1985; Garcia-Guinea *et al.*, 2011).

Finally, electron microscopy was used to elucidate the origin of the material comprising the apparent ridges bracketing the LIS, and the possible source of the observed fluorescence. Samples were prepared for SEM imaging by sputter coating (Cressington 108 auto) with a 21 nm thick layer of AuPd alloy, insignificant in height with respect to the micrometer sized features present. A typical SEM image of a section of a LIS is shown in Figure 3.13b. Immediately prominent in the image are the series of periodically spaced holes, likely caused by the focused incident laser beam during scanning. Here the discontinuous movement of the 2-phase stepper motor used to drive the translation stage is apparent (scan rate=0.07 mm/sec). While the volume of these holes cannot be determined quantitatively from the SEM image, their presence does indicate a source for the material found in the ridges of the LIS (Figure 3.10)), which could not be accounted for by AFM. In this case the depth (> 5 μm) of the holes could not be determined accurately by AFM as the width of the pyramidal AFM was likely greater than the size of the holes ($\approx 5\mu$m). Also visible in the SEM images are microcrystallites on either side of the LIS. These crystallites appear to form abruptly along the topographic edge of the LIS, as visible in the SEM, and gradually decrease in size and abundance moving away from the LIS. This same 'intensity' profile can be seen in the fluorescence images. The features present in the fluorescence images (Figure 3.11), are not spatially correlated with the LIS, but rather this pattern of microcrystallites.

3.4   Summary

This chapter has presented preliminary evidence for a relatively simple method whereby micron sized line features can be generated using low power focused CW laser illumination of silver nanoparticle based thin films. The resulting Light Induced Structures (LIS) exhibit 3D topography and are $\approx$ 10X times smaller than those achieved by typical printing techniques. Optical characterization of the LIS showed that in addition to changes in
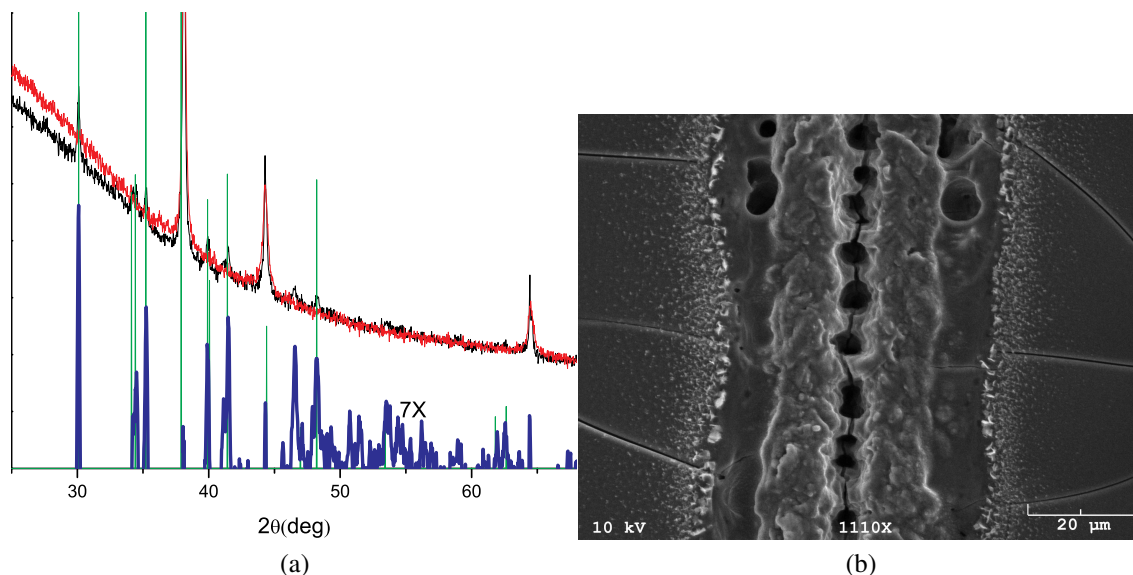
Figure 3.13. XRD and SEM of LIS. X-ray diffraction spectra comparing of unexposed (red curve) and exposed regions within a Ag nanoparticle film (black curve) (a). Scanning electron micrograph of LIS (b).

morphology, they emit strong broad visible fluorescence emanating from the edges of the features. Crystallographic characterization of LIS (XRD) showed that the films undergo a chemical change during exposure (likely the thermal decomposition of sodium citrate into sodium carbonate). The presence of newly formed microcrystallites visible on either side of the LIS in the SEM images suggests that the observed fluorescence may be from the microcrystallites. Further experiments were carried out to investigate the mechanism of LIS formation, their fluorescence nature and are discussed in Chapters 5 & 6 of the thesis.

Chapter 4
LASER INDUCED STRUCTURES ON SILVER-POLYMER COATING

4.1 Introduction

This chapter builds on the previous chapter by investigating the effect of increasing the complexity of the film formulation, with the goal of accessing additional properties. Specifically a certain amount of non-conducting polymer, polyvinyl alcohol (PVOH), was investigated, PVOH polymer was added to the concentrated 20nm diameter Ag nanoparticle solution. This chapter reports the optimum Ag to polymer ratio required to achieve a coating formulation for producing LIS with a minimum laser power. In this technique, a silver-PVOH based coating formulation is applied on the substrate, air dried and then subjected to focused laser light of a particular wavelength and power to generate a LIS in the dried coated film. The details of feature formation were discussed in Chapters 2 & 3.

The intention behind adding PVOH was to add strength, flexibility and durability to the coating, and to create non-conducting area. Here it was postulated that the laser exposure may sinter the Ag particles, and form a conductive path along the laser exposure line feature. PVOH was selected because it dissolves in water, has a molecular weight providing higher viscosity and is largely transparent to visible light. The combination of Ag & PVOH yields a coating formulation that is completely aqueous based, obviating the need for toxic solvents or environmentally hazardous polymer. The ratios of Ag to PVOH studied in this chapter were in the range of 0.002 to 0.013, extremely low compared to other conducting formulations (Huang *et al.*, 2006).

4.2   Materials and Method

4.2.1   Synthesis of 20nm Diameter Ag Nanoparticles

The chemicals used for the synthesis were silver nitrate and sodium borohydride. Both the chemicals were analytical grade, purchased from Sigma-Aldrich (USA) and used without further purification.

Aqueous solutions of 1mM of $AgNO_3$ and separately 2mM of $NaHB_4$ in $18.2M\Omega.cm$ pure water were prepared. 30ml of the $NaHB_4$ solution was transfered into a 100ml conical flask containing a stir bar, rotating at 300rpm. This solution was cooled in an ice bath for 20 minutes. The reaction proceeded by titrating with 10ml of $AgNO_3$ solution (at a rate of 1 drop per second) using a 50ml burette. Stirring was stopped immediately after titration. The resulting yellow colored Ag solution was stored in glass vials for further characterization and for making coating formulations. This synthesis procedure is based on the work of Solomon *et al.* (2007)

4.2.2   Ag Nanoparticles-PVOH Based Coating Formulation and Coating Setup

The Ag particle solution of Section 4.2.1 was concentrated using constant heat at $80°C$ and stirring to remove excess water. Three different volumes of Ag solution (200, 120, 40ml) were concentrated to 4ml volume each. The resulting nanoparticle solutions were characterized using DLS, UV-Vis Spectroscopy, and TEM imaging and were compared with the fresh solution (non-concentrated). After characterizing the solutions, the concentrated Ag solutions were mixed with different amounts of PVOH polymer solution to get different Ag to polymer ratios and then there solutions were coated using metered draw down coating with three different rod numbers. An in use of the draw down instrument, and the rods, is shown in Figure 4.1. The rods used for metered draw down coating consisted of steel rods with spiral wound wire over the surface of the rod. The distance between the threads of the spiral wound wire and the thickness of the wire dictates the

coating thickness. The rod numbers and their corresponding wet coated film thicknesses are shown in Table 4.1. Higher rod number have larger space between the threads and the spiral wound wire is also thicker.

(a)   (b)
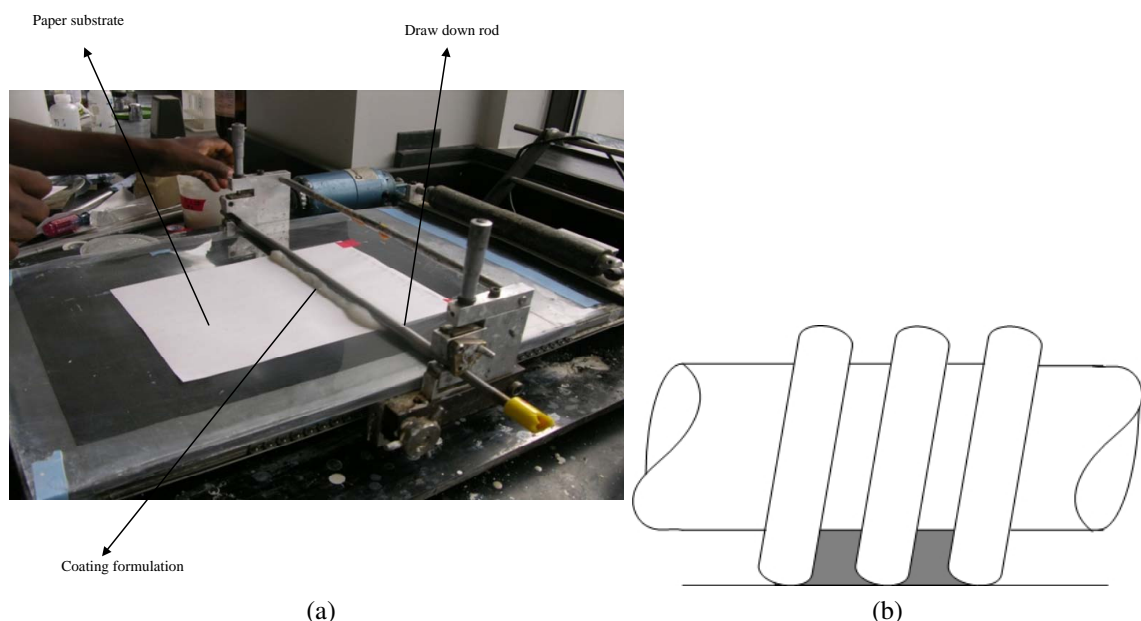
Figure 4.1. Meter bar coating setup and spiral wound rod. Meter bar coating setup (a). Spiral wound rod (b).

Rod Number	Wet Film Thickness (μm)	Wire Diameter (mm)
1 (Yellow)	6	0.08
5 (Horn)	50	0.64
8 (Blue)	100	1.27

Table 4.1. Rod number and corresponding film thickness.

The 20nm Ag-polymer based coating formulation was coated on HP-gloss paper substrates and then air dried for 4 hours, 22x22mms areas of uniformly coated sections were cut from the samples for laser exposure. Dried coated samples are shown in Figure 4.2. The detailed procedure of coating and cutting out uniformly coated sample areas is given in Appendix D. The exact coat weight was not measured by the gravimetric technique

due to the very small area of uniform coating and variations resulting from the cutting of the samples. The same coating setup was used to coat glycerol on the same size and type of substrate. The resultant coat weight was determined using the gravimetric technique. These values were used to back calculate the approximate coat weight of the Ag-polymer based coating.

Rod Number	Glycerol coat weight (g/m^2)
1 (Yellow)	15.9133
5 (Horn)	40.8637
8 (Blue)	65.5134

Table 4.2. Rod number and corresponding glycerol coat weight on HP-gloss paper.

4.3   Result and Discussion

4.3.1   Characterization of Particles

Nanoparticle solutions were characterized using DLS, UV-Vis spectroscopy and TEM imaging. DLS revealed that the freshly made Ag particles were a 15 to 20nm in diameter, where concentrated particle solution showed aggregation effects. This aggregation effect was pronounced when the volume of the solution to be concentrated increased from 40ml to 200ml. These trends of DLS curves are complemented by UV-Vis curves, shown in Figure 4.3.

A TEM image of freshly made 20nm diameter Ag particles is shown in Figure 4.4.

4.3.2   Exposing and LIS Characterization

A 22x22mm piece of uniformly coated sample was adhered to a glass slide using double sided tape, so that the coated sample was flat for subsequent laser exposure. Each sample was exposed to 532nm CW DPSS irradiation, using the setup shown in Figure
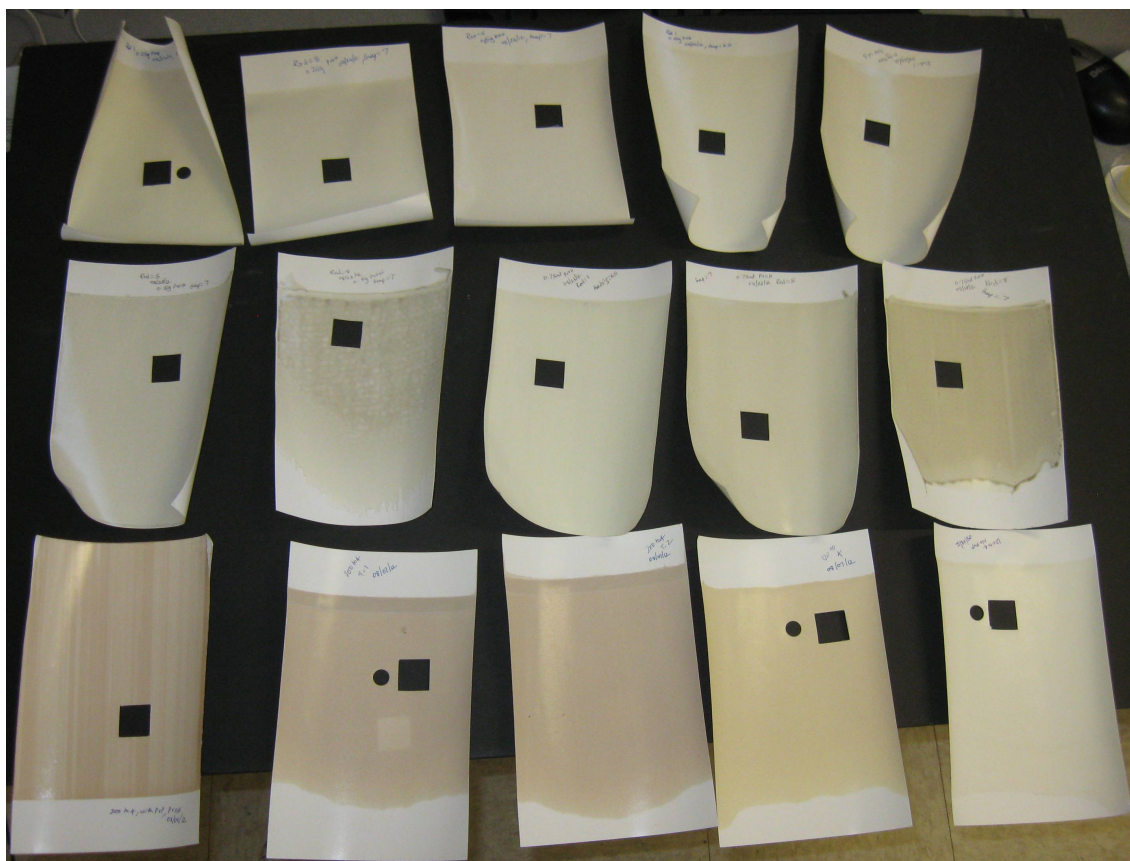
Figure 4.2. Ag-Polymer based coating on HP-gloss paper substrates using different rod numbers.
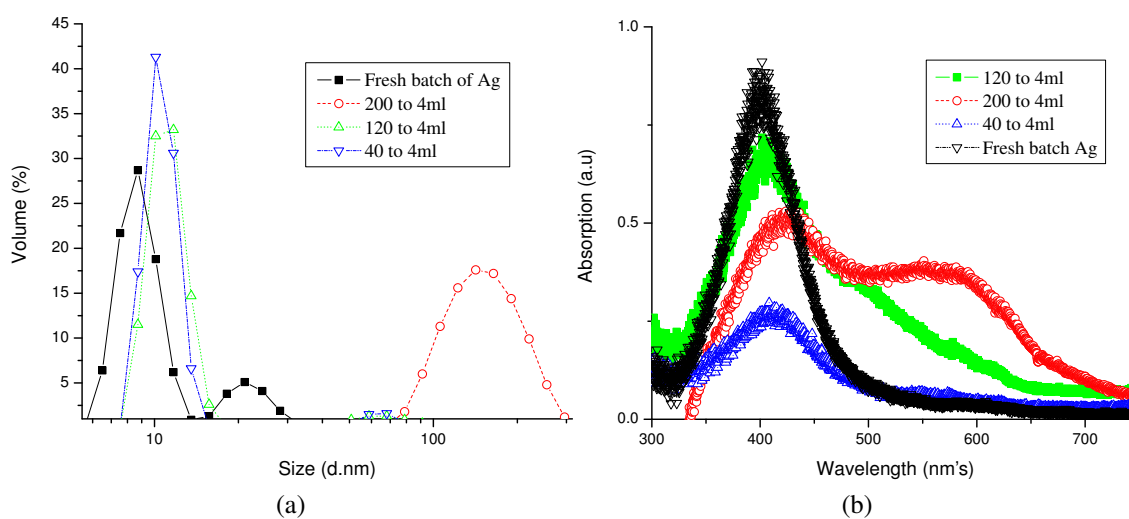
Figure 4.3. Comparison of DLS, UV-Vis spectrum of freshly made to concentrated Ag solution. DLS (a). UV-Vis spectrum (b).
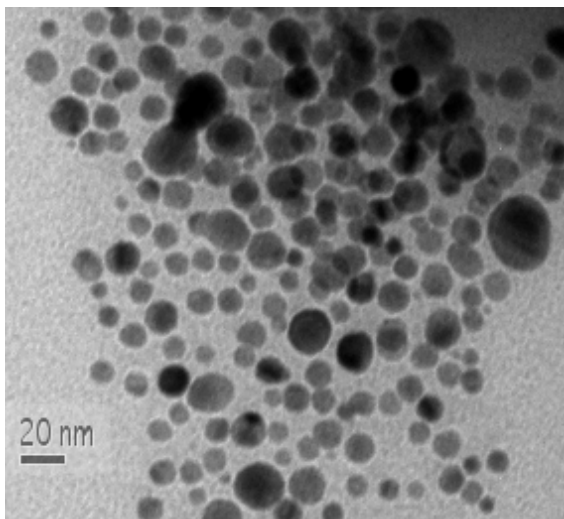
Figure 4.4. TEM micrograph of 20nm Ag particles.

3.7. The laser power used was measured after the objective (0.65 NA) using a standard laser power meter (THROLABS PM100D). The scan speed used for exposing the coated HP gloss substrates was $2\mu m/sec$. The substrates were translated under the laser using the scan stage and were constantly observed; as soon as a laser feature was observed, an image of the LIS was taken using a 5.1MP (Mega pixel) microscope eyepiece camera (Amscope MU500). To quantify the physical dimensions of the laser feature, non-contact mode AFM was performed.

As can be seen from the AFM data (Figure 4.5) the LIS were approximately 15μm wide and just $\approx$ 136nm high, whereas Ag-citrate based coating gave 8μm high LIS (Figure 3.10b). To find the optimum ratio of Ag to PVOH in coating formulations to induce LIS formation at a minimum laser power, various ratios (Ag to PVOH) of coating formulations were tested, the results are tabulated in Table 4.3. The 'Response' column of Table 4.3 corresponds to the observed LIS, which was recorded using the microscope eyepiece camera (5.1MP Aptina MU500) as optical images (Figure 3.7). The maximum power of the laser available was 19.3mW, for all the samples different power levels were tried and the lowest power at which the LIS was observed is reported in the 'Critical Power' column. The tabulated values indicate a critical Ag-PVOH ratio required to in-
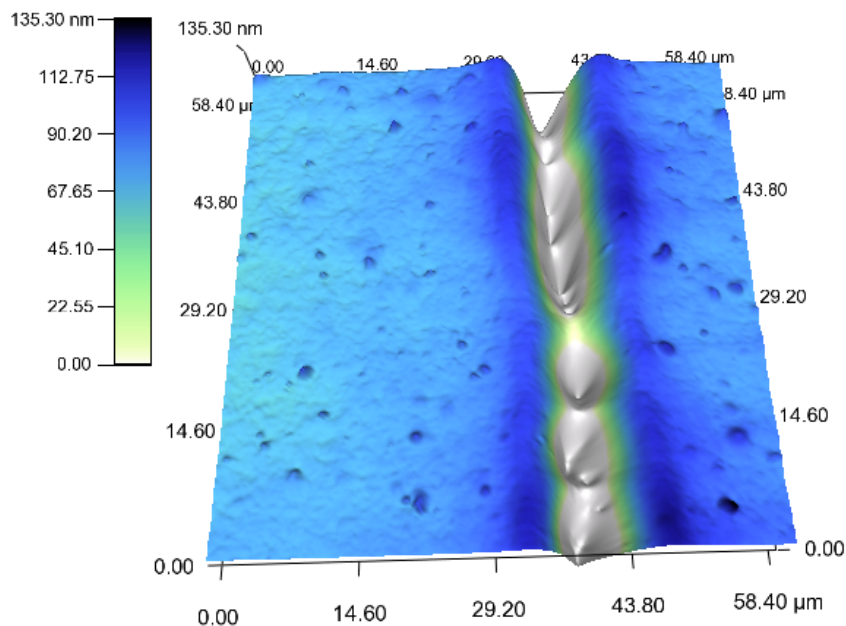
Figure 4.5. AFM image of LIS on Ag-Polymer coated paper sample.

duce a response with a particular wavelength and laser power. It is noted that the power numbers can be improved by moving towards the wavelength where the Ag nanoparticles absorbs maximum. For example, for 20nm Ag particles, based on UV-Vis absorption curves (Figure 4.3b), a wavelength of 400nm laser should give a response at the lower laser power. This is not just because of higher photon energy (lower wavelength) but also because of higher absorption of 20nm Ag nanoparticles at that wavelength. In the optical characterization, laser scanning confocal microscope (LSCLM) was used to examine the fluorescence nature of LIS. In LSCM characterization, various laser wavelength (488nm, 543nm, 633nm) was used to excite the LIS & emission light was collected using photo multiplier tube (PMT). Interestingly, LSCLM characterization did not show any fluorescence nature of the LIS.

A possible reason for the non-observation of LIS formation with large amount of polymer ($21.242 g/m^2$ and above) is that the Ag particles might be embedded in the polymer

Ag (g/m^2)	PVOH (g/m^2)	Ratio (Ag/Polymer)	Critical Power (mW)	Response
0.053	26.328	0.002023	19.3	No
0.048	23.801	0.002023	19.3	No
0.043	21.242	0.002023	19.3	No
0.055	17.113	0.003236	19.3	Yes (Strong)
0.05	15.47	0.003236	19.3	Yes (Weak)
0.045	13.807	0.003236	19.3	Yes (Weak)
0.056	13.053	0.004315	14.3	Yes (Strong)
0.051	11.799	0.004315	14.3	No
0.045	10.531	0.004315	14.3	No
0.057	8.852	0.006472	14.3	Yes (Weak)
0.052	8.002	0.006472	14.3	No
0.046	7.142	0.006472	14.3	No
0.058	4.503	0.013	14.3	No
0.053	4.071	0.013	14.3	No
0.047	3.633	0.013	14.3	No

Table 4.3. Different Ag to polymer ratio in coating and corresponding laser response.

(also make the surface go out of focus) which may lead to a decrease in the amount of laser energy reaching to the settled Ag particles in the coating. The photon energy which is converted to heat by Ag particles may not be sufficient to decompose the surrounding polymer matrix, consequently heat is lost through conduction into the coating.

A potential reason for non-LIS response with too little polymer ($8.022 g/m^2$ and below) is that the majority of the polymer and particles might be used up to smoothen the surface of the hp-gloss paper i.e. they will be embedded between the fibers/fillers such that the heat generated by the particles was not sufficient to effect the fibers/fillers & induce a change. Control samples of concentrated Ag solution, and separately prepared PVOH solutions, were coated on two separate sheets of HP-gloss paper and exposed to different levels of laser power. There was no LIS response observed with either sample.

To predict the surface temperature of the Ag particles during laser absorption, a simple quasi-steady state energy balance was performed across the volume of the particle. The specific details of all the equations used for temperature estimation are given in the
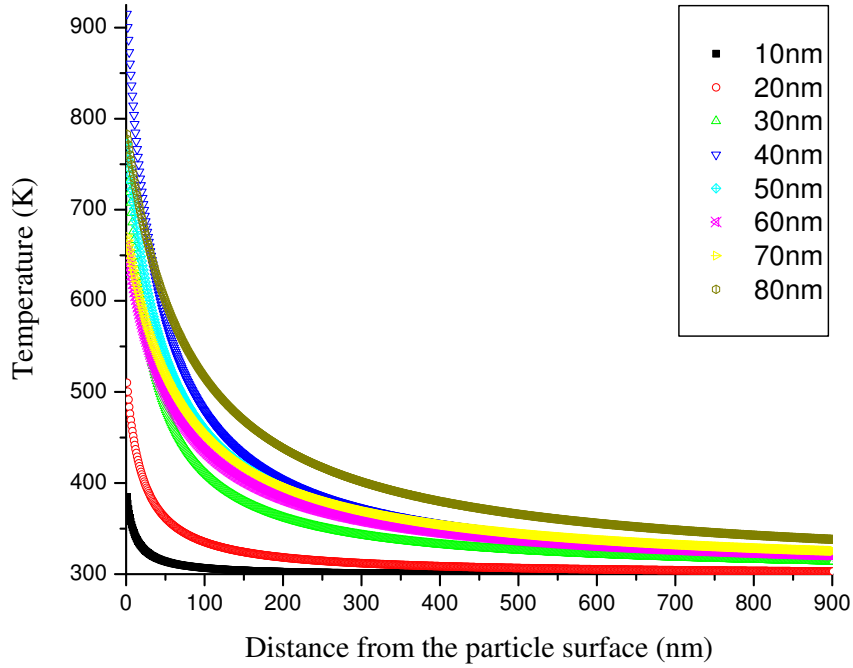
Figure 4.6. Temperature profile around different size Ag particle embedded in PVOH matrix.

Section2.8.

$$\rho_0 c_0 V_0 \frac{dT_0}{dt} = \frac{1}{4} I_0(t) Q_{abs} S_0 - J_\varepsilon S_0 \tag{4.1}$$

MATHCAD software was used to obtain values from the energy equations and an example for the surface temperature; and the temperature profile estimation around a 50nm Ag particle is given in Appendix E. Figure 4.6 shows the temperature distribution around different sized Ag particles embedded in a PVOH matrix.

4.4 Summary

This chapter reports a new coating formulation based on 20nm diameter Ag nanoparticles and PVOH polymer. It was determined experimentally that below a laser power of 14.3mW, no structures were formed. The minimum size of the structure achieved was 15μm wide. Interestingly, the LIS based on Ag-polymer coating were not fluorescent active, this is described in greater detail in the following chapter.

Chapter 5

MECHANISM OF LIS AND REASONS BEHIND EDGES OF THE LIS BEING

FLUORESCENT

In the previous chapters, particular parameters and coatings that respond to laser illumination to produce LIS were characterized. In general, the response is expected to be a result of optically induced heating of the nanoparticle. This heat, in turn, causes chemical and physical changes in the material layer (nanoparticles and its surrounding layer). However, a detailed understanding of the basic mechanisms behind this change is missing. The work in the present chapter is aimed at understanding the mechanisms that drive the structure formation and the cause for the observed fluorescence in particular situations.

5.1   Mechanism of LIS Formation

In order to frame analysis of the mechanism of LIS, a cartoon of the entire system of interest is shown in Figure 5.1. The system, a Ag nanoparticle based film, consists of Ag particles surrounded by sodium citrate (Chapter 3) or polymer (PVOH, Chapter 4). Based on the coating formulation used to make the film for LIS formation, the amount of citrate/polymer by weight was ≈ 8 times the amount of reduced Ag. The nanoparticle film coating can be visualized as shown in Figure 5.1, where an individual Ag particle is surrounded by either citrate or polymer. When the laser (532nm) is directed towards this film, Ag absorbs a portion of the radiation (citrate/polymer has poor absorption at 532nm) and because of the efficient photothermal transfer of metal particles (Section 2.3), the absorbed radiation is converted into heat.

The heat generated by absorption is conducted in all directions around the metal particle, but because of the tremendous discontinuity in thermal conductivity at the interface

of the particle (Ag (k=429W/m-K)) and capping material (PVOH (k=0.2W/m-K)), heat accumulates at the interface. The resulting temperatures (Melting point of bulk Ag is 961.78°C and melting point of sodium citrate dihydrate is 150°C) can easily exceed the decomposing temperature of the material (sodium citrate dihydrate or PVOH). An important point to note here is that the entire process of heat absorption, conversion, and conduction happens in few picoseconds (Hodak *et al.*, 1998).
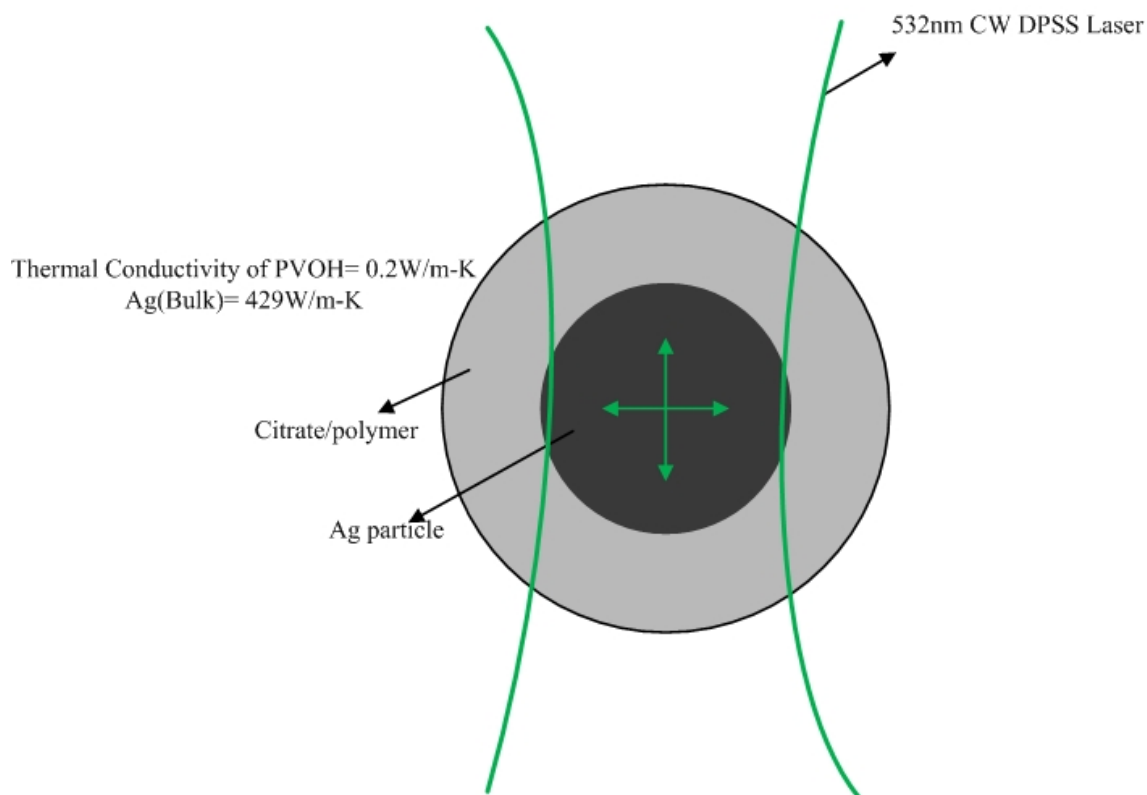
Figure 5.1. Cartoon depicting laser beam-Ag nanoparticle interaction.

The use of a laser along with a high NA objective gives rise to high flux at the point of focus. This high flux spot raises the temperature at the particle-surrounding material interface, leading to the formation of a melt pool of citrate or PVOH and fast escaping volatile material (degradation products of the citrate or polymer, such as carbon dioxide, water vapor). This pressure of the hot expanding vapor pushes the melted pool material towards the sides of the focus spot. This hypothesized mechanism for LIS formation is explained

in detail in the literature review chapter (Chapter 2). Experimentally it was found to be difficult to quantify the physical and chemical changes occurring during nanoparticle film irradiation and LIS formation. The reasons were: 1) The laser intensity required was too high and it was not possible to cut the laser intensity with the available filters to collect Raman signals, and 2) The fluorescent nature of the LIS also adulterated the Raman signal. Consequently LIS were analyzed post formation and observations were made related to that might have happened during the formation process. TGA (Thermo Gravimetric Analysis) along with MS (Mass spectroscopy) were used to quantify the weight loss and nature of the volatile material, respectively. In addition, another set of films and LIS were made from different centrifuged cuts of Ag solution (Ag synthesis explained in Chapter 3), to support the hypothesis of requiring low decomposing material around the Ag particle to get response.

5.1.1 Films of Centrifuged Ag Solution & Their Laser Response

Ag solution was centrifuged (12000g) for half an hour. The centrifugation lead to the separation into a bottom layer and a top layer. As expected the bottom layer had a high Ag content while the top layer contained little Ag and the particles present were of small size confirmed based on color of the solution. In addition the top layer contained the major portion of sodium citrate molecules in the solution. $100\mu l$ of the bottom solution cut was drop cast onto a glass slide, and allowed to air dry for 8 hours. The top layer of centrifuged Ag solution was concentrated to remove excess water using rotational evaporation, $100\mu l$ of this solution was drop cast onto a glass slide and allowed to air dry for 8 hours. The air dried samples were then subjected to focused 532nm CW DPSS (Diode pumped solid state) laser irradiation using the optical setup shown in Figure 3.7.

The dropcast film formed from the bottom Ag solution did not show any response when exposed to the laser (Figure 5.2a). Figure 5.2 may be interpreted as the black speckle patterns arising from Ag nanoparticles and the bright regions as surrounding to
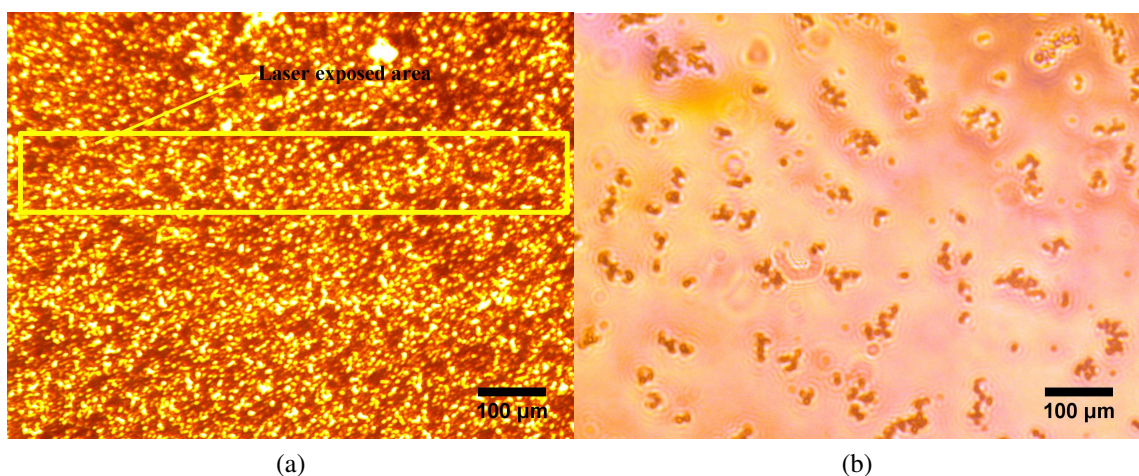
Figure 5.2. Laser interaction with centrifuge Ag film. Drop cast film of bottom cut of centrifuged Ag solution (a). Drop cast film of diluted solution of bottom cut of centrifuged Ag solution (b).

the space between them, consisting of sodium citrate. The investigation of image of Figure 5.2a reveals the possibility that particles may in fact be in contact and thereby path for heat conduction (which would obviate the structure formation). Consequently, the bottom solution was diluted to ensure that the film cast from this solution did not contain particles in contact. This diluted bottom Ag solution was drop cast onto a glass slide and air dried before being subjected to laser irradiation. The diluted dropcast film did not show any response to the laser exposure (Figure 5.2b). Conversely, the drop cast film cast using the rotovap concentrated solution of the top cut showed a response to laser exposure, see the boxed region of Figure 5.3. Taken together their response suggest that in order for LIS formation to occur there needs to be a low decomposition temperature material surrounding the Ag particles, in this case sodium citrate dihydrate. To confirm this theory of LIS formation by pressure created by volatile material such as water vapor and citrate or polymer degradation products, TGA of the sodium citrate and dried Ag-citrate nanoparticle film material, along with mass spectroscopy of the gases evolved during the TGA process was performed.
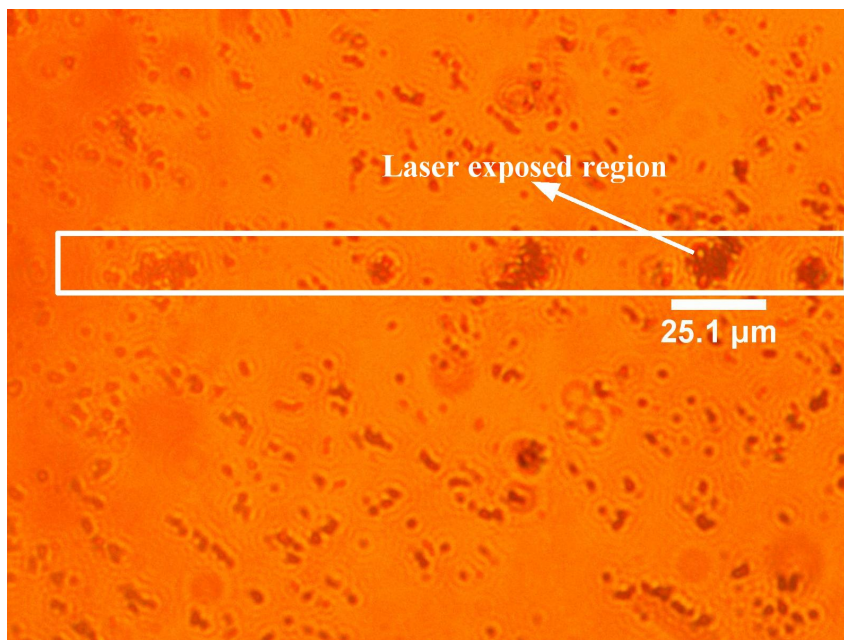
Figure 5.3. Laser exposed film of top cut of centrifuged Ag solution.

5.1.2 TGA and Mass Spectroscopy Analysis

Thermogravimetric analysis of sodium citrate (has melting point 313°C) and dried silver nanoparticles (Section 3.2.1) was performed in the presence of air (N_2=78%, O_2=21%), to simulate LIS formation in native atmospheric conditions. The temperature in the TGA furnace (TA Instrument, TGA-Q500) was raised at a ramp rate of 10°C per minute from ambient temperature up to 1000°C. Samples were held at 1000°C for 20 minutes before cooled down at a rate of 10°C per minute. Mass spectroscopy (AMETEK, Dycor Benchtop) was performed simultaneously on the gases released from the TGA exhaust. The mass-spectrometer was scanned at a rate of a scan per 30 seconds. The exhaust pipeline of the TGA to mass-spectrometer was held at 120°C using a heating coil, to avoid water vapor condensation in the exhaust line.

In both the Figure 5.4a & Figure 5.5a (TGA curves), the black curve represents the weight loss of the compound as a function of temperature, while the blue curve is the derivative weight loss with respect to the temperature of the chemical compound. The mass spectrographs of Figure 5.4b & Figure 5.5b represent the gases evolved during the

71
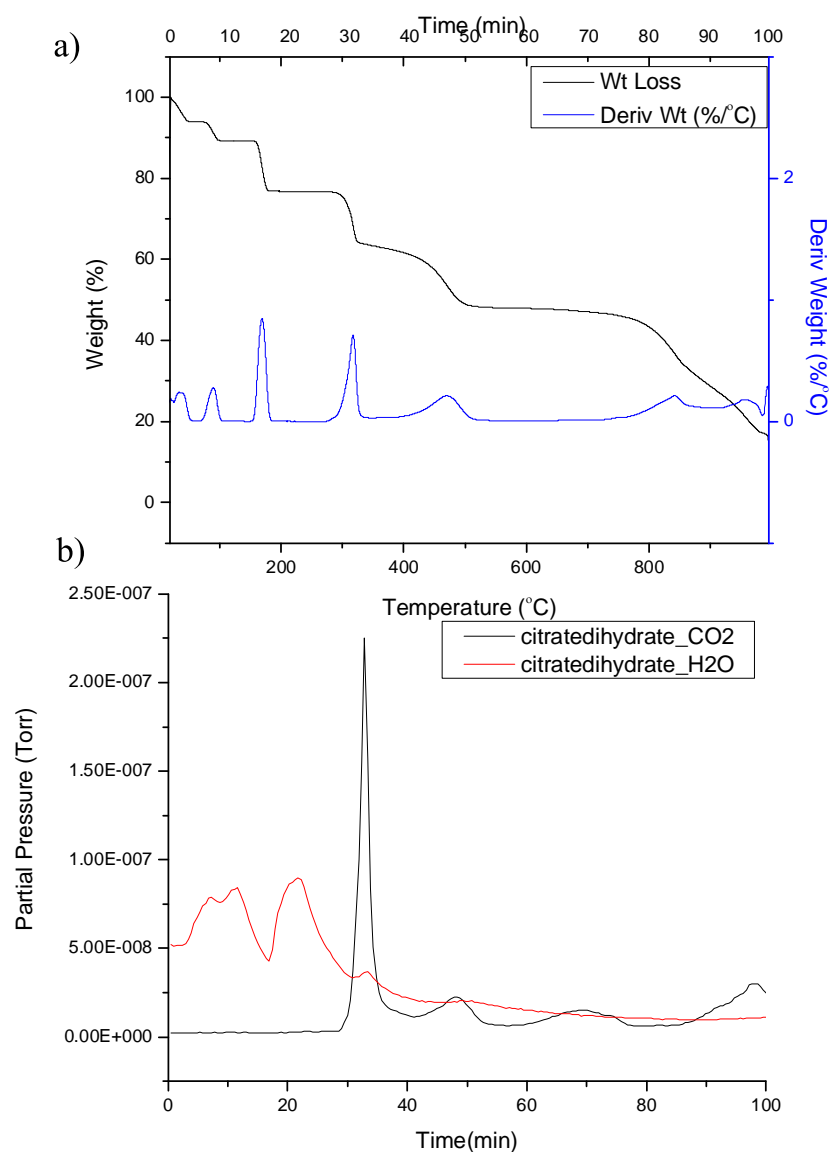
Figure 5.4. TGA, Mass-spectroscopy of sodium citrate dihydrate. TGA of sodium citrate dihydrate (a). Mass-spectroscopy of gases evolved from TGA of sodium citrate dihydrate (b).

TGA analysis and are presented as the partial pressure of the gas evolved during the TGA process versus their arrival time at the detector of mass spectrometer. The red curve represents the water released during TGA of the compounds (sodium citrate dihydrate (Figure 5.4), dried Ag (Figure 5.5)), while the black curve (Figure 5.4b) represents CO_2 evolved during TGA of the compounds . The MS peaks corresponds well with the temperature at

72
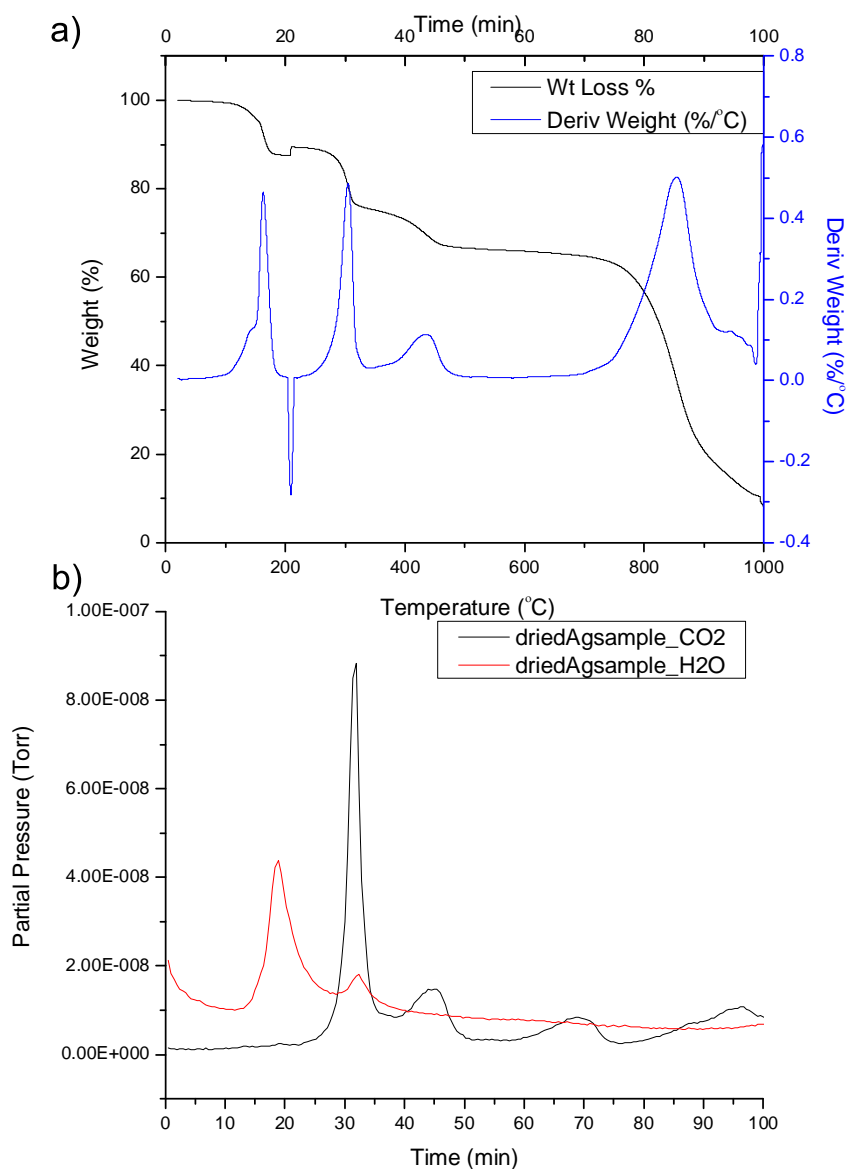
Figure 5.5. TGA, Mass-spectrograph of dried Ag-citrate. TGA of dried Ag nanoparticles (sodium citrate based) (a). Mass-spectroscopy of gases evolved from TGA of dried Ag nanoparticles (b).

which weight loss occurred in the TGA curves. These results are consistent with the notion that the material surrounding the nanoparticles decomposes and releases vapor upon exposure to heat.

To validate the theory of LIS formation due to vaporization of low temperature decomposing material surrounding the particle, another material with low decomposition

temperature was employed to surround the nanoparticles. Specifically Polyvinyl alcohol (PVOH) (has a melting point of 230°C) was used as the continuous matrix material; the details of LIS formation on Ag-PVOH formulations are described in Chapter 4. TGA-MS data of PVOH is presented in Figure 5.6.
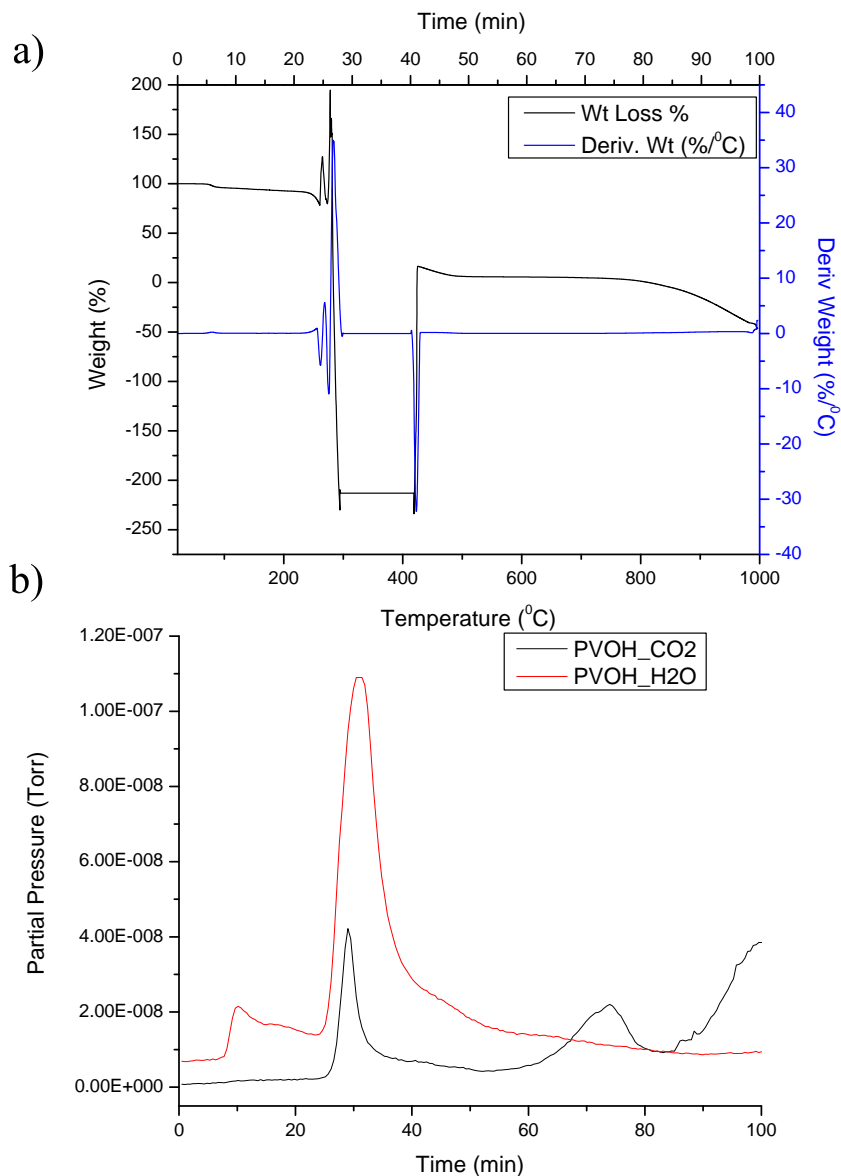
Figure 5.6. TGA, Mass-spectroscopy of PVOH. TGA of PVOH (a). Mass-spectroscopy of gases evolved from TGA of PVOH (b).

The TGA-MS data of PVOH (Figure 5.6) suggests that the majority of the weight loss is from water. The color notation for the curves in the graphs of Figure 5.6 are comparable to those of Figure 5.5. The TGA data for PVOH shows a negative weight loss, which is not physically possible and is attributed to the issues related to the TGA furnace. A number of repeats were performed but the result was the same and after few days it came to be known that the furnace died because the inner glass lining was shattered. TGA data of PVOH from the literature (Strawhecker & Manias, 2000) confirms the decomposition of PVOH starts at approximately 200°C and is completed just below 450°C. Therefore it is hypothesized that during LIS formation, flash evaporation of water occurs to prove degradation of the polymer itself. These hot vapors, while expanding, push the melted pool of compounds to the side as the laser moves along the prescribed path.

5.2   Mechanism Behind Observed Fluorescence

5.2.1   Reasons behind just the LIS edges being fluorescent

As described in Section 3.3.4, LIS formation on Ag-citrate based coating results in fluorescent active edges not the structure, shown in Figure 3.11. The possible mechanism behind the observed fluorescence was subsequently investigated. The fluorescence spectrum of sodium citrate dihydrate was compared with the fluorescence spectrum measured along the edges of the LIS using the optical setup shown in Figure 3.7. Specifically, 473 nm (for LIS) and 532 nm (for Na-citrate) CW laser excitation (20 μW) was directed towards the sample via a broad band beamsplitter, and focused to a diffraction limited spot using a 0.65 NA objective. The resulting fluorescence was collected in the reflection geometry using the same objective, passed through the beamsplitter, and directed into an optical fiber (CeramOptec, spot-to-slit fiber bundle). Emission spectra were obtained by passing light from the fiber into a 1/4 meter grating monochromoter (Acton) and onto a LN$_2$ cooled CCD camera system (Princeton Instruments). Figure 5.9 presents a compar-

75

(a)	(b)
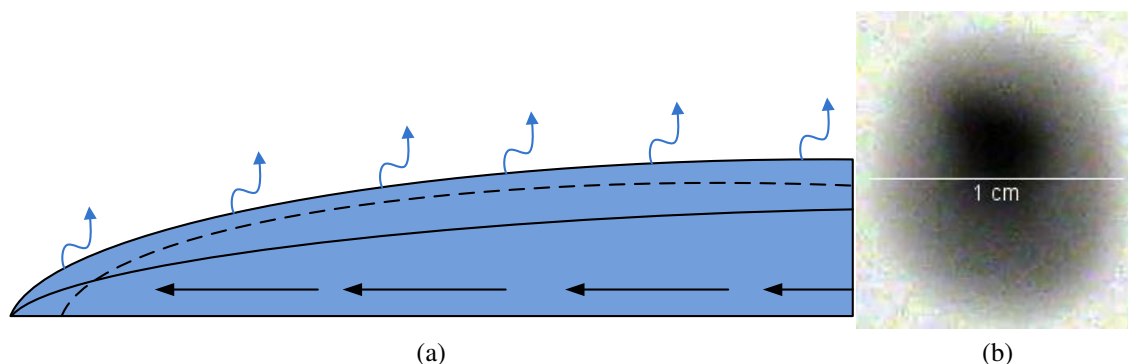
Figure 5.7. Coffee ring formation and dropcast of Ag solution. Coffee ring formation mechanism (a). Drop cast film of rotovap concentrated Ag solution (b).

ison between the fluorescence spectrum from Na-citrate dihydrate and the fluorescence spectrum measured from the edge of the LIS. In this figure, the slight difference in the curves, the red (edge of the LIS) and black (Na-citrate) curves is due to differences in the excitation and collection geometries of fluorescence but the nature of both the curves are similar. This finding strongly suggests the fluorescence source in LIS is Na-citrate. Naturally the question then arises, why is only the edge of the LIS fluorescently active when the entire coat has citrate. Potential reasons for this are:

1) During air drying of the film, the phenomena of the coffee ring effect (Deegan *et al.*, 1997; N. D. Denkov & Nagayama, 1993; Hu & Larson, 2002) occurred, leading to migration of excess citrate molecules in the solution towards the edge of the drop where the drying rate was highest, shown in Figure 5.7a (Yunker *et al.*, 2011). At the end of the drying process the majority of the excess citrate had migrated towards the rim of the drop. To quantify the citrate presence at the rim, an FTIR (Fourier transform infrared spectroscopy) spectrum was taken and is shown in Figure 5.8. The two major peaks at 1500 cm^{-1} in the FTIR graph corresponds to the carboxylic acid and peak at 3250 cm^{-1} corresponds to water. Interestingly the rim of cast drop showed emission under mercury lamp excitation. To quantify this, a fluorescence spectrum was measured and is shown in Figure 5.9.
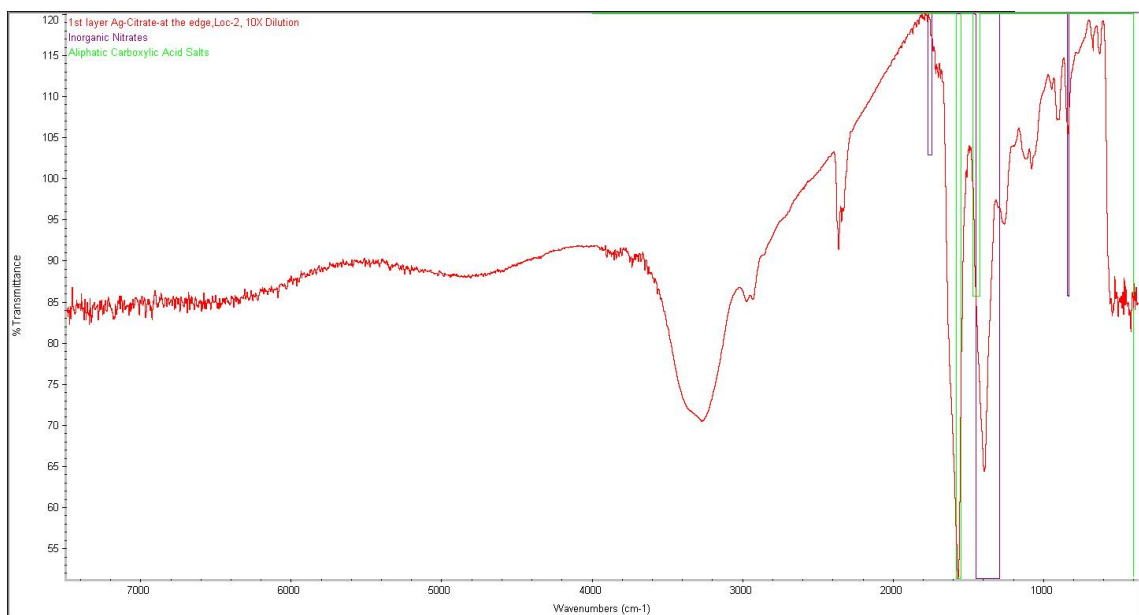
Figure 5.8. FTIR spectrum taken at the rim of the drop cast film.

2) During LIS formation the center of the laser beam has a maximum intensity resulting in maximum heat generation. This flash of heat not only creates a liquid melt pool (of Na-citrate) and vapor expansion leading to LIS, but also decomposes the material, as evident from the XRD of the LIS shown in Figure 3.13a (giving evidence of thermal decomposition). If you move away from the center of the beam, the intensity of the laser decreases and the intensity might be just enough to desorb the citrate from the Ag particle surface by removing the water molecule from citrate, as observed from the SEM micrograph (3.13b). It is also possible that during the vapor expansion process (during LIS), some of the citrate gets pushed to the sides which was not completely effected by heat (may be just loss of water molecule).

3) It is reported in the literature that metal nanoparticles have a tendency of both quenching and enhancing fluorescence, depending on the distance of the fluorophore from the surface of the metal nanoparticle (Chris D. Geddes, 2003; Wang *et al.*, 2012).

4) The fluorescence signal might be from: metal impurities present in the sodium citrate, formation of metal complexes, or from citrate itself. Further investigation is required into the source of fluorescence in the citrate molecule.
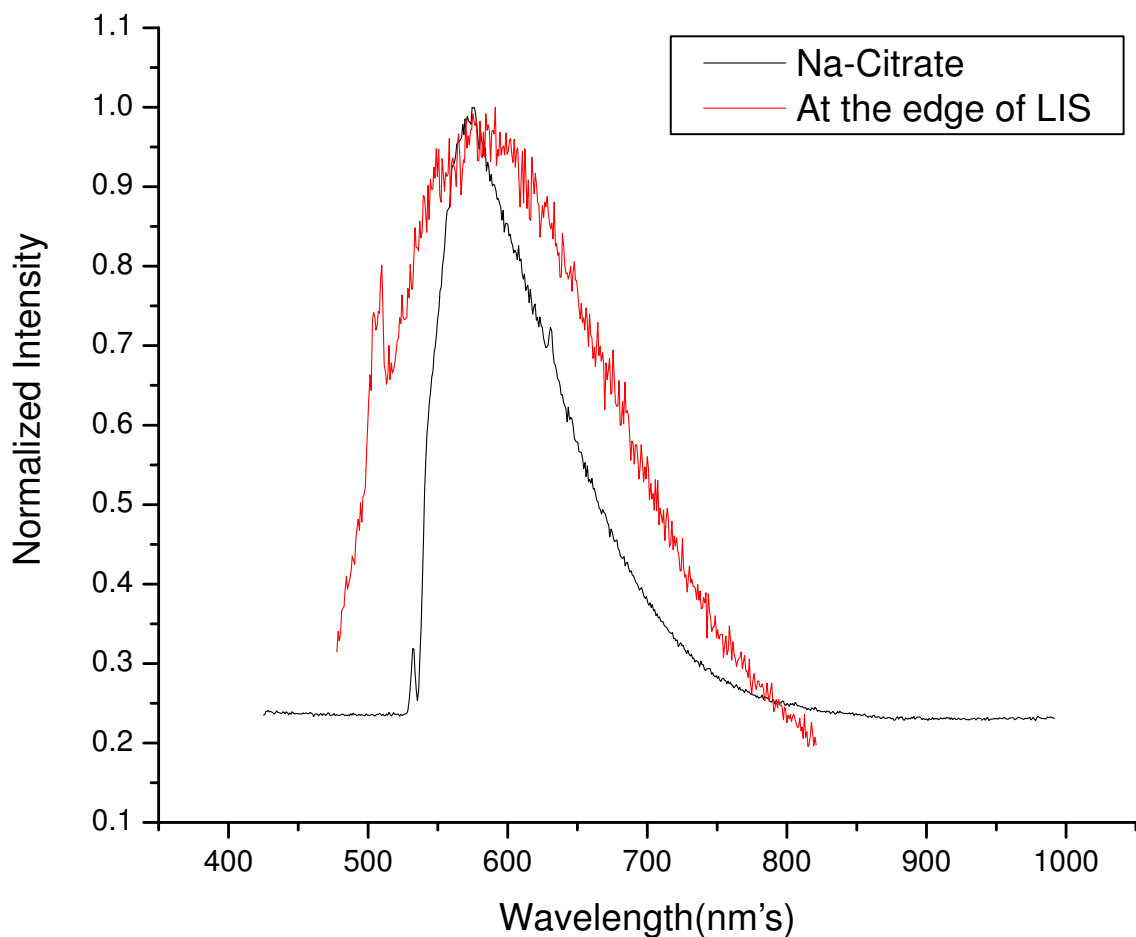
Figure 5.9. Fluorescence spectrum comparison between neat Na-citrate dihydrate and a spectra measured at the edge of a LIS.

5.2.2 Fluorescence quenching effect by water

To get further insight into the non-fluorescent nature of the drop cast film (at the regions away from the laser exposure) and to prove presence of water in sodium citrate acts as fluorescent quencher, fluorescence of citrate with varying amount of water content was measured and are shown in Figure 5.10. The blue curve denotes the fluorescence spectrum of baked citrate heated on hot plate at 75°C for half an hour to drive off all

the water, the green curve is the fluorescence spectrum of citrate out of the box which contains some bonded water molecules, the red curve is the fluorescence spectrum of drop cast film made only from citrate solution, and the black curve is the fluorescence spectrum of glass, which was used as substrate for holding citrate. These curves show how the hydrated forms of sodium citrate reduce fluorescence. Therefore, the mechanism
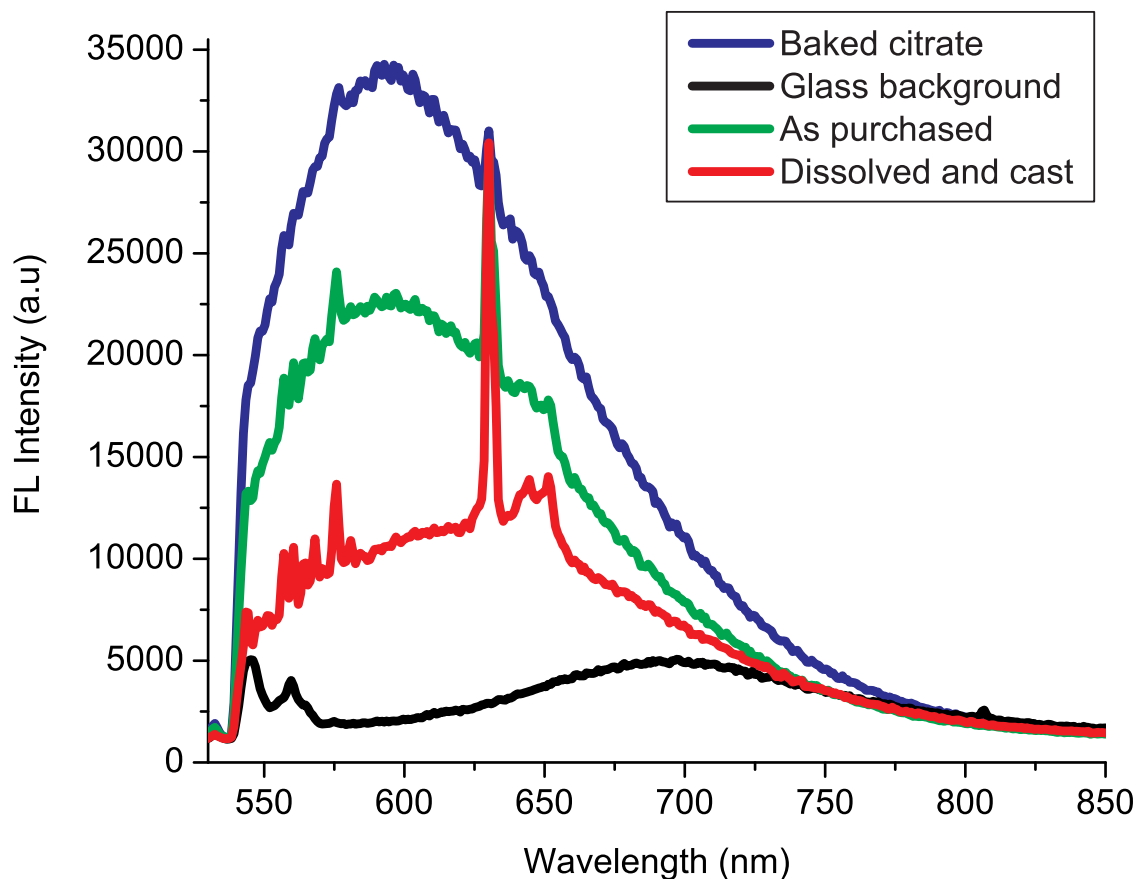
Figure 5.10. Fluorescence spectrum of citrate with varying amounts of water content.

of fluorescence seen in Figure 3.10 seems to be clear: 1) regions directly exposed to the laser increase in temperature well above the decomposition temperature of citrate, destroying the molecule, 2) regions right next to the laser exposure are heated enough to release bound water, increasing its fluorescence, and 3) regions far from the laser exposure have hydrated sodium citrate and are not fluorescently active.

5.3 Summary

To get LIS formation, a low temperature decomposing material is required around the Ag particles. The LME (liquid melt ejection) phenomena is the likely mechanism behind LIS formation, vapors (H_2O & CO_2) were identified during heat treatment (TGA) of Ag-Na-citrate film material. The source of the fluorescent signal at the LIS periphery was found to be sodium citrate dihydrate and water content in the sodium citrate dihydrate acted as its fluorescent quencher.

Chapter 6

PHOTO-PHYSICAL CHARACTERIZATION OF RARE EARTH DOPED

MATERIALS

6.1 Introduction

In recent past, rare earth doped particles have been used in various commercial products ranging from the fiber-optic thermometer (Mochida *et al.*, 2004), printing ink, ceramics, paper, emergency sign board, traffic signs (Ronda *et al.*, 1998), structural damage sensing (Akiyama *et al.*, 2002), and even children's toys (Ronda *et al.*, 1998). The reasons for widespread use of this material are bright and long lasting phosphorescence, wide absorption band, good chemical stability, non-radioactive, non-poisonous, and high conversion efficiency of energy (Mishra, 2010). Due to these interesting properties of rare earth doped materials, people are also looking into incorporating them into thin films, using them with solar cells, and medical diagnostic equipments (Karthikeyani & Jagannathan, 2000). Recent work suggests that some doped phosphors exhibit little degradation in optical efficiency at reduced dimensions (Van den Eeckhout *et al.*, 2010). However, the emission mechanism in these systems is still not fully understood and may be affected by particle size (Chander *et al.*, 2004). The nanoscale phosphors are prepared by solid state reaction, vacuum deposition, or by combustion methods, which are expensive for most commercial applications (Aruna & Mukasyan, 2008). An alternative cost-effective approach involves size reduction via mechanical milling. This approach may not be universally applicable to all nanomaterials; it may be useful for nanoparticles where the property of interest is determined by the presence of dopant ions within the particle and not the final particle dimensions. In this work, comparison of the optical properties of a commercially available $SrAl_2O_4$:Eu, Dy phosphor before and after milling. The phosphore samples were then incorporated into thin film, laid over commercially available so-

lar cells, and their effect on solar cell efficiency was studied. To improve dispersity, a low cost surfactant was also considered. Both X-ray (data not shown) (Kandpal *et al.*, 2011) and visible spectroscopic technique was used to characterize the particles and to describe the observed changes in optical efficiency. The work suggests that the size reduction leads to degradation of the phosphorescence and thermoluminescence of the phosphor but an increase in laser induced emission, providing further insight into the emission mechanism in this system.

6.2   Materials and Methods

Accurate and quantitative determination of most photophysical parameters typically requires the sample of interest to be suspended in an appropriate non-interacting solvent system. Furthermore, incorporation of nanomaterials into heterogeneous systems (such as polymer film coatings) mandates the stability of the colloid which is most efficiently obtained when well controlled particle size distributions are employed. This posed an initial challenge as the commercial phosphorescent material exhibited mean sizes in excess of a micron with broadly varying size distributions. These samples would not form stable colloids and exhibited strong light scattering, making quantification of photophysical properties nearly impossible. In order to move forward, size reduction and size control was required. The size measurement of commercially available phosphor was done using the dynamic light scattering technique using Malvern Zetasizer instrument (ZS-Nano).

To do the size measurement using the dynamic light scattering technique, a tiny amount of phosphor is dispersed in dispersant (usually water), just enough to make it look cloudy. If we add higher amounts of material then that will saturate the detector of the instrument. To avoid sedimentation of material during measurement, a higher viscosity dispersant was chosen (60% Glycerol plus 40% water).

6.2.1 Dry Ball Milling-Ceramic Tumbler

A ceramic vessel of size 5inches by 7inches, with a mixture of alumina milling beads with sizes ranging from millimeters to centimeters was used. The milling action was rotational along the circumference of the vessel crushing the particles between the inner surface of the vessel and the ball while tumbling. 100grams of phosphor material was mechanically milled in a dry ball mill for 0, 24, and 48 hours using a combination of $\approx$1cm and 3cm alumina beads. 10mg of sample was removed after 24 hours and 48 hours of milling and suspended in 60% glycerol solution for dynamic light scattering measurement. Sizes of the particles were cross checked using the Transmission Electron Microscope (TEM) (Philip-CM10). For TEM imaging, the phosphor material was suspended in water and a tiny drop (10μl) was drop casted on the carbon coated grid then allowed to air dry before being inserted into the scope.

6.2.2 Wet Ball Milling-Traditional Ceramic Tumbler

To decrease the particle size further we used wet ball milling, as this technique employs a small amount of solvent, which is expected to increase the shear force between the material, milling media, and milling vessel. 50wt% of phosphor to water was dumped into ceramic tumbler with half the volume of tumbler filled with milling media and the tumbler was rotated at 60RPM. A test sample was drawn out at 12 hours and 33 hours for size measurement using the Zetasizer. Milling with water as solvent lead to irreversible caking, making the material unusable. To overcome the caking nature, DMF (Dimethyl-formamide) was tried and it reduced the caking a lot; samples after 12 and 33 hours of milling were subjected to size measurement using Zetasizer.

6.2.3 Dry Ball Milling-Using Surfactant

In this method, we used the same ceramic tumbler, milling media, and amount of phosphor material as that of dry ball mill, but added 5wt% of PEG-20000 (Poly Ethylene

Glycol). The presence of the surfactant is expected to dramatically reduce the particle-particle interactions and minimize particle aggregation during milling. Polyethylene glycol offers the additional ability to provide some electrostatic stabilization coupled with efficient steric stabilization. Furthermore, PEG typically allows for improved stability in a range of polar to weakly polar solvents. Test samples were taken out at 12, 24, 36, and 48 hours and the size was measured using the zetasizer, the data is shown in Figure 6.2.

6.2.4 Colloid Zeta Potential

Under most processing conditions nanoparticles are dispersed or deposited as a colloid. This requires that the particle suspension be stable. Colloid stability in a number of solvent systems can be assessed by determining the zetapotential, or surface charge, of the particulate. Colloids which exhibit significant surface charge (positive or negative) are considered stable, while those with minimal surface charge are considered unstable. As a method of assessing colloid stability the particle surface charge (zetapotential) versus solution pH was determined for the 48hr dry milled material ($\approx$200nm).

6.2.5 Absorption and Emission Spectrometry

The electronic structure of these materials was probed using simple absorption/transmission measurements as well as laser stimulated absorption specifically probing the up/down conversion properties of these materials. Unless otherwise indicated all measurements were performed on dry milled Luminova material ($\approx$250nm).

6.2.6 UV-Vis Extinction Spectroscopy

In order to determine the required parameters for more detailed photophysical characterization (ex. optimal absorption wavelength, concentration), simple solution phase UV-Vis extinction spectroscopy was employed. Of specific interest here are the relative contributions of absorption and scattering to the total extinction cross-section, whereas

absorption can result in the re-emission of a photon (desirable for the proposed application) and scattering can result in a loss of photons, significantly reducing efficiency. Therefore, accurate determination of absorption properties for these systems requires the simultaneous determination of scattering properties. The procedure for UV-Vis spectroscopy is explained in Appendix C.

6.2.7 Laser Induced Emission Spectroscopy

The apparent up-conversion process in these materials was investigated using wavelength selective Laser Induced Emission Spectroscopy. For this experiment a home built laser scanning confocal instrument was used (Dr. Mike Mason optics lab). A mass (0.15 g) of the purchased phosphor (Luminova) and 48 hour milled samples was used to fill welled slide glass (Fisher brand) and closed with one inch thick cover slip using nail polish paint. Samples were stored overnight, inside the dark in a -80°C freezer before subjected to laser induced characterization to make sure of complete thermal deactivation. The sample was excited using laser 633nm, the optical setup can be seen in Figure 3.7. The confocal microscope was equipped with 0.85NA air objective, used for excitation of sample and collection of signal. The resulting emission was guided to a 1/4 m spectrometer (Acton Instruments) and liquid nitrogen cooled CCD camera (Princeton Instruments, SPEC-10). An excitation power of 6mW was used and held fixed for all samples at each wavelength, and spectra were collected over constant integration periods (10s).

6.2.8 Time-Resolved Emission Spectroscopy

In order to be considered a useful emissive material in a PV (Photo-Voltaic) device the total emission yield of the up-conversion process must be significant. Because the up-conversion process involves the absorption and re-emission of photons, the total cycle time for this process is critical. The emission lifetime is a quantitative measure of this

process. Short lifetimes (nanoseconds) indicate that GHz photon emission rates are possible while millisecond lifetimes, though long-lived, effectively reduce the total emission rate (per second) to levels too low for most device applications. Fluorescence processes typically occur on the nanosecond timescale while Phosphorescence shows microsecond to second lifetimes. To measure the, lifetime of the raw material the same optical setup as of Figure 3.7 was used with picocount software. Time-Resolved pump probe measurements were performed using picosecond pulses of 633 and 835 nm laser excitation with 20MHz repetition rate. This approach was used to determine the lifetimes of fluorescence up-conversion processes (if present), whereas continuous wave (CW) start-stop measurements were used to determine the lifetime of phosphorescence processes under similar 633 and 835 nm excitation conditions.

6.2.9 Thermo-Luminescence

As IR (Infrared) wavelengths are consistent with thermal energies, the potential conversion of thermal energy into visible photons is an indication of the up-conversion efficiency of these materials. Furthermore, as most solar PV devices are associated with excess thermal energy, thermoluminescent materials have the potential to increase the overall energy yield of PV devices. For thermoluminescent measurement, raw and 48hr dry milled material samples were used to fill welled slide glass (Fisher brand, look for depth of well) and closed with 1inch thick cover slip using nail polish paint. Samples were stored overnight, in the dark in a -80°C freezer before subjected to laser induced characterization to make sure of complete thermal deactivation. To collect the photothermal emission, a software controlled hot plate was used as a thermal source to provide a well determined temperature ramp ($\approx 1°$C per second). The photothermal emission was collected using an optical fiber cable (Thorlabs, AFS105/125Y) and was installed over the sample coverslip and guided into avalanche photodiode module (EGG, SPCM). Total temperature dependent emission was obtained by integrating each time sampled spectrum.

6.2.10 Synthesis of SrAl₂O₄:Eu, Dy Material

To investigate the feasibility of synthesizing related materials with varying Eu:Dy ratios and to characterize their photothermal properties, $SrAl_2O_4$:Eu, Dy was synthesized. As a starting point, stoichiometries approximating the commercial material were investigated in order to assess the feasibility of performing later synthesis (with varying stoichiometric ratios of dopants) in house; this corresponded to a 1:2 (Eu:Dy) ratio, stoichiometrically controlled quantities of dopant atoms (relative to the Strontium oxide glassy host material) were obtained by dissolution from commercial sources of high grade rare metal oxides. Here (Eu, Dy)Dy_2O_3(4N) & Eu_2O_3(4N) (Sigma-Aldrich) were dissolved in a small amount of HNO_3, then the solution was diluted to 0.1M Dy^{3+} and Eu^{3+}, respectively. We found that if HNO_3 was used in abundance, the later gelation steps did not proceed as desired. Then $SrCO_3$(2.86g) and $Al(NO_3)_3.9H_2O$(15g) were added to the solution of Dy^{3+}(4ml) & Eu^{3+}(2ml), respectively. After the $SrCO_3$ was dissolved completely, 10ml distilled water, 20g urea & 20g ammonium acetic was added to the mixture. The mixture was heated at 85°C for 15 hours until the gel was formed. Following gellation, the mixture was transferred into a clean parabolic porcelain crucible suitable for temperatures in excess of 1200°C. This was then placed in a muffle furnace maintained at 600°C, where the gel boiled and underwent dehydration initially, then was followed by decomposition with an evolution of large amounts of gases (oxide of carbon, nitrogen and ammonia), and finally, the foamy precursor was produced by the spontaneous combustion with enormous volume expansion (here expansion was greater than a factor of 20 and care had to be taken to not overfill the crucible with gel). The whole process was over within less than 5 minutes. The voluminous and foamy combustion ash was annealed at 800°C in an air atmosphere for 4 hours to remove the residual carbon. The well-milled precursor powder was subsequently annealed at temperature 1200°C for 2 hours in an active carbon atmosphere to produce $SrAl_2O_4$:Eu^{2+},Dy^{3+} phosphor. The qualitative analysis of the

prepared material appeared following sintering as an extremely fine powder and required no milling prior to analysis. Samples were opaque white, similar to commercial materials. Samples showed phosphorescence under UV excitation, but with a reduced intensity as compared to commercial materials. The recipe for the synthesis of the phosphor was taken from Zhao *et al.* (2006) and Son *et al.* (2009).

6.2.11   Quantitative Analysis of Synthesized Material

Resulting materials were assessed by fluorescence emission spectroscopy. To better assess the broad band photoresponse of the as prepared materials, laser excitation was performed continuously at 473 nm (blue) and separately at 633 nm (red). Emission was collected using a grating spectrometer (Acton instruments) with a 150 grooves/mm grating, blazed at 500nm. Samples were prepared in a welled 100mL volume welled slide glass, capped with a 1 inch thick coverslip, and sealed with cytoseal. Data was acquired in a custom build spectral imaging microscope shown in Figure 3.7. Typical spectral acquisition times were 1ms.

6.2.12   Preparation of Photovoltaic's Film Coatings

This section describes the process of incorporation of milled material into polymer, deposition as thin film onto PV devices and assessment of PV efficiency under constant solar illumination, as well as periodic illumination (cycled excitation) as compared to uncoated devices. Due to its relative cost, ease of use, and optical transparency, Poly(methyl methacrylate) (PMMA) was selected as the host polymer for the nanoparticle doped film coatings. The dip coating preparation method is quite simple and requires little specialized equipment. It is worth noting that spin coating methods were also investigated, making use of a commercial spin coating instrument, but no advantages were observed, and the additional time required for this method was not warranted. For the dip coating method, PMMA was dissolved in CCl4 at a 25wt%. This was stirred slowly (several

minutes) until the polymer was completely dissolved. To this solution, 48hr milled phosphor particles were added to achieve a solution of 4wt% particle, relative to the solvent. This same method was used to prepare the original material (unmilled). To facilitate dip coating, volumes of 50mL were prepared. Dip coating was performed directly on the commercial PV devices (AM-5610CAR/869-1009-ND, 25mm x 20mm). Here the entire PV device was immersed vertically in the polymer/particle solution for a period of 2 seconds, removed slowly, and allowed to dry (1 Layer dip). For the second dip layer, the sample was rotated 180 degrees, and the dip process was repeated (2 Layer dip). After drying, the films appeared to be slightly opaque. Here it was found that the unmilled material formed very inhomogeneous films. These were not used for further PV conversion studies.

| (a) | (b) | (c) |
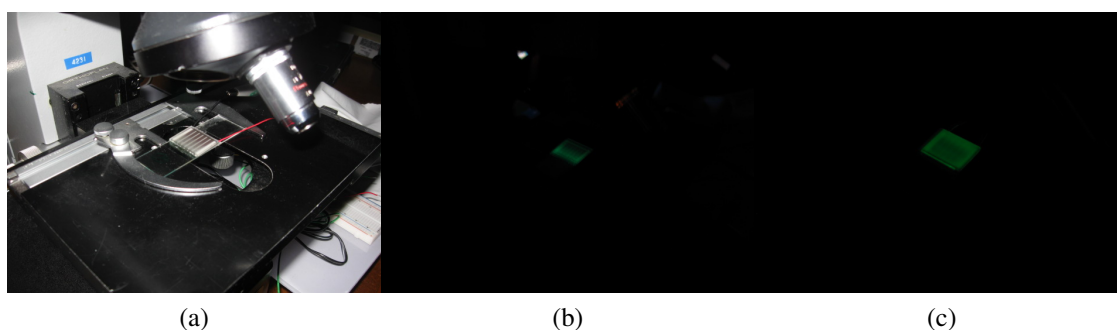
Figure 6.1. Photo's of PV cell with and without dip coat. Commercial PV (a). Dip coated single layer (b). Dip coated double layer

6.3 Results and Discussion

6.3.1 Size Measurement of Milled and Unmilled Material

Malvren Zetasizer Nano-ZS was used to measure size of the particles and surface charge of the particles, for detailed procedures please refer to the Malvren Zetasizer manual and APPENDIX C. The graph (Figure 6.2) between the percentage volume of particles verses their diameter. The region under the curve gives the size distribution of the parti-

89
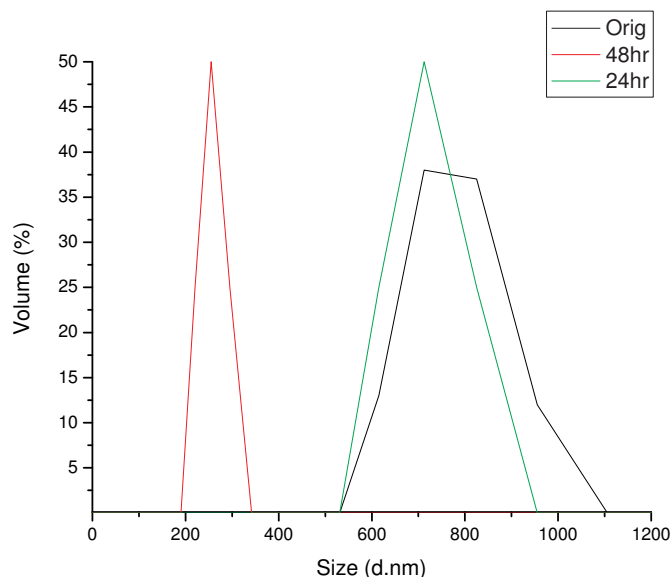
Figure 6.2. Size comparison of 24hr, 48hr dry ball milled phosphor with unmilled phosphor.

cles. Integration of the area under the curve gives the total volume of the particles. The size was reduced to 250nm from 1μm after milling for 48 hours.

6.3.2 Transmission Electron Microscopy Images of Milled and Unmilled Material

To know the shape of the particles and to validate the DLS (Dynamic light scattering) size data (Figure 6.2), TEM images were taken. During sample preparation for TEM imaging, the unmilled material was sonicated for 10minutes with the intention to disperse it effectively. The TEM images suggest that the sonication had an adverse effect on the surface of the material and it was not employed further for sample dispersion. In Figure 6.4 clearly shows the decrease in size with milling time.

6.3.3 Size Measurement of Wet Milled Material

The graph (Figure 6.5) is between volume% versus diameter of the wet milled (DMF solvent) phosphor particles. Irreversible caking was formed when water was used as solvent, this may be due to silicate hydrolysis, making the material unusable. Attempts

(a) Unmilled   (b) Unmilled with sonication
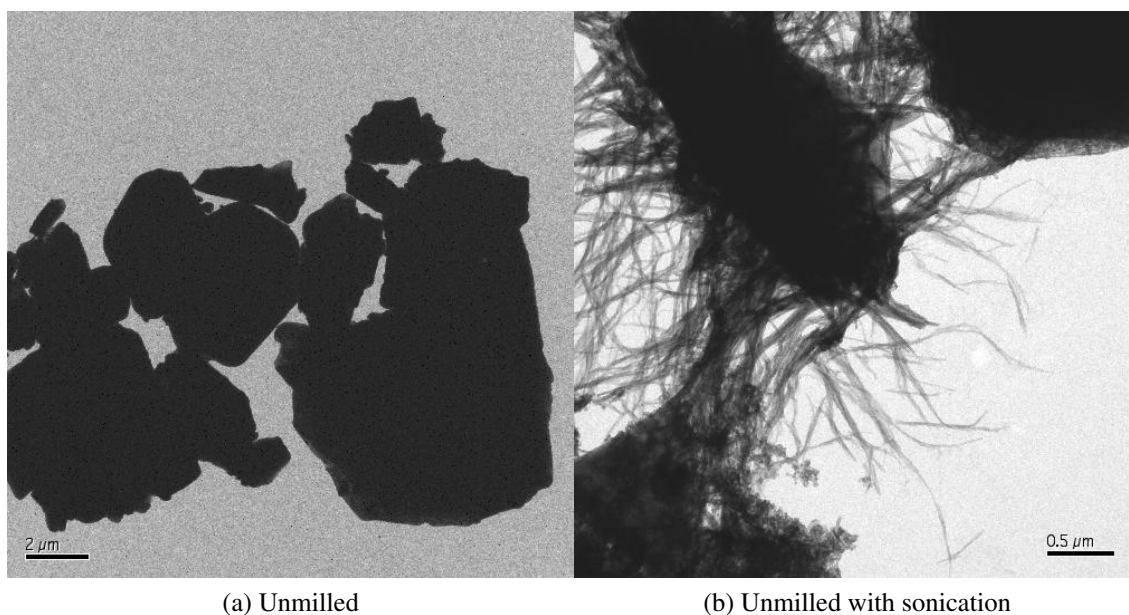
Figure 6.3. TEM images of unmilled material and 10minutes sonicated unmilled material. Unmilled (a). Unmilled with sonication (b).

(a)   (b)
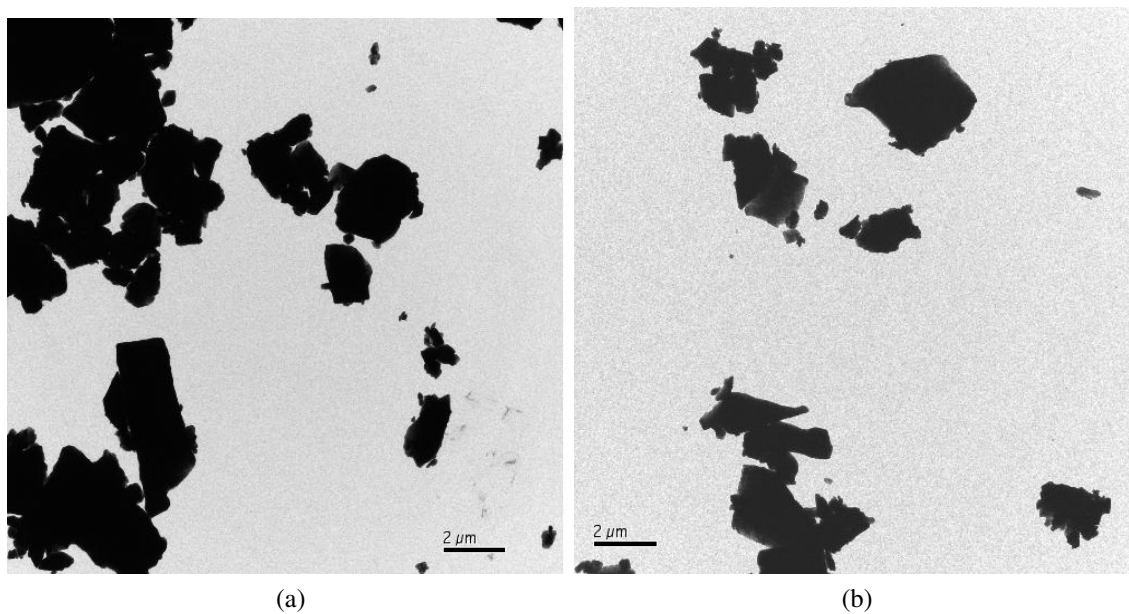
Figure 6.4. TEM images of 24 hours and 48 hours milled materials. 24 hours milled (a). 48 hours milled (b).

were made to resuspend this cake via sonication but resultant material showed dimensions much greater than 1 micron. Caking was significantly reduced with DMF solvent.

91
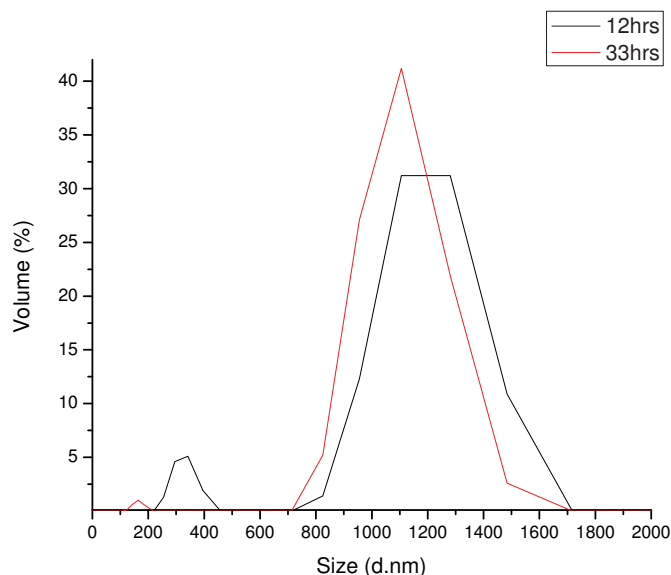
Figure 6.5. Size comparison of 12hr, 33hr wet ball milled phosphor.

The resultant suspension was sized by DLS and showed bimodal size distributions (Figure 6.5). The bulk of the material still exhibited diameters of approximately 1 micron, likely due to localized aggregation of smaller particles. However, a significant fraction of the 12 and 33 hour wet milled material exhibited diameters of 300 and 150 nm, respectively. Ethanol was also investigated as an alternative to DMF (data not shown), while the particle size appeared to be larger, caking was significantly reduced. Subsequent solution phase optical measurements were preformed in 60wt% glycerol/ethanol to reduce sedimentation. Further size reduction and reduction of caking/aggregation was expected with the use of a suitable surfactant (i.e. CTAB (cetyltrimethylammonium bromide) or polyethylene glycol).

6.3.4 Size Measurement of Dry Milled With PEG as Surfactant

With the use of PEG surfactant, caking was significantly reduced. Resultant suspension was sized by DLS and showed mean sizes in the 100-200 nm range (Figure 6.6). Interestingly, efficient size reduction appears to occur within the first 12 hours, obviating

the need for longer milling times. As such, 12hour dry PEG milled material is recommended for later studies.
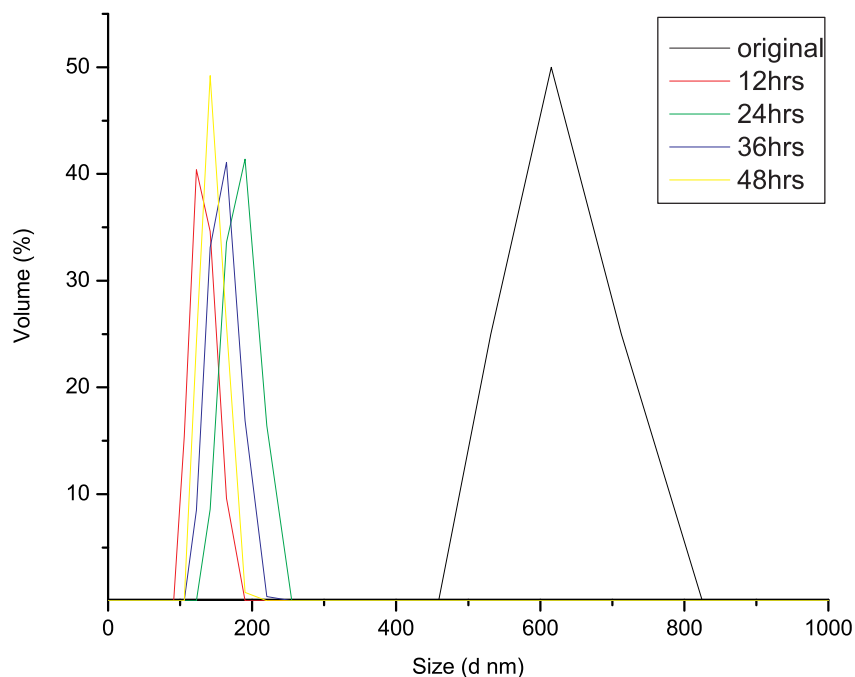
Figure 6.6. DLS data of samples dry milled with polyethylene glycol surfactant vs. milling time.

6.3.5 Zeta-Potential Measurement of Raw Material

The graph (Figure 6.7) shows how surface charge varies over a range of pH values. An iso-electric point is that point on the pH scale where the net charge on the surface of the particle is zero, this is the highly unstable state of the colloid and the solution will crash out quickly. In the graph (Figure 6.7), the values (in mV) above and below 0 mV indicate relative stability at very low and modestly high pH levels.
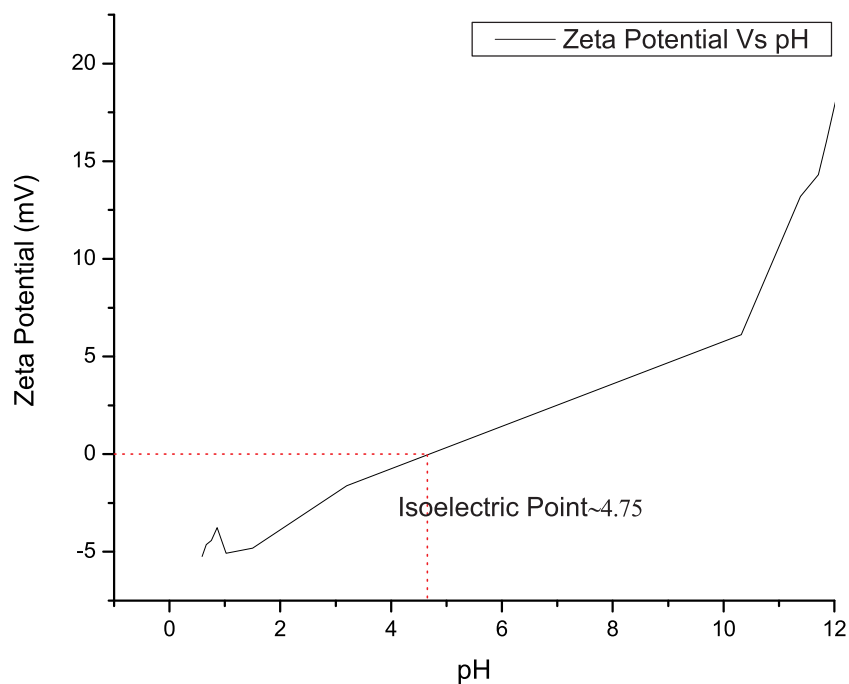
Figure 6.7. Zeta potential vs. pH curve for 48 hr dry milled material.

(a)

(b)
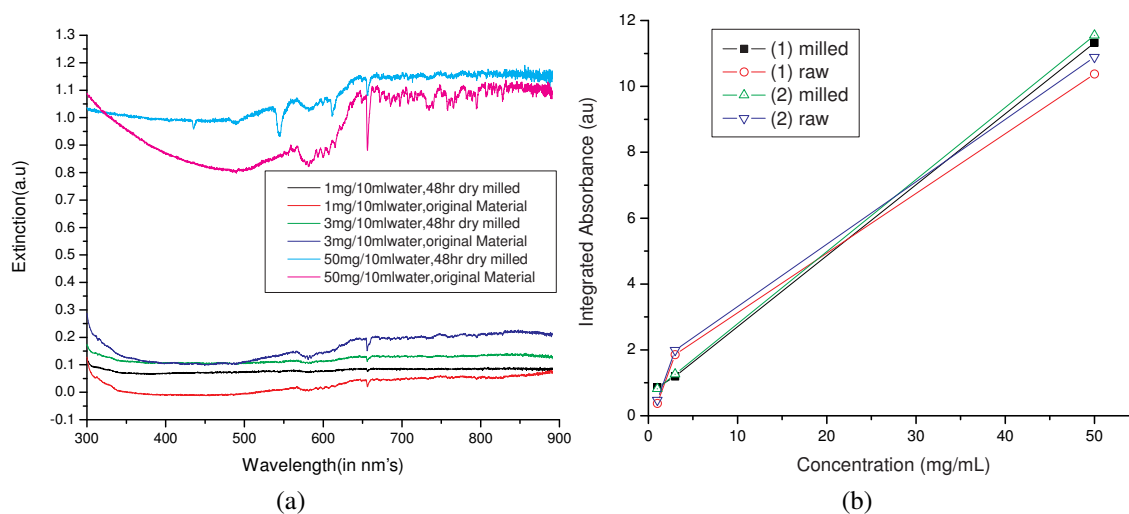
Figure 6.8. UV-Vis Extinction Spectra comparison of milled and unmilled phosphor. Extinction vs. material concentration for 48 dry milled and raw material (a). Concentration dependence of extinction for milled vs. raw material in the ranges 655-665 nm (1) and 700-710 nm (2) (b).

6.3.6   UV-Vis Extinction Spectroscopy

A comparison of the milled and raw material was performed to determine if the process significantly alters the photophysical properties of the material. Primarily the extinction versus concentration and size (milling time) were investigated. An approximate linear dependence between concentration and integrated absorbance (Figure 6.8b) was determined with a mean slope = 0.21442. This implies that the extinction properties are well behaved. It should be pointed out however, that in this measurement, scattering is also present and must be excluded in order to obtain accurate absorbance data. To more accurately determine the absorption properties, particle scattering was measured independently (at 90 degree geometry), and subsequently removed from the extinction spectra. The resulting data represents the pure absorption spectra (Figure 6.9).
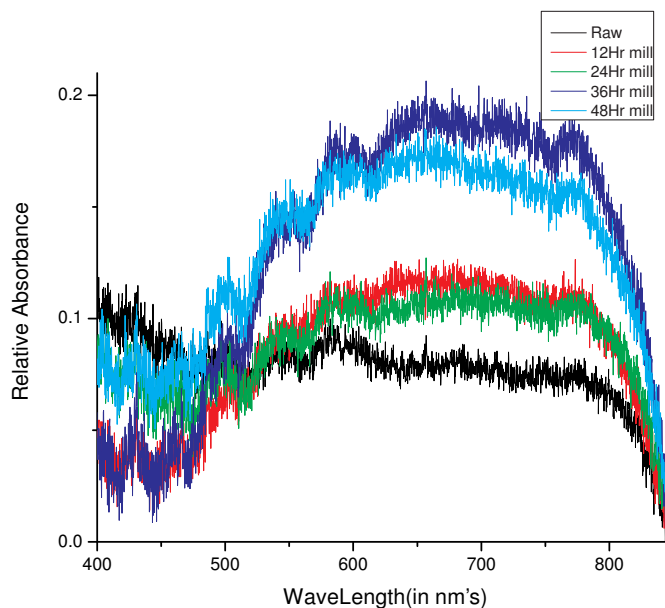
Figure 6.9. Relative absorbance vs. milling time excluding scattering component of extinction.

Interestingly, the absorbance increases significantly for longer milling times compared to the raw sample. Indeed, this suggests that scattering may be dominant in the larger unmilled material further supporting the need for size control via milling. Using the pure absorbance data, molar absorptivity (absorption) coefficients can be determined. These

Sample	ε (L/g cm)	σ(cm²)/MW
Raw (Luminova)	0.05	$2.0 * 10^{-22}$
12 Hr milled	0.07	$2.3 * 10^{-22}$
24 Hr milled	0.06	$2.5 * 10^{-22}$
36 Hr milled	0.11	$4.8 * 10^{-22}$
48 Hr milled	0.12	$5.0 * 10^{-22}$
PbS quantum dot	0.5	$2.0 * 10^{-21}$
Cy7	50	$2.0 * 10^{-19}$

Table 6.1. Comparison of absorption coefficient of milled material with dye and quantum dot.

values allow for more meaningful comparison of the optical activity of the material. They can be obtained (approximately), using Beer's law were Absorbance = εbC. Here b is the optical path length (1cm), C is the particle concentration (in mg/mL or moles/L), and ε is the molar absorptivity (or molar extinction coefficient for absorption). The absorption cross-section (σ) can then be directly calculated from the extinction coefficient: $\sigma = 2.303\varepsilon/NA$.

It is important to note that in the case of absorbing (and scattering) nanoparticles, a general assumption is made that all absorbers in the measured solution act independently of one another with regard to the light source. Clearly, this is not the case with larger nanoparticles which can shadow one another from the incident light source. For the device application proposed, this shadowing effect is also expected to be present. As such the calculated values for the extinction coefficient can be considered "effective" values, having specific relevance for the system under study. With these values, optimal loading conditions can be predicted. The cross-section in particular yields an effective optical dimension which can be compared to the physical dimension in thin 2D films.

6.3.7   Laser Induced Emission Spectroscopy

The apparent upconversion process in these materials was investigated using wavelength selective Laser Induced Emission Spectroscopy. Specifically, the spectral signature of upconversion and downconversion processes were compared versus excitation wavelength as a means of further assessing the photophysical process. The narrow peak is
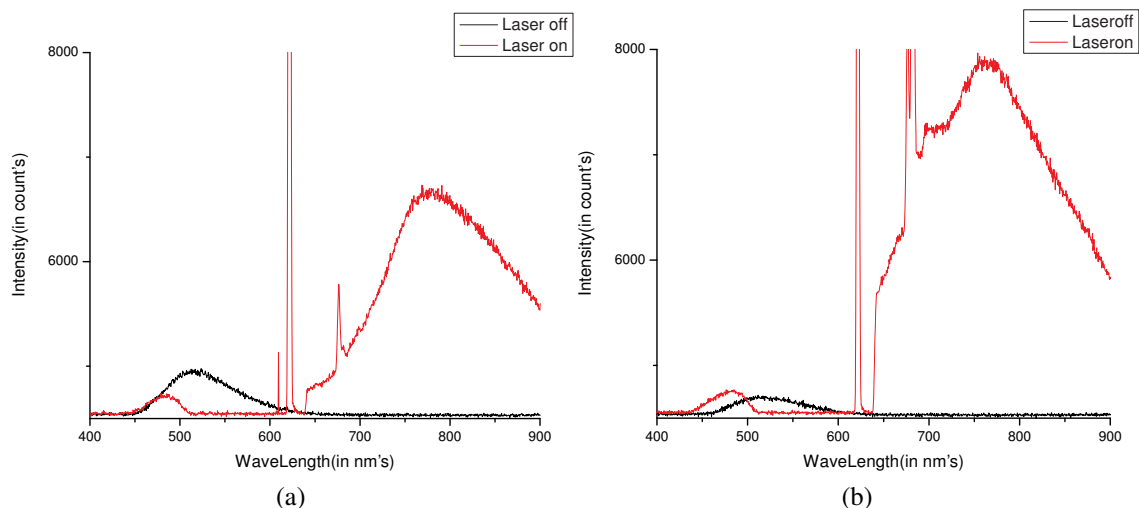
Figure 6.10. Total stimulated emission spectral line shapes under 633nm excitation (red). Unmilled (a). 48hr milled (b).

due to bleed-through of the 633nm excitation laser. For both the raw and milled samples, 633nm efficiently excites both up and down conversion processes. Qualitatively, down conversion is more efficient for the milled samples while up conversion efficiency is slightly more efficient. Interestingly, the slow phosphorescence process is less efficient for the milled samples. This discrepancy may be due to stimulated depletion of the triplet state, effectively reducing the triplet lifetime and allowing for a greater fraction of transitions occurring through the faster emission states.

6.3.8   Time-Resolved Emission Spectroscopy

Time-Resolved pump probe measurements were performed using picosecond pulses of 633 and 835 nm laser excitation with 20MHz repetition rate. This approach was used

to determine the lifetimes of fluorescence upconversion processes (if present), whereas continous wave (CW) start-stop measurements were used to determine the lifetime of phosphorescence processes under similar 633 and 835 nm excitation conditions.
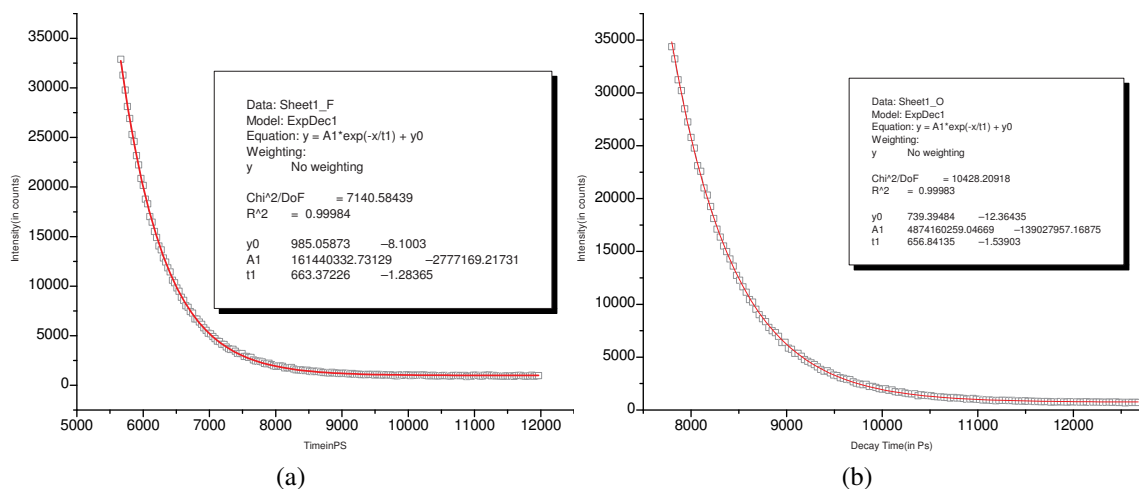
Figure 6.11. Time-resolved up converted emission under 20 MHz pulsed laser excitation. 633nm pulsed excitation (a). 835nm pulsed excitation (b).

Exc/Coll Geometry	Measuring	Lifetime (ps)	Uncertainty ($\pm$ps)
633/No Filter	Control (Total Em.)	237.7102	1.193
633/630 SP	Up conversion	663.3723	1.284
633/647 LP	Down conversion	666.7401	1.343
833/800 SP	Up conversion	656.8414	1.539
833/830 LP	Down conversion	387.4822	1.525

Table 6.2. Decay constants obtained from single exponential fits for all excitation and collection geometries.

CW start-stop measurements were used to determine the lifetime of phosphorescence processes under similar 633 and 835 nm excitation conditions.

Decay constants obtained from single exponential fits indicate lifetimes of $\tau = \sim 750$ and 850 seconds, respectively. These long times are indicative of phosphorescence via a slow triplet excited state. Under both 633 and 835 nm excitation a single ~ 0.5 ns
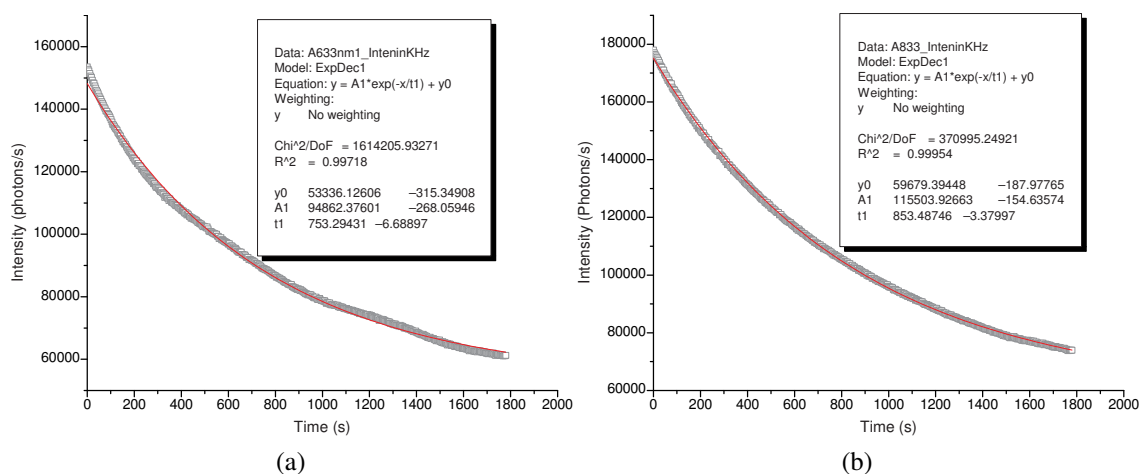
Figure 6.12. Time-resolved emission under 633nm and 835nm CW laser excitation for phosphorescence life time measurement. 633nm CW excitation (a). 835nm CW excitation (b).

lifetime was measured (multiexponential analysis showed no further mechanisms were present). Under similar excitation conditions weak phosphorescence was observed with a lifetime on the order of seconds. The short fluorescence emission lifetime and long phosphorescence lifetime suggests that this material has potential as a photovoltaic's (PV) additive. The various excitation and collection geometries provide insight into the nature of the emission mechanism and place practical limits on the material as an emitter. The lifetimes represent the reciprocal of the upper limit of possible emission (in Hz). For example, a 1 ns lifetime suggests that a given emitter can generate no more than 10^9 photons per second. An emitter with a phosphorescent triplet lifetime of 800 s, on the other hand, can generate only 1 photon per 800 seconds. While bulk of phosphorescent samples appear to glow brightly for extended periods of time, they do so with relatively low flux (photons per unit time per unit area) compared to systems with shorter lifetimes. Hence, shorter lifetimes are implicated for device design. The discrepancy between the two lifetimes present makes ratiometric analysis (determination of the relative contribution of each process) extremely difficult. However, qualitative analysis of upconverted

emission (fast component vs. slow component) (Table 6.3), suggests that the fast process dominates the total emission. This is estimated by comparing the peak emission rates.

	Fast Component	Slow Component
Lifetime	700 ps	800 s
Max Count (photons/bin)	50,000	150,000
Bin Width (s)	$33.9 * 10^{-12}$	1
Flux (photons/s)	$1.5 * 10^{15}$	$1.5 * 10^{5}$

Table 6.3. Comparison of slow and fast component lifetime, flux, maximum count of photon.

6.3.9   Thermo-Luminescence
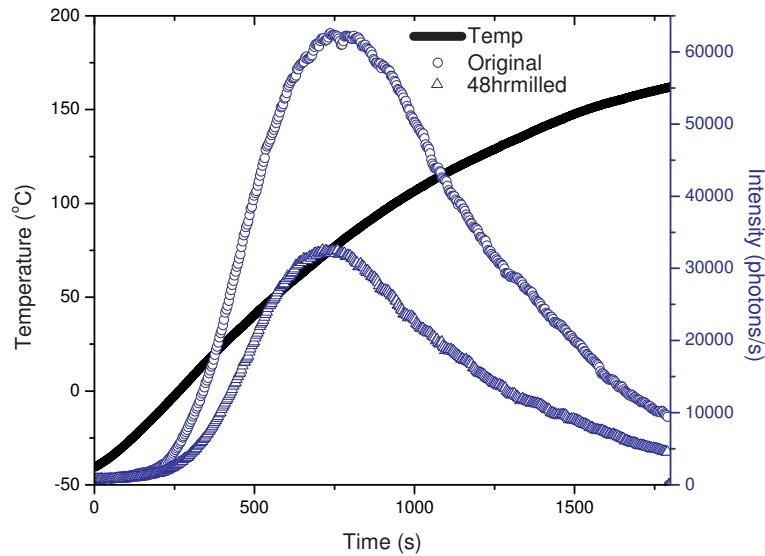
Figure 6.13. Emission vs. heating profile for raw and 48hr milled material under monotonic heating conditions 0 to 200° C.

This graph (Figure 6.13) shows that the emission from milled material is half of the emissions from the raw material and the peak emission occurs at different temperatures. The emission follows a descending trend once it reaches the maximum intensity. The reason may be because of stimulated emission of holes trapped by dysprosium in the matrix of the material, which is according to the proposed mechanism in literature.
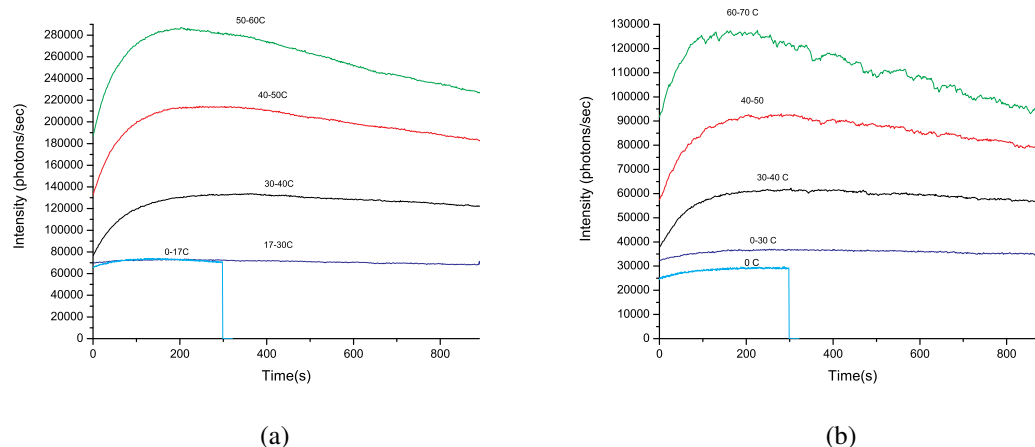
Figure 6.14. Emission vs. heating profiles for raw and 48hr milled material. unmilled (a). 48hr dry milled (b).

Both the raw and milled materials showed (Figure 6.14) significant thermal induced visible photon emission at only modest temperatures. The emission from the milled material is much lower compared to the raw material. The graph shows higher emission rates at higher temperatures but at the same time there is increased rate of decrease in emission rate at higher temperatures.

6.3.10   Quantitative Analysis of Synthesized Material

The synthesized material was characterized using fluorescence emission spectroscopy and compared with the original, and the 48hr dry milled material.

The milled material exhibits similar spectral linewidths at both 473 nm and 633 nm . The emission intensity is slightly reduced for the milled material under 473nm excitation and enhanced under 633 nm excitation for the milled material relative to the commercial material (Figure 6.15, Figure 6.16).

When excited at 473 nm the synthesized material (Figure 6.17) shows dramatically different spectra than the milled commercial material (6.15b). Specifically the emission peak around 550 nm is dramatically reduced, and a strong broad emission peak is ob-
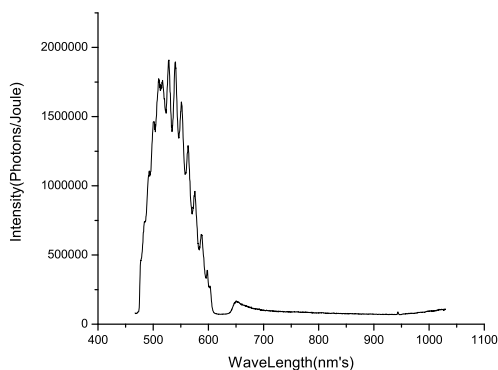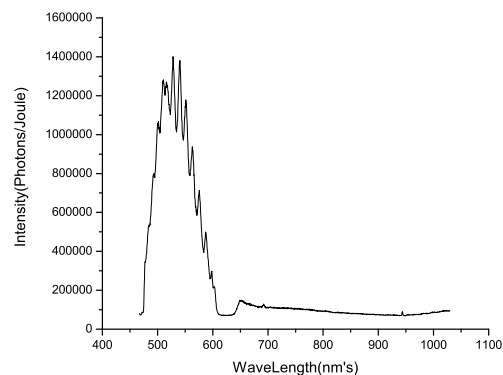
(a)   (b)

Figure 6.15. Comparison of laser stimulated fluorescence emission spectra for unmilled and 48hr milled phosphor, excitation was performed at 473 nm. unmilled (a). 48hr dry milled (b).
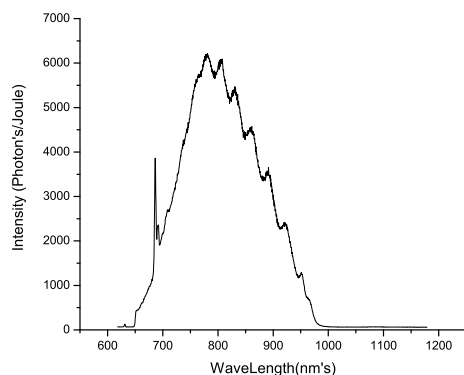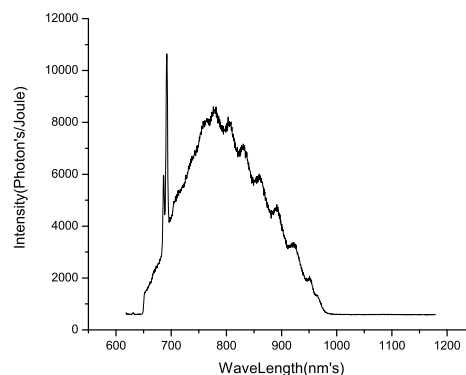
(a)   (b)

Figure 6.16. Comparison of laser stimulated fluorescence emission spectra for unmilled and 48hr milled material, excitation was performed at 633 nm. unmilled (a). 48hr dry milled (b).

served at 800 nm (near IR). In contrast, under 633 nm excitation (6.20b, 6.16b) a strong

peak centered at 800 nm is observed in both the synthesized and the milled commercial

samples, in the synthesized sample, this peak is significantly narrower.
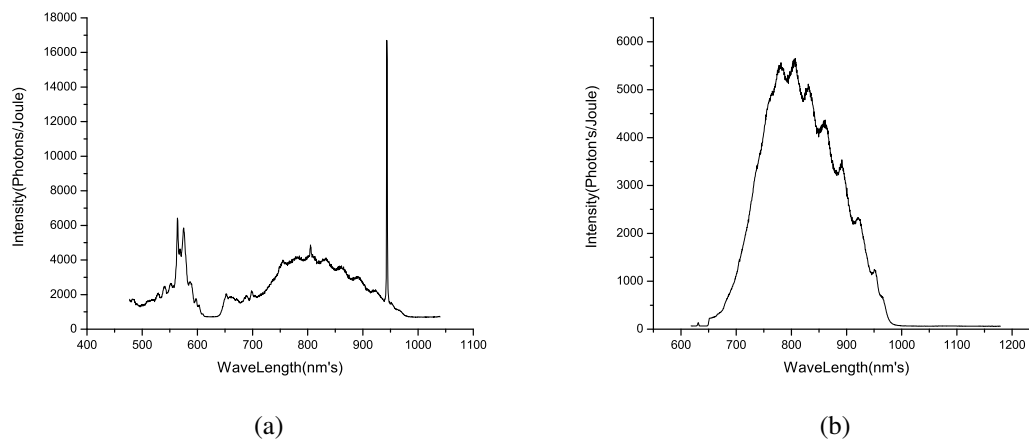
Figure 6.17. Representative fluorescence emission spectra for as synthesized material excited at 473 nm and 633 nm. Synthesized material with 473nm excitation (a). Synthesized material with 633nm excitation (b).

6.3.11   Quantitative Analysis of Dip Coated PV Cell

Dip coated samples were analyzed for PV conversion under thermal excitation (in the absence of light) and under constant illumination with a solar simulator lamp. For comparison, all PV devices were assessed before and after film application. Samples were fixed on a reflection microscope where collimated but incoherent simulated solar radiation was used to uniformly bathe the entire PV surface. For thermal measurements, an electronically controlled Peltier device was used to heat the PV device from the back side. An IR temperature probe was used to assess the device temperature throughout operation. A custom LabVIEW program was generated to record the PV output signal for each temperature setpoint. Complete emission spectra were also acquired at each temperature point. As reported previously, the phosphor material exhibits significant light emission when heated. At only 4wt% (phosphor in polymer), peak output voltages of ≈ 0.15 v were obtained when operated at $\approx 120°C$. At temperatures above this point, emission diminishes quickly, and ultimately vanishes. As reported previously, at constant temper-

103
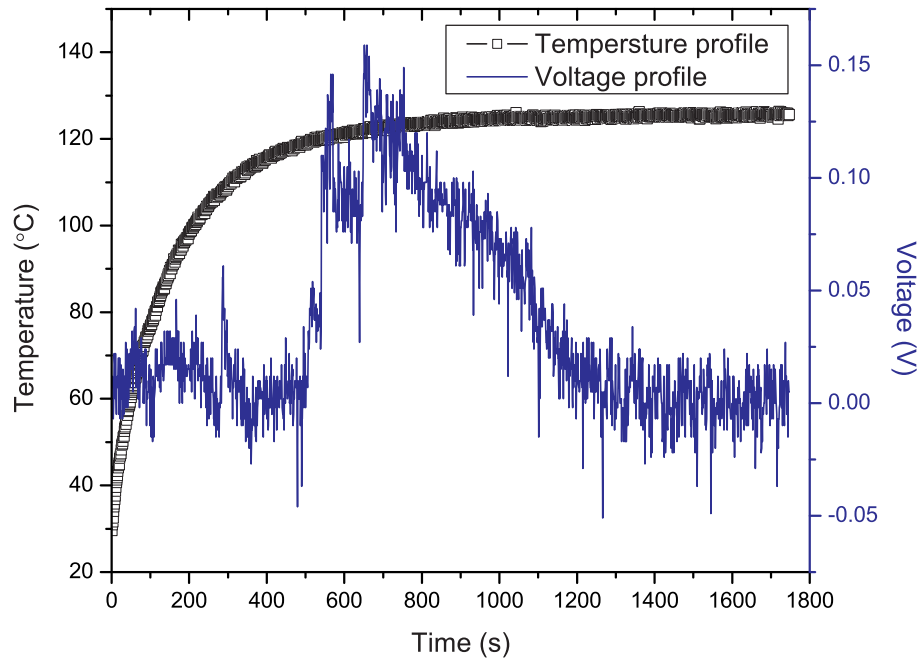
Figure 6.18. Temperature voltage response of PV device with 4 wt% dip coated phosphor film under thermal excitation only.

atures, emission intensity gradually diminishes. This suggests that under varying thermal excitation (hot-cold-hot), a maximum in the time-integrated emission might be achieved.

(a)

(b)
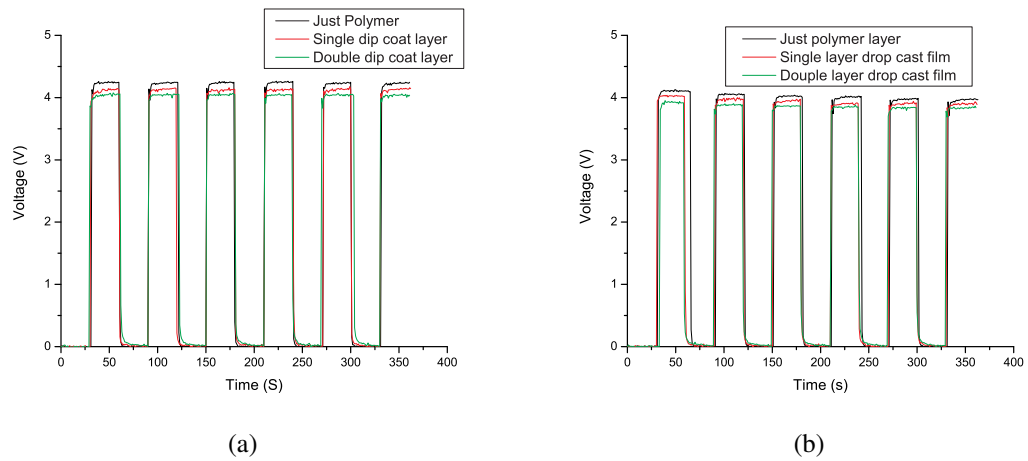
Figure 6.19. PV device voltage response versus periodic illumination at 27°C and 38.5°C temperatures. At 27°C (a). At 38.5°C (b).
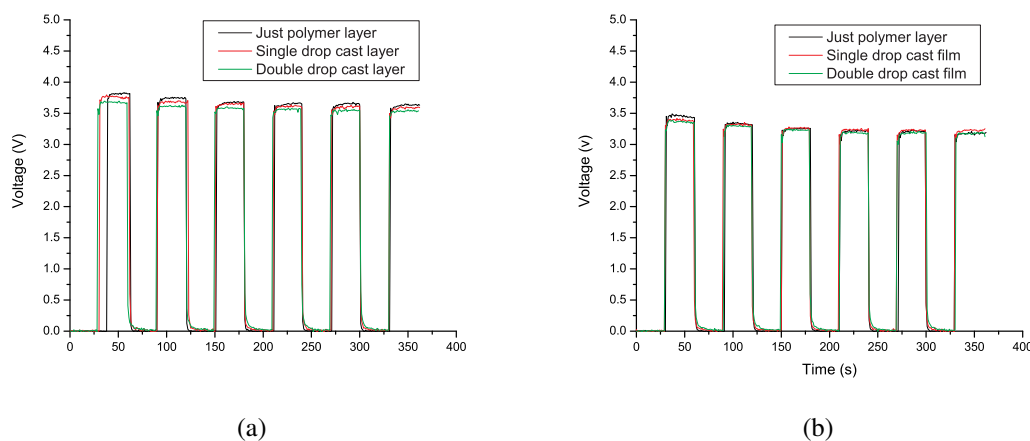
Figure 6.20. PV device voltage response versus periodic illumination at 60 and 80°C temperatures. At 60°C (a). At 80°C (b).

In graph Figure 6.19, Figure 6.20 PV device response under periodic illumination at four different temperatures are compared. The samples compared were just polymer film (PMMA (Poly methyl methacrylate)), single dipcoated 48 hour milled phosphore layer, and a double dipcoated 48 hour phosphore layer. The data in the Figure 6.19 and Figure 6.20 is extremely rich and should be carefully studied. First, the mean intensity of the periods under illumination (PV-ON) were compared for the three PV preparations at all 4 temperatures. Here it is refereed to as the ON periods.

Temperature	Mean V-Illumination during ON periods		
	Neat Film	1 Dip Layer	2 Dip Layer
27°C	4.22 V	4.12 V	4.03 V
38.5°C	4.04 V	3.97 V	3.88 V
60°C	3.73 V	3.67 V	3.7 V
82°C	3.33 V	3.32 V	3.29 V

Table 6.4. Mean voltage comparison during ON period.

At or around room temperature, the neat PV devices perform at significantly higher levels than the devices containing the nanoparticle films. However, at elevated temperatures,

all three systems exhibit nearly identical performance. Second, the OFF periods were analyzed to account for possible contributions due to phosphorescence component.

(a)   (b)
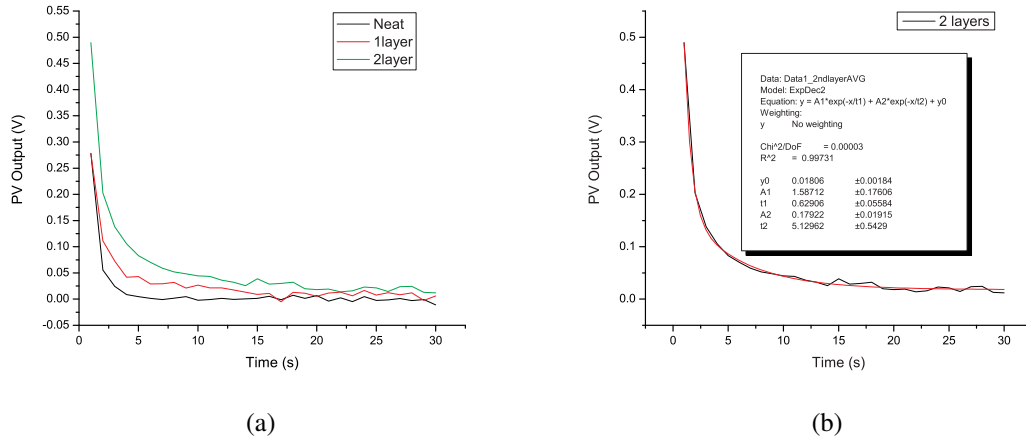
Figure 6.21. Comparison of average of all OFF periods for three sample types at 27°C and its representative exponential fit. Comparison of average of all OFF periods for three sample types (Neat, 1 layer, 2 layers) at 27°C (a). Representative exponential fit for 27°C data (2 Layers), Data (black squares), fit (red) (b).

In the graph shown in Figure 6.21 the OFF periods were compared. To account for the gradual decay in signal, an exponential fit to the data was performed and the peak amplitude and decay constants were extracted. The best fit was obtained when a double exponential was used.

In the graph, the OFF periods were compared. To account for the gradual decay in signal, an exponential fit to the data was performed and the peak amplitude and decay constants were extracted. The best fit was obtained when a double exponential was used.

$$y = y_0 + A_1 e^{-t/\tau_1} + A_2 e^{-t/\tau_2} \tag{6.1}$$

Since primary interest is in determining the intensity versus time, and not elucidating the underlying physical phenomena responsible for it, this somewhat phenomenological approach is satisfactory. This was repeated for each temperature and is tabulated below (uncertainties in fit parameters are not shown, but were generally less than +/- 5%).

Temperature	Sample	A_1	τ_1	A_2	τ_2
27°C	Neat	1.41	0.54	0.07	1.96
	1 Layer	0.82	0.72	0.08	5.50
	2 Layers	1.67	0.6	0.19	4.75
38.5°C	Neat	1.1	0.51	0.08	2.08
	1 Layer	4.95	0.43	0.17	3.4
	2 Layers	1.97	0.67	0.2	4.91
60°C	Neat	0.56	0.66	0.02	4.32
	1 Layer	1.06	0.78	0.08	7.64
	2 Layers	1.6	0.66	0.23	4.79
82°C	Neat	1.38	0.48	0.11	1.8
	1 Layer	0.9	0.83	0.09	5.93
	2 Layers	1.59	0.69	0.21	4.74

Table 6.5. Decay constants and amplitude of 2nd exponential fit of OFF period curves.

Due to the very rapid signal decay in the neat device preparation, the resulting fit decay constants and amplitudes did not trend well with the coated PV device data. However, this is not a requirement when comparing only intensity versus time. In contrast, the 1 and 2 Layer data trends well with temperature. Furthermore, as the number of film layers are increased, the overall efficiency for all temperatures increases. Interestingly, for a single film, the peak response occurs at high frequencies at 38°C, whereas, for a 2 layer system the peak efficiency occurs at 60°C. This makes sense if one considers that the additional signal is largely due to the thermal response of the material, for multiple layers this contribution becomes larger (greater termperature dependence). For increasing numbers of layers this may continue to trend up, however, increased scattering losses must also be considered.

6.4 Conclusion

Generally, the photoactive film coatings do demonstrate a measured PV response. However, the scattering losses due to the addition of nanoparticulates reduce the amount of "solar" radiation hitting the PV device surface. While it is evident that, under constant illumination, the photoactive films do add back some additional reemissions, via fluorescence upconversion or downconversion, radiation in the direction of the PV active element, the net losses are greater than the net gains. At elevated temperatures the gain term is larger (due to thermal activation of the phosphor), but the net losses still dominate. What may be interesting is the temporal response. Here the longer-lived phosphorescence mechanism becomes activated and continues to emit during the off period, though with decreasing intensity. When the pulse duration (here varied by changing the pulse frequency over a fixed time interval), is decreased, the relative phosphorescence contribution increases. This effect is accentuated at elevated temperatures. When one considers that in typical solar PV applications elevated temperatures are common, and off periods do exist (clouds, night time), the observed periodic response may be significant. Furthermore, yet as undetermined applications may be considered where this material system can yield some net benefits.

Chapter 7
CONCLUSIONS AND FUTURE WORK

7.1   Conclusions

A relatively simple method was developed whereby micron sized line features can be generated using low power focused CW laser illumination of silver nanoparticle films. The resulting Light Induced Structures (LIS) exhibit 3D topography and are roughly 10X times smaller than those achieved by typical printing techniques. Optical characterization of the LIS showed that they emit strong broad visible fluorescence emanating from the edges of the features. Crystallographic characterization of LIS (XRD) showed that film undergoes a chemical change during exposure (likely the thermal decomposition of sodium citrate into sodium carbonate). The presence of newly formed microcrystallites visible on either side of the LIS in SEM images suggests that the observed fluorescence may be from the recrystallization of sodium citrate, which was confirmed by finding out sodium citrate having inherent fluorescent nature and found that the presence of water molecules acted as fluorescence quenchers. The diffraction pattern of beam provided just enough heat to drive the water molecule away at the edges of LIS, making their fluorescent signal go up when compared to other parts of the film, which contains water molecules (acting as fluorescence quencher). At the center of LIS, where the beam intensity is very high, leading to decomposition of sodium citrate to sodium crbonate, which does not happen away from the center of the beam (just enough to drive away the water but not decompose the citrate). The LIS formation was possible only if the Ag particles were surrounded by low decomposing material, such as PVOH or sodium citrate at low laser power ($\approx 20mW$).

7.2 Future Work

The future work will be focused on to find the source and mechanism of fluorescence in sodium citrate and factors effecting the fluorescence so that the fluorescent active LIS can be used for sensor applications, where the surroundings of LIS can be probed based on its fluorescence. To measure the important physical parameter during LIS formation i.e. temperature raise during laser-nanoparticle film interaction and to develop a model which can predict the temperature raise. To understand the effect of important experimental and instrumental parameters on LIS, such as different shape and size of particles, type (pulsed/continuous) of laser, shapes of laser beam (such as square, spherical), wave length of laser and different NA objective lens. The other challenges to overcome are coffee ring effect during drying process of the coating and finding ways to increase the shelf life of the coat.

REFERENCES

Akiyama, Morito, Xu, Chao-Nan, Liu, Yun, Nonaka, Kazuhiro, & Watanabe, Tadahiko. 2002. **97**.

Aminuzzaman, Mohammod, Watanabe, Akira, & Miyashita, Tokuji. 2010. Direct writing of conductive silver micropatterns on flexible polyimide film by laser-induced pyrolysis of silver nanoparticle-dispersed film. *Journal of Nanoparticle Research*, **12**(3), 931–938.

Arcidiacono, S., Bieri, N. R., Poulikakos, D., & Grigoropoulos, C. P. 2004. On the Coalescence of gold nanoparticles. *Int. J. Multiphase Flow*, **30**, 979.

Aruna, Singanahally T., & Mukasyan, Alexander S. 2008. Combustion synthesis and nanomaterials. *Current Opinion in Solid State and Materials Science*, **12**(3-4), 44–50.

B. D. Gates, Q. Xu, M. Stewart D. Ryan C. G. Willson, & Whitesides, G. M. 2005. New approaches to nanofabrication: Molding, printing, and other techniques. *Chem. Rev.*, **105**, 1171–96.

Barbooti, Mahmood M., & Al-Sammerrai, Dhoaib a. 1986. Thermal decomposition of citric acid. *Thermochimica Acta*, **98**, 119–126.

Bielawski, M, & Baranowska, A. 1985. Thermoanalytical investigation of citric acid and complexe salds of the transition metals with citric acid. *Thermochimica Acta*, **92**, 235–239.

Bohren, C. F., & Huffman, D. R. 1983. *Absorption and Scattering of Light by Small Particles*. John Wiley & Sons, Inc., New York.

Born, M., & Wolf, E. 1999. *Principles of Optics*. 7 edn. Cambridge University Press, Cambridge, U.K.

Buffat, Ph, & Borel, J-P. 1976. Size effect on the melting temperature of gold particles. *Physical Review A*, **13**(6), 2287–2298.

Buscall, R., Ottewill, R.H., Corner T, & Stageman, J.F., Eds. 1985. *Stability of Polymer Latices in Polymer Colloids*. Academic Press.

C. Schizas, V. Melissinaki, A. Gaidukeviciute C. Reinhardt C. Ohrt V. Dedoussis B. Chichkov C. Fotakis M. Farsari D. Karalekas. 2010. On the design and fabrication by two-photon polymerization of a readily assembled micro-valve. *Int. J. Adv. Manuf. Technol*, **48**, 435–441.

Chander, Harish, Haranath, D., Shanker, Virendra, & Sharma, Pooja. 2004. Synthesis of nanocrystals of long persisting phosphor by modified combustion technique. *Journal of Crystal Growth*, **271**, 307–312.

Chris D. Geddes, I.G., Joanna Malicka Zygmunt Gryczynski Joseph R. Lakowicz. 2003. Metal-Enhanced Fluorescence: Potential Applications in HTS. *Combinatorial Chemistry & High Throughput Screening*, **6**, 109–117.

Deegan, Robert D, Bakajin, Olgica, & Dupont, Todd F. 1997. Capillary flow as the cause of ring stains from dried liquid drops. **389**, 827–829.

Ding, L., Davidchack, R. L., & Pan, J. 2009. A molecular dynamics study of sintering between nanoparticles. *Computational Materials Science*, **45**, 247.

E. Stankevicius, T. Gertus, M. Rutkauskas M. Gedvilas G. Raciukaitis R. Gadonas V. Smilgevicius M. Malinauskas. 2012. Fabrication of microtube arrays in photopolymer sz2080 by using three different methods of direct laser polymerization technique. *J. Micromech. Microeng*, **22**, 065022.

Elliott, D. J. 1989. *Integrated circuit fabrication technology*. 2nd ed. McGraw-Hill Book.

Evanoff, David D, & Chumanov, George. 2005. Synthesis and optical properties of silver nanoparticles and arrays. *Chemphyschem : a European journal of chemical physics and physical chemistry*, **6**(7), 1221–31.

Everett, D.H. 1988. *Basic Principles of Colloid Science*. Royal Society of Chemistry,Cambridge.

Ganesh, RK, & Faghri, A. 1997. A generalized thermal modeling for laser drilling process- I . Mathematical modeling and numerical methodology. *International journal of heat and mass*, **40**(14), 3351–3360.

Garcia-Guinea, J., Correcher, V., Lozano-Diz, E., Baares, M.A., Lopez-Arce, P., Garca, A.M., & Moreno, D.A. 2011. Effect of thermal annealing on synthetic sodium oxalate crystals. *Journal of Analytical and Applied Pyrolysis*, **91**(2), 332–337.

Gibson, F.W. 1998. *Stabilization of Submicron Metal Oxide Particles in Aqueous Media*. Thesis, Virginia Polytechnic Institute and State University, Blacksburg, Virginia.

Gouadec, Gwenael, & Colomban, Philippe. 2007. Raman Spectroscopy of nanomaterials: How spectra relate to disorder, particle size and mechanical properties. *Progress in Crystal Growth and Characterization of Materials*, **53**(1), 1–56.

Govorov, Alexander O, & Richardson, Hugh H. 2007. Generating heat with metal nanoparticles. *Nano Today*, **2**(1), 30–38.

Guarini, Giulio G T, & Dei, Luigi. 1995. Thermal investigation of the role of outer surfaces in the decomposition of crystalline solids. *Thermochimica Acta*, **270**, 79–88.

Hamaker, H.C. 1937. The London-van der Waals attraction between spherical particles. *Physica*, **4**(10), 1058 – 1072.

Hartland, Gregory V., Hu, Min, & Sader, John E. 2003. Softening of the Symmetric Breathing Mode in Gold Particles by Laser-Induced HeatingâĂă. *The Journal of Physical Chemistry B*, **107**(30), 7472–7478.

Hawa, T., & Zachariah, M. R. 2004. A Molecular Dynamics Study of particle-particle collisions between Hydrogen surface passivated silicon nanoparticles. *Phys. Rev. B*, **69**, 035417.

Hawa, T., & Zachariah, M. R. 2006. Coalescence Kinetics of unequal sized nanoparticles. *Aerosol Sci*, **37**, 1.

Hecht, E. 2002. *Optics*. 4 edn. Addison Wesley, New York.

Hendy, S., Brown, S. A., & Hyslop, M. 2003. Coalescence of nanoscale metal clusters: Molecular-dynamics study. *Phys. Rev. B*, **68**, 241403.

Hodak, Jose, Martini, Ignacio, & Hartland, Gregory V. 1998. Ultrafast study of electron-phonon coupling in colloidal gold particles. *Chemical Physics Letters*, **284**, 135–141.

Hu, H., & Larson, R. G. 2002. Evaporation of a sessile droplet on a substrate. *J. Phys.Chem. B*, **106**, 1334–1344.

Huang, Li-Ming, Chen, Cheng-Hou, & Wen, Ten-Chin. 2006. Development and characterization of flexible electrochromic devices based on polyaniline and poly(3,4-ethylenedioxythiophene)-poly(styrene sulfonic acid). *Electrochimica Acta*, **51**(26), 5858 – 5863.

Hulst, H. C. v. d. 1981. *Light Scattering by Small Particles in Water*. Academic Press, London.

Huynh, Khanh An, & Chen, Kai Loon. 2011. Aggregation kinetics of citrate and polyvinylpyrrolidone coated silver nanoparticles in monovalent and divalent electrolyte solutions. *Environmental science & technology*, **45**(13), 5564–71.

Israelachvili, J. 1992. *Intermolecular and Surface Forces, Second Edition*. Academic Press,San Diego.

J. Serbin, A. Ovsianikov, B. Chichkov. 2004. Fabrication of woodpile structures by two-photon polymerization and investigation of their optical properties. *Opt. Express*, **12**, 5221–5228.

J. Trull, L. Maigyte, V. Mizeikis M. Malinauskas S. Juodkazis C. Cojocaru M. Rutkauskas M. Peckus V. Sirutkaitis K. Staliunas. 2011. Formation of collimated beams behind the woodpile photonic crystal. *Phys. Rev.A*, **84**(3), 033812.

Johnson, P. B., & Christy, R. W. 1972. Optical Constants of the Noble Metals. *Phys. Rev. B*, **6**, 4370–4379.

Kandpal, Sanjeev Kumar, Goundie, Ben, Wright, Joshua, Pollock, Rachel a, Mason, Michael D, & Meulenberg, Robert W. 2011. Investigation of the emission mechanism in milled SrAl2O3:Eu, Dy using optical and synchrotron X-ray spectroscopy. *ACS applied materials and interfaces*, **3**(9), 3 2–6.

Karthikeyani, A, & Jagannathan, R. 2000. Eu^{2+} luminescence in stillwellite-type SrBPO5-a new potential X-ray storage phosphor. *Journal of Luminescence*, **86**, 79–85.

Khlebtsov, N. G., & Dykman, L. A. 2010. Optical properties and biomedical applications of plasmonic nanoparticles. *J Quant Spectrosc Radiat Transfer*, **111**, 1–35.

Kim, Dongjo, Jeong, Sunho, Moon, Jooho, & Kang, Kyungtae. 2006. Ink-Jet Printing of Silver Conductive Tracks on Flexible Substrates. *Molecular Crystals and Liquid Crystals*, **459**(1), 45/[325]–55/[335].

Koparde, V., & Cummings, P. 2005. Molecular Dynamics Simulation of Titanium Dioxide Nanoparticle Sintering. *J Phys Chem B*, **109**, 24280.

Koparde, V., & Cummings, P. 2008. Sintering of Titanium dioxide nanoparticles: A Comparison between molecular dynamics and phenomenological modeling. *J. Nanopart. Res*, **10**, 1169.

Kreibig, U., & Vollmer., M. 1995. *Optical Properties of Metal Clusters*. Vol. 25. Springer-Verlag, Berlin, Germany.

Kurita, Hideaki, Takami, Akinori, & Koda, Seiichiro. 1998. Size reduction of gold particles in aqueous solution by pulsed laser irradiation. *Applied Physics Letters*, **72**(7), 789–791.

la Fuente Vornbrock, Alejandro De. 2009 (December). *Roll Printed Electronics: Development and Scaling of Gravure Printing Techniques*. PhdThesis, University of California at Berkeley, Berkeley, USA.

Laven, Philip. 2013. *Mie plot*.

M. Malinauskas, A. Zukauskas, V. Purlys K. Belazaras A. Momot D. Paipulas R. Gadonas A. Piskarskas H. Gilbergs A. Gaidukeviciute I. Sakellari M. Farsari S. Juodkazis. 2010. Femtosecond laser polymerization of hybrid/integrated micro-optical elements and their characterization. *J. Opt. 12*, **12**, 321–325.

Madou, M. J. 2002. *Fundamentals of Microfabrication: The Science of Miniaturization*. 2nd ed. New York: CRC.

Maekawa, Katsuhiro, Yamasaki, Kazuhiko, Niizeki, Tomotake, Mita, Mamoru, Matsuba, Yorishige, Terada, Nobuto, & Saito, Hiroshi. 2009. Direct writing of conductive silver micropatterns on flexible polyimide film by laser-induced pyrolysis of silver nanoparticle-dispersed film. *59th Electronic Components and Technology Conference*, 1579–1584.

MafunÃl', Fumitaka, Kohno, Jun-ya, Takeda, Yoshihiro, & Kondow, Tamotsu. 2003. Formation of Gold Nanonetworks and Small Gold Nanoparticles by Irradiation of Intense Pulsed Laser onto Gold Nanoparticles. *The Journal of Physical Chemistry B*, **107**(46), 12589–12596.

Maier, S. A. 2007. *Plasmonics: Fundamentals and Applications*. Springer Science, New York.

Mikami, Y. 1994. A new patterning process concept for large-area transistor circuit fabrication without using an optical mask aligner . *IEEE Trans. Elec. Dev.*, **41**(3), 306–314.

Mishra, S. B.; Mishra, A. K.; Luyt A. S.; Revaprasadu N.; Hillie K. T.; Steyn W. J. V.; Coetsee E.; Swart H. C. 2010. Strontium aluminate / polymer composites: Morphology, Luminescent properties and Durability. *J. App. Polymer Sci*, **115**, 579–587.

Mizuno, Katsuhiko, & Okazaki, Satoshi. 1991. Printing Color Filter for Active Matrix Liquid-Crystal Display Color Filter. *JJAP*, **30**(11B), 3313–3317.

Mochida, S., Kubo, H., Usui, Y., Aizawa, H., Katsumata, T., Komuro, S., & Morikawa, T. 2004. Fluorescence thermometer using long afterglow phosphors based on phase angle measurement. *Pages 2498–2501 of: SICE 2004 Annual Conference*, vol. 3.

Moreau, W. M. 1988. *Semiconductor lithography: Principles, Practices and Materials*. Plenum Publishing.

N. D. Denkov, O. D. Velev, P. A. Kralchevsky I. B. Ivanov H. Yoshimura, & Nagayama, K. 1993. Two-dimensional crystallization. *Nature*, **361**(6407), 26.

Nanda, K. K., Kruis, F. E., & Fissan, H. 2002. Evaporation of free PbS nanoparticles: Evidence of Kelvin effect. *Phys. Rev. Lett*, **89**, 256103.

Neuman, Keir C, & Block, Steven M. 2004. Optical trapping. *Review of Scientific Instruments*, **75**(9), 2787–2809.

Nguyen, Bao Toan, Gautrot, Julien E, Nguyen, My T, & Zhu, X X. 2007. Nitrocellulose-stabilized silver nanoparticles as low conversion temperature precursors useful for inkjet printed electronics. *Journal of Materials Chemistry*, **17**(17), 1725.

Panigrahi, B. B. 2007. Sintering and Grain growth Kinetics of ball milled nanocrystalline nickel powder. *Mater. Sci. Eng.*, **A460**, 7.

Pawluk, T., & Wang, L. 2007. Molecular Dynamics Simulation of the coalescence of Iridium clusters. *J. Phys. Chem. C*, **111**, 6713.

Pillai, ZS. 2004. What factors control the size and shape of silver nanoparticles in the citrate ion reduction method. *The Journal of Physical Chemistry B*, **3**(10), 945–951.

Pinchuk, Anatoliy O. 2012. Size-Dependent Hamaker Constant for Silver Nanoparticles. *The Journal of Physical Chemistry C*, **116**(37), 20099–20102.

Pustovalov, V.K., & Bobuchenko, D.S. 1989. Heating, evaporation and combustion of a solid aerosol particle in a gas exposed to optical radiation. *International Journal of Heat and Mass Transfer*, **32**(1), 3–17.

P.Zeng, S.Zajac, P.Clapp, & Rifkin, J. A. 1998. Nanoparticle sintering simulations. *Mater Sci Eng*, **252**(2), 301–306.

R. Guo, S. Xiao, X. Zhai J. Li A. Xia W. Huang. 2006. Micro lens fabrication by means of femtosecond two photon photopolymerization. *Opt. Express*, **14**, 810–816.

Raut, J. S., Bhagat, R. B., & Fichthorn, K. A. 1998. Sintering of Aluminium nanoparticles: a molecular dynamics study. *Nanostruct. Mater*, **10**, 837.

Rekstyte, Sima, Zukauskas, Albertas, Purlys, Vytautas, Gordienko, Yuri, & Malinauskas, Mangirdas. 2013. Direct laser writing of 3D polymer micro/nanostructures on metallic surfaces. *Applied Surface Science*, **270**(0), 382 – 387.

Rivas, L, Sanchez-Cortes, S, & Garcia-Ramos, JV. 2001. Growth of silver colloidal particles obtained by citrate reduction to increase the Raman enhancement factor. *Langmuir*, **17**(3), 574–577.

Ronda, C R, Jüstel, T, & Nikol, H. 1998. Rare earth phosphors: fundamentals and applications. *Journal of Alloys and Compounds*, **275-277**(1-2), 669–676.

S. Jariwala, K. Venkatakrishnan, B. Tan. 2010. Single step self-enclosed fluidic channels via two photon absorption (TPA) polymerization. *Opt. Express*, **18**, 1630–1636.

Shaw, D.J. 1992. *Introduction to Colloid and Surface Chemistry, Fourth Edition*. Butterworth-Heinemann Ltd., Oxford.

Sirringhaus, H. 2000. High-Resolution Inkjet Printing of All-Polymer Transistor Circuits. *Science*, **290**(5499), 2123–2126.

Solomon, Sally D, Bahadory, Mozghan, Jeyarajasingam, Aravindan V, Rutkowsky, Susan A, & Boritz, Charles. 2007. Synthesis and Study of Silver Nanoparticles. **84**(2), 322–325.

Son, Nguyen Manh, Vien, Le Thi Thao, Bao, Le Van Khoa, & Trac, Nguyen Ngoc. 2009. Synthesis of $SrAl_2O_4$:Eu^{2+},Dy^{3+} phosphorescence nanosized powder by combustion method and its optical properties. *Journal of Physics: Conference Series*, **187**(Sept.), 012017.

Song, Pengxiang, & Wen, Dongsheng. 2010. Surface Melting and Sintering of metallic nanoparticles. *J. Nanoscience and Nanotechnology*, **10**, 8010.

Strawhecker, K E, & Manias, E. 2000. Structure and Properties of Poly (vinyl alcohol)/ Na^+ Montmorillonite Nanocomposites. 2943–2949.

Tadros, Th.F. 1987. *Solid-Liquid Dispersions*. Academic Press.

Tekin, Emine, Smith, Patrick J, & Schubert, Ulrich S. 2008. Inkjet printing as a deposition and patterning tool for polymers and inorganic particles. *Soft Matter*, **4**(4), 703.

The Gale Group, Inc. 1970-1979. *Laser Radiation, Effects of*.

Turkevich, J., Stevenson P.C., & Hillier, J. 1951. A study Of the nucleation and growth processes in the synthesis of colloidal gold. *Discussions of the Faraday Society*, **11**, 55–75.

Van den Eeckhout, Koen, Smet, Philippe F., & Poelman, Dirk. 2010. Persistent Luminescence in Eu2+-Doped Compounds: A Review. *Materials*, **3**(4), 2536–2566.

Vargaftik, N.B. 1972. *Handbook on Thermophysical Properties of Gases and Liquids. 2nd ed.* Nauka, Moscow, USSR.

Šileikaite, Asta, Prosyčevas, Igoris, Puišo, Judita, Juraitis, Algimantas, & Guobiene, Asta. 2006. Analysis of Silver Nanoparticles Produced by Chemical Reduction of Silver Salt Solution. **12**(4).

Wakai, F. 2006. Modeling and Simulation of Elementary Processes in ideal sintering. *J. Am. Cerm. Soc.*, **89**, 1471.

Wang, Jianting, Moore, Joseph, Laulhe, Sebastien, Nantz, Michael, Achilefu, Samuel, & Kang, Kyung a. 2012. Fluorophore-gold nanoparticle complex for sensitive optical biosensing and imaging. *Nanotechnology*, **23**(9), 095501.

Watanabe, Kazuo, & Kisaka, Ryuichi. 1993. Recent development on thermal papers. *Proceedings of SPIE-The International Society for Optical Engineering*, **1912**, 76–82.

Willson, C. Grant, & Roman, Bernard J. 2008. The Future of Lithography: SEMATECH Litho Forum 2008. *ACS Nano*, **2**(7), 1323–1328.

Wu, D.T., Yokoyama A., & Setterquist, R.L. 1991. An experimental study on the effect of adsorbing and non-adsorbing block sizes on divlock copolymer adsorption. *Polymer journal*, **23**(5), 709–714.

Yunker, Peter J, Still, Tim, Lohr, Matthew a, & Yodh, a G. 2011. Suppression of the coffee-ring effect by shape-dependent capillary interactions. *Nature*, **476**(7360), 308–11.

Zeng, Shuwen, Yong, Ken-Tye, Roy, Indrajit, Dinh, Xuan-Quyen, Yu, Xia, & Luan, Feng. 2011. A Review on Functionalized Gold Nanoparticles for Biosensing Applications. *Plasmonics*, **6**, 491–506.

Zhao, Changliang, Chen, Donghua, Yuan, Yuhong, & Wu, Ming. 2006. Synthesis of $Sr_4Al_{14}O_{25}$:Eu^{2+},Dy^{3+} phosphor nanometer powders by combustion processes and its optical properties. *Materials Science and Engineering: B*, **133**(1-3), 200–204.

Zhu, H. L., & Averback, R. S. 1996a. Sintering of Nano-particle powders: Simulation and Experiments. *Mater. Manuf. Processes*, **11**, 905.

Zhu, H. L., & Averback, R. S. 1996b. Sintering Process of Two nanoparticles: A Study by Molecular Dynamics simulations. *Philos. Mag. Lett*, **73**, 27.

Appendix A

MAKING 15 NANOMETER SILVER PARTICLES

Cleaning

1. Gather a stir bar, a burette, an Erlenmeyer flask, a 1000mL beaker, and a 600mL beaker

2. Mix 200mL of Ethanol, 24mL of deionized water, and 24 grams of potassium hydroxide

3. Use mixture to clean glassware and then rinse thoroughly with deionized water.

Synthesis

1. Measure 0.17g of silver nitrate and put it in the 1000mL beaker. Pour in 1L of deionized water measured using a graduated cylinder

2. Measure 0.0378g of sodium borohydride and put in the 600mL beaker. Pour in 500mL of deionized water measured using a graduated cylinder.

3. Pour 30mL of sodium borohydride solution into Erlenmeyer flask with stir bar and then let this cool in an ice bath for 20 minutes while the stir bar is stirring at the lowest setting.

4. Fill the burette with silver nitrate solution

5. After the sodium borohydride cools for 20 minutes, carefully adjust the burette so silver nitrate solution is added to the sodium borohydride solution at a rate of 1 drop per second

6. Stop stirring immediately after 10mL have been added and remove from the ice bath.

7. Remove the stir bar.

Appendix B

CONCENTRATING AG NANOPARTICLE SOLUTION

Making polymer solution beforehand

1. Add 150mL deionized water and 20g of PVOH 31-50k to a 400mL beaker.

2. Heat solution to 200°C for 1.5 hours while stirring at 600 to 800rpms. Increase the RPM as the polymer dissolves because the viscosity is increasing.

Concentrating the silver

1. Gather two empty 250mL round bottom flasks and a steam bump

2. Fill one round-bottom flask with 4mL of water for comparison to the concentrated sample.

3. Mass the other empty round-bottom flask

4. Measure out the necessary amount of silver that needs to be concentrated with a graduated cylinder.

5. Pour the measured silver into the round-bottom flask and then mass it again.

6. Turn on the power of the rotovap (rotational evaporator), the heating bath, the vacuum, and the connecting sink just enough to let water run through the rotovap

7. Set the Pressure to 60mbar for a starting amount of 120mL.

8. Turn on the vacuum and allow the silver to boil. If the boiling is too violent then increase the pressure setting. As the amount of silver decreases, decrease the pressure.

9. Concentrate until there is about 4mL of silver, if it drops below 4 mL, necessary amount to total to 4 mL is added (deionized water) into the flask and spin to collect the silver from the sides of the flask.

10. Using a syringe, add 1.9mL of the previously made polymer and then mix using a vortex until the concentrated silver becomes entirely viscous.

Appendix C

DYNAMIC LIGHT SCATTERING SIZE MEASUREMENT

1. Turn on the Ocean Optics Zetasizer, model Zen3600.

2. Open the program Zetasizer.

3. Go to File New Measurement File This will cause a new window to pop open to name the file and save it into the desired location. This file will store the data that is taken and will save by itself. The next time that data needs to be taken, go to File> Open> Measurement File and file this same file for the data to be stored in.

4. Check the settings for the program: Make sure the workspace (drop-down menu on the top-left) and the SOP (drop-down menu on the top-right) read Size and Manual Measurement respectively.

5. Click on the green triangle at the top of the window to start the process.

6. In the pop-up window check the settings again: Measurement Type: Size, Sample Name: Batch number and current date, Material: SilverNP, Dispersant: Water, Cell: Disposal sizing cuvette, Data Processing the Analysis model: High resolution. Now hit the OK button.

7. In the new window that follows click on the green triangle then wait for the size measurement to be taken. There will be a beep to signal that the process is finished.

8. Once done close the program and the instrument.

Appendix D

UV-VIS MEASUREMENT

1. Prepare the background for the silver sample: mix 0.25mL of the polymer solution previously made and put into the silver with 10mL of deionized water in another vial.

2. Fill a disposable cuvette with 2mL of the background and another cuvette with 2mL of the silver sample.

3. Open the program SpectraSuite and go to File New Absorbance Measurement.

4. This will open a new window asking for the choice of source. Make sure that USB4C00393 is highlighted and hit the Next button.

5. Turn on the light source (If the switch is centered then the light source is off, if the switch is off to the side then the light is on)

6. Adjust the integration time until the colored number labeled Last Peak Value is slightly higher than the Recommended Peak Value (the integration time will usually be lower than 30 milliseconds) and hit the Next button.

7. Place the cuvette that holds the background in the holder.

8. Make sure that the light source is on and then click on the given button that shows a bright light bulb. Move on to the next step.

9. Turn off the light source then click on the given button showing a dark light bulb and click on the Finish button. Now the setting up of the background is finished

10. Remove the cuvette with the background from the holder and replace it with the cuvette with the sample

11. Once the absorbance measurement is in the appropriate range (i.e less noise or else dilute the sample) hit play icon to take the measurement. Click on the save button and save in the appropriate place as a file type of Tab Delimited, No Header

Appendix E

COATING & CUTTING PROCEDURE

Coating Paper with Ag-PVOH coating formulation

1. Prepare hp Brochure Paper 180g, Glossy to a size of "8.5x5.5".

2. Tape to corners to the Draw-Down Coater.

3. Insert Rod number 3 or 5 or 10 into the holder.

4. Test instrument to adjust the height of the rod, recommended reading of 7 units (about

3.5cm from the surface of the substrated) and a speed of 2.5cm per second.

5. Turn instrument on and spread the silver in front of the rod while it is moving.

6. Set out to air dry.

Cutting coated paper

1. Gather 22mmx22mm coverslip, a blade, blank slides, and double-sided tape.

2. Find area on paper coating that has even coverage and trace outline of coverslip.

3. Use blade to cut out the shape.

4. Mass the cut-out and record it.

5. Use double-sided tape to stick square onto blank slide..

6. Record the slide number with sample description.

Appendix F

TEMPERATURE PROFILE AROUND THE PARTICLE

The theory behind heat absorption by spherical particles is treated in literature review chapter. The list of major equations used in MATHCAD software are listed here along with MATHCAD worksheet.

Distribution of temperature inside the particle given is given by: For $b \neq -1$,

$$T = T_0 \left(1 + \frac{q_0(r_0^2 - r^2)(b+1)T_\infty^b}{6k_{0\infty}T_0^{b+1}} \right)^{1/b+1} \tag{F.1}$$

For $b = -1$,

$$T = T_0 exp \left(\frac{q_0(r_0^2 - r^2)}{6k_{0\infty}T_\infty} \right) \tag{F.2}$$

Distribution around the particle can be given by using the following equations, $a \neq -1$,

$$T(r) = T_\infty \left[1 + \frac{r_0}{r} \left(\left(\frac{T_0}{T_\infty} \right)^{a+1} - 1 \right) \right] \tag{F.3}$$

For $a = -1$,

$$T(r) = T_\infty \left(\frac{T_0}{T_\infty} \right)^{r_0/r} \tag{F.4}$$

To estimate surface temperature. For two different a values the expression reduces to: For a=0,

$$T_0 = T_\infty + \frac{I_0 Q_{abs} r_0}{4k_\infty} [1 - exp(-Bt)] \tag{F.5}$$

For a=1,

$$T_0 = T_\infty A \frac{A + 1 - (A - 1)exp(-ABt)}{A + 1 + (A - 1)exp(-ABt)} \tag{F.6}$$

where $A = \left(\frac{I_0 Q_{abs} r_0}{2k_\infty T_\infty} + 1 \right)^{0.5}$, $B = \frac{3k_\infty}{c_0 \rho_0 r_0^2}$.

Input Laser Power $Power := 20mW$

Numerical aperture $NA := 0.65$

Radius of the particle $r_0 := 50nm$

Wavelength of the laser $\lambda := 532nm$

For Small particles ($2\pi\ r_0$ / $2\pi\ r_0$
Less than 1)
$$\frac{2\pi\ r_0}{\lambda} = 0.591$$

Beam waist $$d := \frac{0.61\lambda}{NA}$$

$$d = 499.262 \cdot nm$$

Intensity of beam $$I_0 := \frac{Power}{\left(\frac{\pi\ d^2}{4}\right)}$$ $$I_0 = 1.022 \times 10^5 \cdot \frac{MW}{m^2}$$

Absorption efficiency table

$T123 :=$

	0	1
0	$1 \cdot 10^{-3}$	$2.145 \cdot 10^{-3}$
1	$1.012 \cdot 10^{-3}$	$2.169 \cdot 10^{-3}$
2	$1.023 \cdot 10^{-3}$	$2.195 \cdot 10^{-3}$
3	$1.035 \cdot 10^{-3}$	$2.22 \cdot 10^{-3}$
4	$1.047 \cdot 10^{-3}$	$2.246 \cdot 10^{-3}$
5	$1.059 \cdot 10^{-3}$	$2.272 \cdot 10^{-3}$
6	$1.072 \cdot 10^{-3}$	$2.298 \cdot 10^{-3}$
7	$1.084 \cdot 10^{-3}$	$2.325 \cdot 10^{-3}$
8	$1.096 \cdot 10^{-3}$	$2.352 \cdot 10^{-3}$
9	$1.109 \cdot 10^{-3}$	$2.379 \cdot 10^{-3}$
10	$1.122 \cdot 10^{-3}$	$2.407 \cdot 10^{-3}$
11	$1.135 \cdot 10^{-3}$	$2.435 \cdot 10^{-3}$
12	$1.148 \cdot 10^{-3}$	$2.463 \cdot 10^{-3}$
13	$1.161 \cdot 10^{-3}$	$2.491 \cdot 10^{-3}$
14	$1.175 \cdot 10^{-3}$	$2.52 \cdot 10^{-3}$
15	$1.189 \cdot 10^{-3}$	...

$i := 0, 1 .. 1000$

These i's values are the set of interesting particle sizes

$$i := \begin{pmatrix} 0 \\ 200 \\ 259 \\ 294 \\ 320 \\ 339 \\ 355 \\ 369 \\ 381 \\ 391 \\ 400 \\ 460 \\ 495 \\ 520 \\ 540 \\ 556 \\ 569 \\ 581 \\ 591 \\ 600 \end{pmatrix}$$

Absorbtion efficiency for 50nm radius particle $effi := T123_{340, 1} = 0.234$

This gives amount of radiation absorbed by particle $\quad I_0 \cdot effi = 2.393 \times 10^4 \cdot \dfrac{MW}{m^2}$

Surface area of the particle $\qquad\qquad\qquad S_0 := 4\pi\, r_0^2$

$S_0 = 3.142 \times 10^{-14}\, m^2$

This gives heat generation per unit volume $\qquad q_0 := \dfrac{\dfrac{I_0 \cdot effi \cdot S_0}{4}}{\dfrac{4}{3}\pi\, r_0^3} = 3.59 \times 10^{14}\, \dfrac{1}{L} \cdot W$

dependence of thermal conductivity of nanoparticle (material) on temperature $\qquad b := 0$

Surrounding temperature $\qquad\qquad T_\alpha := 25\,°C \qquad\qquad T_\alpha = 298.15\,K$

Thermal conductivity of nanoparticle (Ag) $\qquad k_{0\alpha} := 1.72\, \dfrac{W}{cm \cdot \Delta°C} \qquad k_{0\alpha} = 172 \cdot \dfrac{W}{m \cdot K}$

dependence of thermal conductivity of surrounding (material) on temperature $\qquad a := 0$

Integration Problem

$\rho_0 := 10.49\, \dfrac{gm}{cm^3} \qquad\qquad$ Thermal conductivity of PVOH $\qquad k_\alpha := 0.2 \cdot \dfrac{W}{m \cdot K}$

$\qquad\qquad C_0 := 0.24\, \dfrac{J}{gm \cdot \Delta°C} \qquad V_0 := \dfrac{4 \cdot \pi \cdot r_0^3}{3} \qquad V_0 = 0 \cdot m^3$

$fl(t, T) := \dfrac{S_0}{\rho_0 \cdot C_0 \cdot V_0} \cdot \left[\dfrac{I_0 \cdot effi}{4} - \dfrac{k_\alpha \cdot T_\alpha}{(a+1) \cdot r_0} \left[\left(\dfrac{T}{T_\alpha} \right)^{a+1} - 1 \right] \right]$

$\dfrac{d}{dt}T(t) = f(t, T) \qquad T(t0) = T0 \qquad\qquad constant_1 := \dfrac{\dfrac{S_0}{\rho_0 \cdot C_0 \cdot V_0}}{\dfrac{K \cdot s^2}{kg}} = 23.832$

Tried to make things unitless

$$\text{constant}_2 := \frac{\dfrac{I_0 \cdot effi}{4}}{\dfrac{kg}{s^3}} = 5.983 \times 10^9$$

$$\text{constant}_3 := \frac{\dfrac{k_\alpha \cdot T_\alpha}{r_0}}{\dfrac{kg}{s^3}} = 1.193 \times 10^9$$

$$f(t, T) := \text{constant}_1 \cdot \left[\text{constant}_2 - \frac{\text{constant}_3}{(a+1)} \left[\left(\frac{T}{298.15} \right)^{a+1} - 1 \right] \right]$$
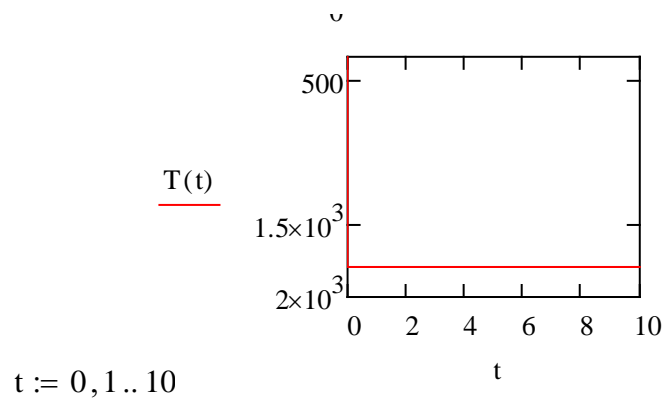
$$T0 := 298.15$$

Enter the desired solution parameters:

$$t1 := 10 \qquad \text{Endpoint of solution interval}$$

$$N := 1 \times 10^5 \qquad \text{Number of solution values on [t0, t1]}$$

Given
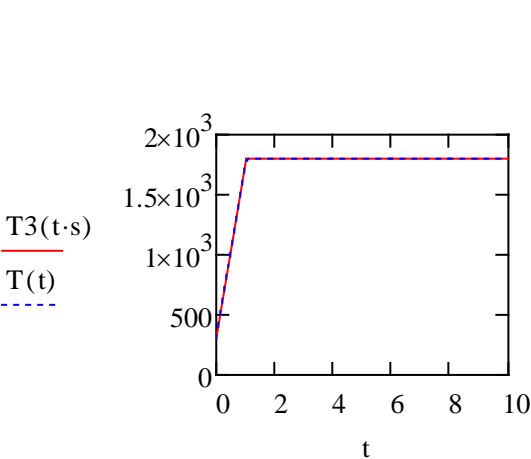
$$T'(t0) = f(t0, T(t))$$

$$T := \text{Odesolve}(t, t1)$$

$$t := 0, 1 .. 10$$

$T(t) =$

298.15
$1.794 \cdot 10^3$
$1.794 \cdot 10^3$
$1.794 \cdot 10^3$
$1.794 \cdot 10^3$
$1.794 \cdot 10^3$
...

This is the analytical expression from paper to cross check the value from integration

$$T3(t) := T_\alpha + \frac{I_0 \cdot \text{effi}}{4} \cdot \frac{r_0}{k_\alpha} \left[1 - e^{\left(-3 \frac{k_\alpha}{\rho_0 \cdot C_0 r_0^2} t \right)} \right]$$

$T3(t \cdot s) =$

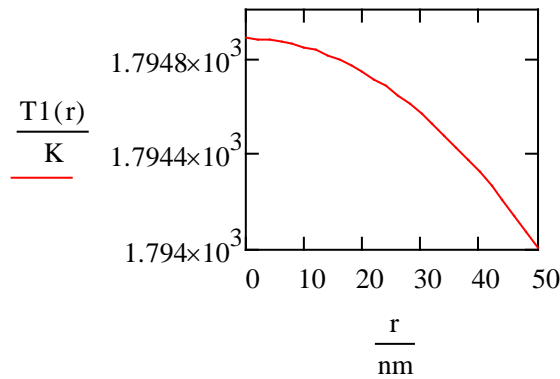|	
298.15	K
$1.794 \cdot 10^3$	
$1.794 \cdot 10^3$	
$1.794 \cdot 10^3$	
$1.794 \cdot 10^3$	
$1.794 \cdot 10^3$	
$1.794 \cdot 10^3$	
$1.794 \cdot 10^3$	
$1.794 \cdot 10^3$	
$1.794 \cdot 10^3$	
$1.794 \cdot 10^3$	
$1.794 \cdot 10^3$	

$T3(t \cdot s)$ ———
$T(t)$ - - - - -

$$T_0 := T3(10.s) = 1.794 \times 10^3 \, K$$

This equation discribes temperature distribution inside the particle (equation T1(r))

$$T1(r) := \left[1 + \frac{q_0 \cdot \left(r_0^2 - r^2 \right)(b+1) T_\alpha^0}{6 k_{0\alpha} T_0^{0+1}} \right]^{\frac{1}{0+1}} \cdot T_0$$

$r := 0nm, 2nm .. 50nm$

Note: We can't club these two equations (T1(r) & T2(r)) because the thermal conductivity of both materials are very different and vary differently with the temperature. So you can't use one equation to predict temperature distribution in and around the particles.

This equation discribes temperature distribution around the particle (equation T2(r))

$$T2(r, a) := \left[1 + \frac{r_0}{r} \left[\left(\frac{T_0}{T_\alpha} \right)^{a+1} - 1 \right] \right]^{\frac{1}{a+1}} \cdot T_\alpha$$

$r := 1nm, 2nm .. 1000nm$

129
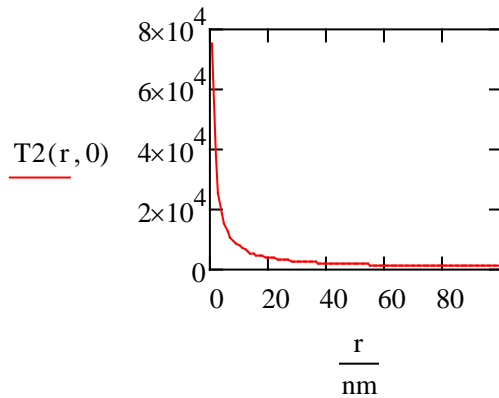
Appendix G

DLVO MODELING RESULTS

DLVO theory is described in detail in the literature review chapter. The list of major equations used in MATHCAD software to predict attractive force (V_{vdW}), repulsive force (V_{R0}), and the total potential energy (V_{tot}) are listed here along with MATHCAD worksheet.

$$V_{R0} = 2\pi\varepsilon r_{NP}\xi^2 exp(-\kappa H1) \tag{G.1}$$

where

$$\kappa^{-1} = \left[\frac{\varepsilon KT}{e1^2 \sum_I 2_i z_i^2}\right] \tag{G.2}$$

$$V_{vdW} = \frac{-A}{12\pi H1^2} \tag{G.3}$$

$V_{tot} = V_{R0} + V_{vdW}$, where A is the Hamaker constant and H1 is the particle separation, r_{NP} is the particle radius, κ is a function of the ionic composition and ξ is the zeta potential, I2 is concentration of free ions (in this cas Na and citrate ions), z_i is valency of ions (for Na it is 1 and for citrate it is 3) .

Part-1

Electronic charge $\quad\quad\quad e1 := 1.6902 \cdot 10^{-19} \cdot C$

Boltzman constant $\quad\quad\quad k := 1.38065 \cdot 10^{-23} \dfrac{J}{K}$ $\quad\quad\quad r_{NP} := 5nm$

$T := 298K$

Dielectric constant of Ag, assumed $\quad \varepsilon_{NP} := 35$ $\quad\quad\quad \varepsilon_0 := 8.854 \cdot 10^{-12} \dfrac{F}{m}$

Dielectric constant of water $\quad\quad \varepsilon_{H2O} := 78$

$N_A := 6.023 \cdot 10^{23} \cdot \dfrac{1}{mol}$

$I2 :=$

	0	1
0	$9.806 \cdot 10^{-3}$	3
1	0.048	1

Concentration (molarity) of excess citrate (0) and sodium (1) for freshly made Ag solution

Measured zeta-potentisl of freshly made Ag $\quad\quad\quad \zeta := -59.4mV$

Debye length $\quad\quad\quad \kappa := \left[1000 \cdot N_A \left(\dfrac{e1^2}{\varepsilon_0 \cdot \varepsilon_{H2O}} \cdot \dfrac{1}{k \cdot T} \right) \cdot \dfrac{mol}{L} \cdot \left(I2_{0,0} \cdot 3^2 + I2_{1,0} \cdot 1^2 \right) \right]^{0.5}$

$H1 =$

$1 \cdot 10^{-12}$	m
$1 \cdot 10^{-11}$	
$1.9 \cdot 10^{-11}$	
$2.8 \cdot 10^{-11}$	
$3.7 \cdot 10^{-11}$	
$4.6 \cdot 10^{-11}$	
$5.5 \cdot 10^{-11}$	
$6.4 \cdot 10^{-11}$	
$7.3 \cdot 10^{-11}$	
$8.2 \cdot 10^{-11}$	
$9.1 \cdot 10^{-11}$	
$1 \cdot 10^{-10}$	
$1.09 \cdot 10^{-10}$	
$1.18 \cdot 10^{-10}$	
$1.27 \cdot 10^{-10}$	
...	

$\kappa = 28.706 \cdot \dfrac{1}{nm}$ $\quad\quad\quad \dfrac{1}{\kappa} = 0.035 \cdot nm$
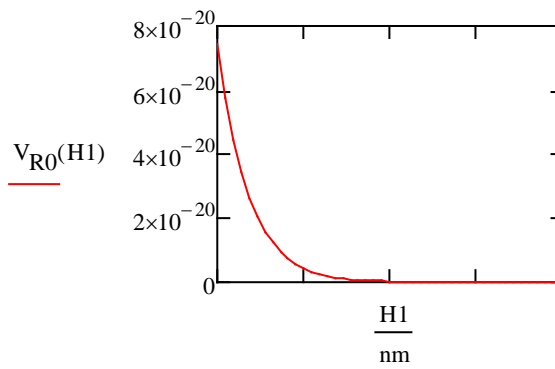
Repulsive energy $\quad\quad V_{R0}(H1) := 2\pi \, r_{NP} \cdot \varepsilon_{H2O} \cdot \varepsilon_0 \cdot \zeta^2 \cdot e^{-\kappa \cdot H1}$

$V_{R0}(1nm) = 2.6126886188 \times 10^{-32} J$

Distance between the particles $\quad\quad H1 := 0.001nm, 0.01nm .. 3nm$

$$V_{R0}(H1)$$ ———

$$\dfrac{H1}{nm}$$

$V_{R0}(H1) =$

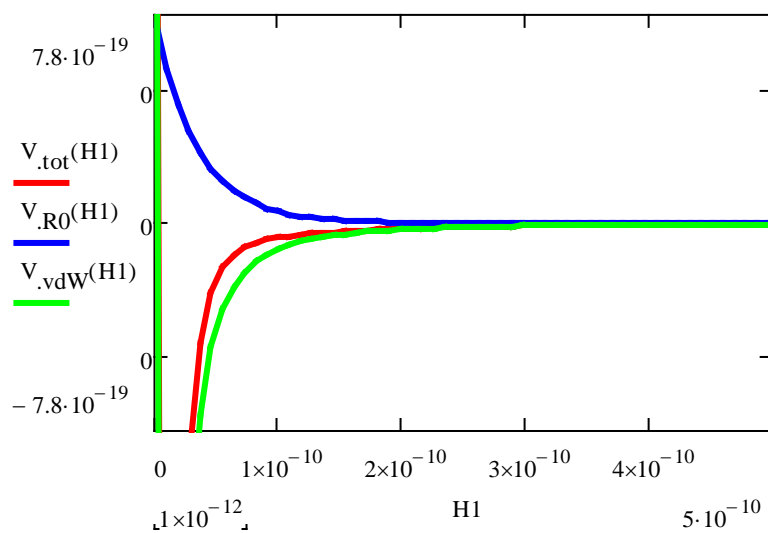|	
$7.439 \cdot 10^{-20}$	$\cdot J$
$5.745 \cdot 10^{-20}$	
$4.437 \cdot 10^{-20}$	
$3.427 \cdot 10^{-20}$	
$2.647 \cdot 10^{-20}$	
$2.044 \cdot 10^{-20}$	
$1.579 \cdot 10^{-20}$	
$1.219 \cdot 10^{-20}$	
$9.416 \cdot 10^{-21}$	
$7.272 \cdot 10^{-21}$	
$5.617 \cdot 10^{-21}$	
$4.338 \cdot 10^{-21}$	
$3.35 \cdot 10^{-21}$	
$2.587 \cdot 10^{-21}$	
$1.998 \cdot 10^{-21}$	
$\dots$	

Hamaker constant $\qquad A := 10^{-21} J$

van der Waals force of attraction between the particles $\qquad V_{vdW}(H1) := \dfrac{-A}{\dfrac{12\pi}{nm^2} H1^2}$

132

$$V_{tot}(H1) := V_{vdW}(H1) + V_{R0}(H1)$$
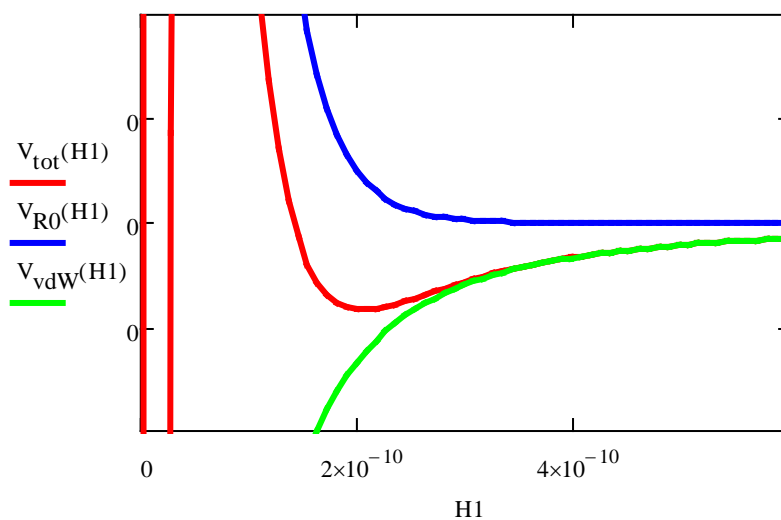
Part-2
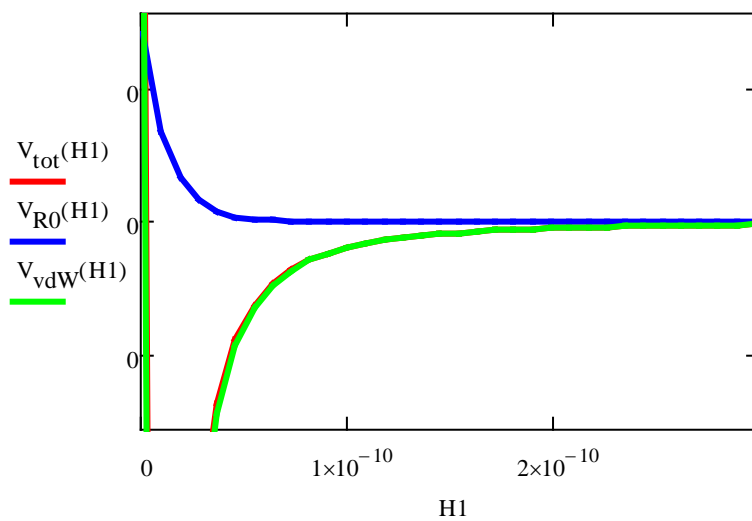
A=3.7*10^-20J

Part-3

After concentrating 200ml Ag batch to 25ml

133

A=10^-21J
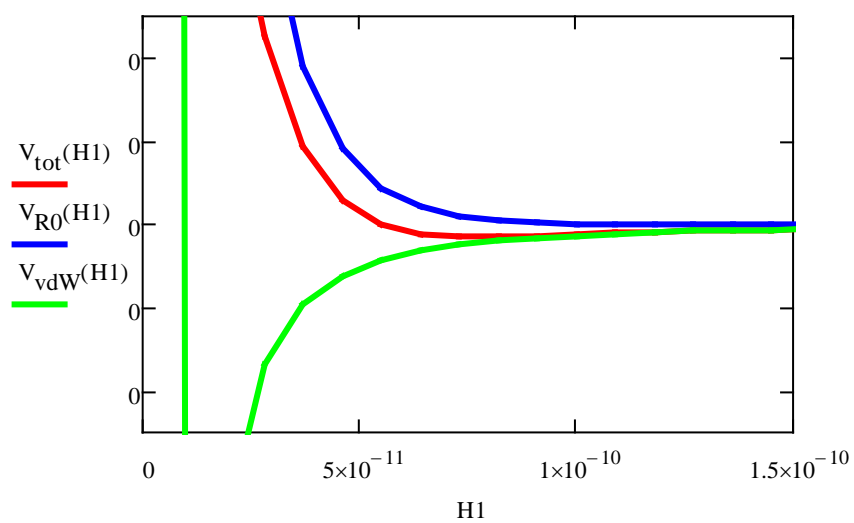
Part-3

After concentrating 200ml Ag batch to 25ml

A=3.7*10^-20J

BIOGRAPHY OF THE AUTHOR

Sanjeev Kumar Kandpal ██████████████████████████ ██ ████ He was raised in Hyderabad, India and graduated from Atomic Energy Central School-III (10th grade) in 2002 and 12th grade from Narayana Junior College in 2004. He attended the Jawaharlal Nehru Technological University and graduated in 2008 with a Bachelor of Technology degree in Chemical Engineering. He entered the Chemical Engineering graduate program at the University of Maine in the fall of 2008. He is a member of the American Institute of Chemical Engineers, American Chemical Society, and The Honor Society of ϕκϕ.

Sanjeev Kumar Kandpal is a candidate for the Doctor of Philosophy degree in Chemical Engineering from The University of Maine in August 2013.